Dynamic Response of a Submerged Floating Tunnel Subject to Hydraulic Loading
Numerical Modelling for Engineering Design

Zou, P.

DOI
10.4233/uuid:59439cc6-8edb-450c-9d03-4f9bd4bbce48

Publication date
2022

Document Version
Final published version

Citation (APA)
Zou, P. (2022). *Dynamic Response of a Submerged Floating Tunnel Subject to Hydraulic Loading: Numerical Modelling for Engineering Design*. [Dissertation (TU Delft), Delft University of Technology]. https://doi.org/10.4233/uuid:59439cc6-8edb-450c-9d03-4f9bd4bbce48

DYNAMIC RESPONSE OF A SUBMERGED FLOATING TUNNEL SUBJECT TO HYDRAULIC LOADING

NUMERICAL MODELLING FOR ENGINEERING DESIGN

DYNAMIC RESPONSE OF A SUBMERGED FLOATING TUNNEL SUBJECT TO HYDRAULIC LOADING

NUMERICAL MODELLING FOR ENGINEERING DESIGN

Proefschrift

ter verkrijging van de graad van doctor
aan de Technische Universiteit Delft,
op gezag van de Rector Magnificus Prof.dr.ir. T.H.J.J. van der Hagen,
voorzitter van het College voor Promoties,
in het openbaar te verdedigen op woensdag 2 maart 2022 om 10.00 uur

door

Pengxu ZOU

Waterbouwkunde Ingenieur, Universiteit Tianjin, China
geboren te Shenyang, China.

Dit proefschrift is goedgekeurd door de

promotor: Prof.dr.ir. W.S.J. Uijttewaal
copromotor: Dr.ir. J.D. Bricker

Samenstelling promotiecommissie bestaat uit:

Rector Magnificus,	voorzitter
Prof.dr.ir. W.S.J. Uijttewaal,	Technische Universiteit Delft, promotor
Dr.ir. J.D. Bricker,	Technische Universiteit Delft, copromotor
Onafhankelijke leden:	
Prof.dr.ir. S.N. Jonkman,	Technische Universiteit Delft
Prof.dr.ir. A. Metrikine,	Technische Universiteit Delft
Prof.dr. P.Z. Lin,	Universiteit Sichuan
Dr.ir. B. Faggiano,	Naples Federico II Universiteit
Prof.dr.ir. J. Westerweel,	Technische Universiteit Delft, reserve member
Overige leden:	
Prof.dr.ir. C.S. Ferreira,	Technische Universiteit Delft

Keywords: Submerged floating tunnel; Cross-section optimization; Internal waves; Extreme hydraulic events; Dynamic response; Flow-induced vibration

Printed by: www.proefschriftmaken.nl

Cover by: P. X. Zou

ISBN 978-94-6366-513-1

CONTENTS

SUMMARY

The submerged floating tunnel (SFT), also called an Archimedes Bridge, is a new type of infrastructure for wide and deep sea-crossings, regarded as one of the alternatives to bored and immersed tunnels and bridges. It is afloat in water employing its buoyancy and a support system to balance its self-weight. However, no prototype SFT has yet been built anywhere due to the immaturity of scientific research and engineering technology. The dynamic response of the SFT subject to operating and extreme environmental conditions, which determines structural safety and reliability, is a crucial issue that needs to be better understood. In order to better comprehend the response of the SFT to hydrodynamic forces, key points including hydrodynamic loads acting on the SFT and the structural dynamic response for various structural configurations, as well as the relations and interactions among these factors must be quantified.

In this study, hydrodynamic loads on various SFT cross-sectional geometries were computed. The parametric cross-section shape described by a Bezier-PARSEC curve was optimized using a hybrid Artificial Neural Network (ANN) and Genetic Algorithm (GA). The practical range of aspect ratios of the SFT cross-section was determined by conducting a sensitivity analysis under tidal current conditions. It was found that an SFT cross-section with an aspect ratio of 0.47 using a leading-edge BP curve under the given clearance is optimal for a balanced consideration of hydrodynamic performance and construction cost. Furthermore, the machine learning method used is shown to be a reliable and effective tool for the SFT cross section optimization design.

The hydrodynamic loads acting on the optimal cross-section shape were compared with simpler shapes under various environmental conditions of currents and waves, including the extreme environmental conditions of internal waves, tsunamis, and super typhoons. An internal solitary wave (ISW), described by the modified Korteweg de Vries (mKdV) theory, was adopted for the hydrodynamic loading analysis of the SFT based on field observations and high-resolution satellite images. It was found that the ISW can remarkably alter the buoyancy - weight ratio (BWR) of the SFT and hence, cause a large vertical hydrodynamic load on the SFT, threatening the safety and reliability of the SFT system. A worst-case tsunami and a hindcast typhoon in the Qiongzhou Strait were selected for extreme event hydrodynamic forcing analysis. It was found that extreme event hazards in the Qiongzhou Strait are rare due to the sheltering effect of Hainan Island. In terms of hydrodynamic forcing, the selected typhoon scenario is more devastating than the tsunami case for an SFT. The proposed parametric cross-sectional shape for the SFT shows better hydrodynamic performance than simpler shapes under all applied environmental conditions and is therefore recommended for the engineering design.

After investigating different types of hydrodynamic loads acting on the SFT, the global dynamic response (including vibration) of the SFT was assessed. A numerical model of a prototype super-long coupled tube-mooring-joint SFT system based on Finite Element Method (FEM) was developed to better predict flow-induced vibration (FIV) and structural dynamic response. A pragmatic approach for structural dynamic response computation under realistic oceanic conditions was developed considering the spatial randomness of hydrodynamic loads. Multi-scale hydrodynamic models including a large-scale oceanographic model and a small-scale CFD model were developed for determination of hydrodynamic loads. It was found that the SFT tube is unlikely to experience severe resonance under steady current conditions, but the vibration of the SFT tube is dominated by wave conditions, where a single dominant mode excitation of the tube with a large wave height and period cause large amplitude motion. In order to give insight into structural dynamic response under extreme environmental conditions, internal forcing on the SFT and structural response of the SFT were computed subject to the ISW and super typhoon loads. This showed that the displacement and acceleration of the SFT under the ISW are far smaller than the structural serviceability requirements, and resonance of the tunnel tube becomes unlikely under the ISW condition due to its rather low intrinsic frequency. The dynamic response of the SFT subject to the typhoon scenario is much more severe than that of the ISW case, and the horizontal stiffness of the moored tube greatly affects its dynamic response. The maximum bending moment and torque on the SFT occur at its shore connections, where failure risk due to structural fatigue or buckling are substantial.

The final aspect of this thesis aims to optimize the SFT structural configuration for minimization of hydraulic resonant loading. The core concept is to investigate the sensitivity of structural response to the structural fundamental frequencies outside the hydrodynamic frequency. It was found that natural frequencies of the SFT system are mainly affected by BWR, tunnel tube length, mooring configuration and stiffness, and joint and shore connection properties. A dynamic process for the SFT configuration optimization subject to different hydrodynamic loads can be established by smartly tuning the fundamental frequencies to mitigate structural dynamic response.

1

INTRODUCTION

The submerged floating tunnel (SFT) is a new type of sea-crossing infrastructure holding promise to facilitate efficient and capable deep-sea transportation. However, behavior of an SFT is complicated due to various types of hydrodynamic loads that the structure is exposed to and the complex dynamic response of coupled components including tunnel tube, mooring lines, and tunnel joints. No prototype SFT has yet been built due to the immaturity of scientific research into this technology. The main theme of this thesis is to investigate hydrodynamic loads acting on the SFT and develop a pragmatic method for SFT dynamic response analysis and structural dynamic performance optimization. The present chapter provides an overview of the general background and motivation for the study (Section 1.1), knowledge gaps (Section 1.2), research aims (Section 1.3), the thesis outline (Section 1.4), and introduction of the submerged floating tunnel project (Section 1.5).

1.1. MOTIVATION

In the past decades, great developments have been made in sea, fjord, and strait crossing technologies. Current solutions mainly include underwater tunnels (e.g., immersed tunnels, shield-bored tunnels, drill-and-blast tunnels) and sea bridges, and key technologies have made breakthroughs in some typical construction methods, such as the longest sea bridge: the Hong Kong-Zhuhai-Macau Bridge in China (55 km) (Li et al. 2015); the longest and deepest undersea tunnel: the Seikan Tunnel in Japan (23.3 km in length and 140 m in depth) (Ikuma 2005, Matsuo 1986), and the longest immersed tunnel: the Fehmarnbelt Tunnel, which will be constructed connecting Germany and Denmark (18 km) (Pedersen & Brøndum 2018). However, the challenges of transportation infrastructure using these conventional schemes in the marine environment increase with crossing length especially in large water depths and/or soft foundations. Therefore, a new type of infrastructure should be developed to improve the efficiency and capability of underwater transportation.

The submerged floating tunnel (SFT), also called an Archimedes Bridges, afloat in water with its buoyancy and support system to balance its self-weight, is regarded as one of the alternatives to underwater tunnels and sea bridges for wide and deep sea-crossings (Fig.1.1). The support system is composed of mooring lines, piles, or pontoons to limit motion and acceleration. One advantage of the SFT is that it reduces the total tunnel length compared with an immersed or bored tunnel, and hence, reduces construction cost; the SFT is more competitive than conventional sea bridges because it avoids severe wave and wind conditions or heavy ship traffic due to its submergence depth (generally 20~50 m (Wikipedia n.d., Faggiano et al. 2005)); In addition, the influence on the ecological environment is minimal compared with other underwater tunnels. Currently, the concept of the SFT has received strong attention and broad interest from both industry and academia, and many potential SFT construction sites in the world have been proposed in recent years, such as Høgsfjord in Norway (Remseth et al. 1999, Larssen & Jakobsen 2010); Qiandao Lake in China (Mazzolani et al. 2008); Sognefjord in Norway (Deng et al. 2020); Messina Strait in Italy (Faggiano et al. 2001, Martire et al. 2010); Funka Bay in Japan (Lu et al. 2011); Mokpo-Jeju in South Korea (Sam Han et al. 2016); Baja California in Mexico (Faggiano et al. 2016); Qiongzhou Strait in China (Yan et al. 2016, Shengzhong et al. 2016, Jiang et al. 2018); Scotland - Northern Ireland in UK (Catherine Kennedy 2020).

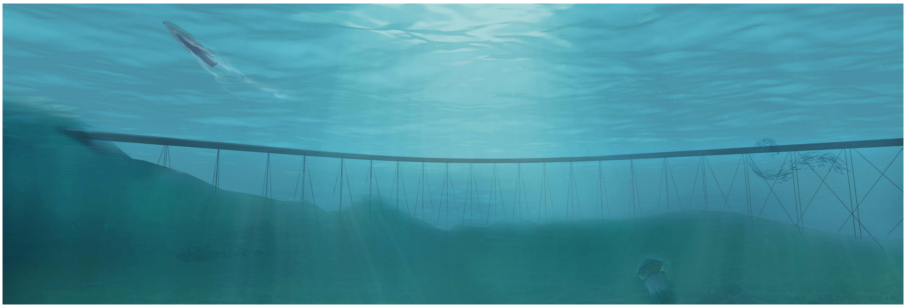

Figure 1.1: Sketch of submerged floating tunnel (CCCC SFT Technical Joint Research Team n.d.)

However, no prototype SFT has yet been built, and engineering design for an SFT is not addressed by existing civil engineering standards or guidelines. As an interdisciplinary technology integrating the knowledge of tunnel engineering, structural engineering, ocean engineering, geotechnical engineering, and materials engineering, etc., there are still a series of key scientific and engineering difficulties and challenges that have not been solved yet. Since the SFT is afloat in water subject to multiple environmental loads, complex fluid-structure interaction and dynamic response of an SFT under different hydrodynamic loads are key points for scientific research. Hydrodynamic interaction of the SFT, determining structural safety and reliability in the harsh environmental conditions, is the crucial issue requiring better understanding. The hydrodynamic loads, structural dynamic response, and structural configuration of the SFT interplay interact with each other, making the mechanism of dynamic response of the SFT rather complicated. For instance, different hydrodynamic loads excite dynamic response in different ways, and structural motions and deformations, in turn, disturb the surrounding flow field, and change the hydrodynamic loads acting on the SFT; structural parameters such as cross-sectional shape can drastically change hydrodynamic forcing on the SFT; hydrodynamic loads such as internal waves can alter structural buoyancy, and hence, change the buoyancy-weight ratio (BWR); structural parameters determine natural frequencies of the SFT and thus directly affect dynamic response of the SFT; severe dynamic response can be induced by fatigue damage and intrinsically change structural physical and mechanical properties. However, the impacts of different types of hydrodynamic loads on an SFT are still unclear, and how to ensure serviceability and safety of the SFT system during construction, operation, and maintenance subject to harsh environmental conditions remains a difficult issue.

1.2. KNOWLEDGE GAPS

Regarding dynamic response of an SFT subject to environmental loads, research should focus on motion of fluids and fluid forces acting on the SFT, dynamic response of the SFT, and measuremes to suppress the impacts of hydrodynamic loading on the SFT by optimizing structural parameters or adding external structures. The identified hydrodynamic loads in SFT engineering design generally include waves (e.g., surface waves, internal waves, ship waves) and currents (e.g., tidal currents, wind-driven currents, rip currents). In addition, the effects of extreme events and accidental loads (e.g., typhoons and tsunamis) should be assessed to ensure stability and safety of the SFT. In order to obtain the flow field at a specific SFT build site, field observations and large-scale oceanic model simulations need to be carried out. The mechanism of fluid-structure interaction (FSI) is key to clarifying the complex dynamic response of the SFT under various hydrodynamic loads.

Currently, research about hydrodynamic loads acting on SFTs is mainly restricted to ideal wave or current conditions (e.g., regular waves, steady current) (il Seo et al. 2015, Chen et al. 2018, Hong & Ge 2010, Kunisu 2010, Long et al. 2009, 2015, Oh et al. 2020, Budiman et al. 2016). These achievements cannot satisfy the requirements of serviceability and safety assessment for an SFT under more realistic, complex, and extreme ocean environments. Moreover, these experiments and mathematical models targeted a single SFT segment, short-span tube elements, or small-scale two-dimensional model tests (Deng et al. 2020, il Seo et al. 2015, Jin et al. 2018, Yang et al. 2020, Zou & Chen 2021), in which the local and global deformation characteristics of the SFT tube under complex interactions with waves and currents cannot be revealed. The small laboratory scale limits the generalizations of the achieved results due to the inability to simultaneously satisfy all the similitudes involved. Thus, dynamic response of a prototype SFT cannot be simply determined by scaled-down experimental tests. Furthermore, the SFT is inherently a nonlinear system coupling multiple components including the tunnel tube, mooring lines, and joints. However, in previous research about global dynamic response of the SFT (Deng et al. 2020, Mazzolani et al. 2008, Jin et al. 2018, Jin & Kim 2020, Mandara et al. 2016), structural nonlinearities were idealized by assuming of a continuous and rigid tunnel tube and neglecting segment joints in between. Therefore, dynamic response analysis of a prototype long span SFT composed of a tube-mooring-joint system should be systematically investigated. The impacts of forcing on the SFT in a complex ocean environment should raise more concern.

Regarding hydrodynamic load computation methods, empirical and theoretical models based on the Morison equation and diffraction theory have been extensively applied in previous research (Chen et al. 2018, Aashto 2010, Kunisu 2010, Jin et al. 2018, Chen et al. 2016, Lin et al. 2019, Lai 2007). However, each of these methods and its respective assumptions limits its range of application. The Morison equation for hydrodynamic load computation neglects diffraction effect by assuming that the fluid field is negligibly affected by the structure's dimensions, which is not always reasonable for large scale SFTs. Furthermore, the drag and inertial coefficients in the Morison equation are typically derived from laboratory experiments and restricted to simpler shapes, making it not generalizable for all structural geometries and all environmental conditions. Moreover, the Morison equation cannot provide flow field information in detail. For diffraction theory, an inviscid, irrotational, homogeneous, and incompressible fluid is assumed, and cannot directly include the effects of turbulence or viscosity on the flow. Therefore, more advanced and capable tools for dynamic response prediction of SFTs in the marine environment should be adopted. The computational fluid dynamics (CFD) approach is a high-fidelity and quantitative analysis tool for solving complex multi-physics interactions. It directly solves all related physical mechanisms (e.g., flow viscosity, wave diffraction and radiation) of the SFT without empirical assumptions based on experiments.

Flow-induced vibration (FIV) analysis is crucial for structural reliability and safety assessment because FIV can cause fatigue damage and structural failure (Luoa et al. 2015). Comprehension of FIV conditions of the SFT under different hydrodynamic loads is a key point in SFT engineering design. Since no SFT prototype has yet been built and few experimental studies of FIV prediction have been conducted, most of the previous research focused on vortex-induced vibration (VIV) of mooring lines or tethers, which can be characterized by intrinsic slender and flexible elements, as with risers and pipelines (Kamphuis 1998, Liu et al. 2020, Felisita et al. 2016, Wu et al. 2012, Chao et al. 2016, nan Sun et al. 2020). For tunnel tube vibration analysis, scale tests in laboratories were performed in previous research (Deng et al. 2020). However, accurate FIV prediction of a prototype-scale SFT can not be easily achieved by scale-down experimental models due to inconsistency in Reynolds numbers, vibration modes, and structural stiffness. Theoretical and semi-empirical methods such as wake oscillator models for VIV prediction are generally based on assumptions with empirical parameters obtained from experiments (Hong & Ge 2010, Wu et al. 2010, Passano et al. 2014, Vandiver & Li 2005). However, experimental data for the SFT that can be incorporated into semi-empirical tools for VIV prediction is rather limited, while data from risers and pipelines cannot be simply applied to the SFT due to its additional mooring system and different buoyancy weight ratio (BWR). Therefore, each method has its limitations and cannot be applied to a generalized application for an SFT. Regarding numerical simulations, the Finite Element Method (FEM) was adopted to explore mode competition and multi-mode VIV of the SFT (Chen et al. 2016). However, the SFT was simplified as a flexible cylinder considering exclusively sheared current conditions. Systematical studies of a long span SFT as a coupled tube-mooring-joint system to examine FIV conditions and structural dynamics with a more pragmatic and effective modelling technique are still absent.

In addition, structural optimization is a crucial topic noteworthy to investigate. Structural optimization has great potential for the engineering design and construction industry, with the objectives of improving structural physical and mechanical properties, mitigating the potential uncertainties, risks and structural failure, and saving construction costs. To minimize the dynamic response of an SFT subject to environmental loads, optimization of the SFT with the aim of suppressing dynamic response and increasing structural sustainability and reliability, requires the optimization of cross-section size, shape, and global configuration. The form finding method was applied to determine the optimal SFT cross-sectional shape with the minimal material use (van Marrewijk 2020). However, previous research about SFT cross-sectional shape optimization to increase hydrodynamic performance is scarce and mainly restricted to simple geometrical shapes such as circles, ellipses, polygons, and squares (Martire et al. 2009, Li & Jiang 2016, Li et al. 2018, Gang et al. 2018). A detailed parametric study and an effective optimization method for the SFT cross-section are lacking. Furthermore, research of a systematic structure configuration optimization process under various environmental loads is still absent. Effective approach for dynamic behaviour prediction and structural optimization of the SFT under various hydrodynamic loads remain question marks.

1.3. RESEARCH AIM AND QUESTION

The central research aim of this thesis is defined as

- To understand the dynamic response of a submerged floating tunnel subject to hydraulic loading.

The associated research objectives mainly include

- To determine hydrodynamic loads and internal forcing of a prototype SFT under various hydrodynamic conditions, especially concerning more complex and extreme hydrodynamics.

- To comprehend the effects of structural parameters on structural dynamic performance, and develop methods to optimize cross-sectional shape and structural configuration.

- To understand the dynamic response and FIV conditions of the SFT under various hydrodynamic loads in order to suppress or avoid structural resonance.

By addressing the central research question, the optimal cross-section geometry of the SFT will be firstly determined by minimizing the mean drag and the dynamic variability in the lift acting on the SFT. Furthermore, hydrodynamic loads acting on the SFT will be evaluated for structural safety. Most of the previous research (il Seo et al. 2015, Chen et al. 2018, Hong & Ge 2010, Kunisu 2010, Long et al. 2009, 2015, Oh et al. 2020, Budiman et al. 2016) adopted steady currents and regular waves in the selection of environmental conditions. However, assessment of the effect of extreme and disastrous loads (e.g. tsunamis, super typhoons, internal waves) on the SFT are lacking. These extreme hydraulic events exacerbate the structural vulnerability, being a key to assessing structural safety and reliability and solving technical challenges in the practical design. The hydrodynamic loads examined in this research are shown in Fig.1.2.

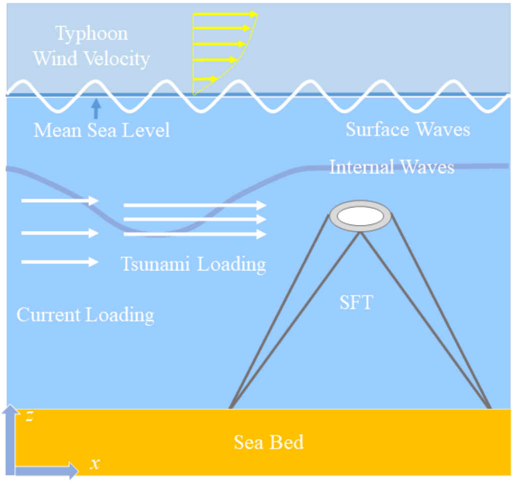

Figure 1.2: Main dynamic loads experienced by an SFT

After determination of the hydrodynamic loads, a global structural dynamic response analysis will be carried out. FIV is a crucial factor affecting structural dynamic behaviour and lifetime of the SFT by inducing structural fatigue damage and even sudden failure, which will be particularly focused on and carefully inspected in the evaluation of safety and durability of the SFT system. Finally, in order to suppress or avoid FIV, configuration optimization of an SFT coupled tube-joint-mooring system with the consideration of both structural parameters and hydrodynamic loads will be developed, accordingly.

Therefore, the central research question can be answered by considering following specific key questions.

What is the ideal cross-sectional shape and aspect ratio that contributes to minimizing the effects of hydrodynamic loads and construction costs? (Chapter 2)

How does an oceanic internal solitary wave (ISW) interact with a prototype SFT? What is the effect of oceanic ISW amplitude, the relative distance of the SFT to the pycnocline, the cross-sectional geometry of the SFT, and the density ratio of the two-fluid layers on the ISW-SFT interaction? (Chapter 3)

What are the impacts of extreme events on the SFT? How does the worst-case tsunami and typhoon affect the hydrodynamic forcing on an SFT? (Chapter 4)

How does a super long coupled tube-joint-mooring system respond under various hydrodynamic loads? What are FIV conditions for an SFT? What is the optimal SFT configuration for practical application? (Chapter 5)

1.4. SCOPE AND OUTLINE

This thesis focuses on the global dynamic response of a submerged floating tunnel and the related fluid-structure interaction issues. The main subtopics involve the optimization method for cross-sectional geometry of an SFT, estimation of hydrodynamic loads on an SFT under extreme events and internal wave conditions, FIV conditions of an SFT subject to currents and waves, and configuration optimization of the SFT system to mitigate severe vibrations. This research is carried out with high fidelity and computational efficiency through multiple, coupled numerical simulation methods(e.g., CFD, FEM, and machine learning). In line with the main subtopics and the research questions, the thesis is structured as follows, and Fig.1.3 displays the general overview and how each chapter is organized.

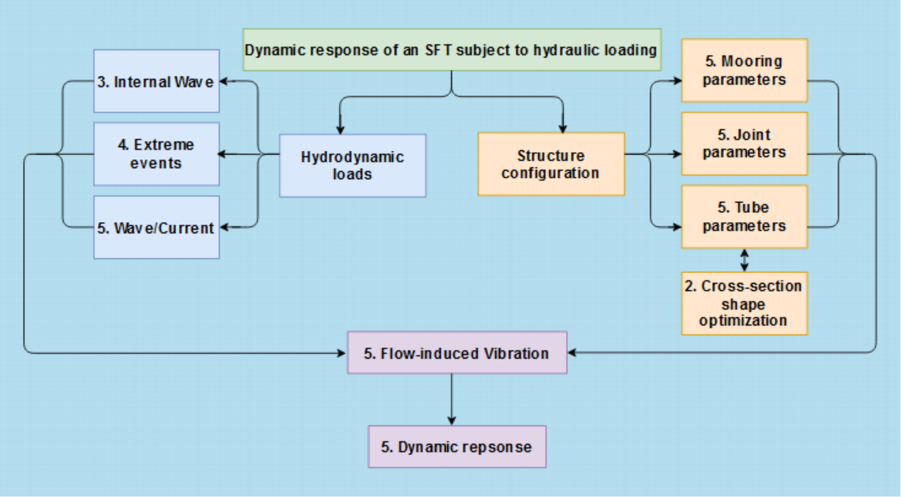

Figure 1.3: Dissertation overview (blue, purple, and yellow blocks represents the hydrodynamic loads related chapters, dynamic response related chapter, and structural configuration related chapters, respectively, and the number in each block indicates the chapter number)

Chapter 2 provides a method to parametrize the geometry of the SFT cross-section. In addition, a sensitivity analysis to the Bézier curve parameters is carried out under steady current conditions. The root mean square (RMS) lift and mean drag coefficients are considered objective functions and are optimized by a hybrid back propagation and genetic algorithm (BP-GA) structure. Furthermore, a reasonable aspect ratio of the SFT cross-section is determined by testing two formats of parametric Bézier curves.

Chapter 3 describes the method used to generate and propagate an oceanic ISW, and reveals interaction between the ISW and SFT by elucidating the velocity field evolution. A sensitivity analysis is carried out with indices including ISW amplitude, SFT cross-sectional shape, relative distance of the SFT to the pycnocline, and fluid density ratio, to figure out their effects on the ISW-SFT interaction.

Chapter 4 presents the wave and current characteristics induced by extreme events. The impacts of the worst-case tsunami and hindcast typhoon on hydrodynamic forcing of an SFT are analyzed. Moreover, the chapter compares hydrodynamic response of the proposed optimal SFT cross-section shape with other simpler shapes under extreme events.

Chapter 5 evaluates the dynamic response of the SFT and elucidates FIV conditions under current and wave conditions. The deflection and internal forcing of a prototype SFT coupled tube-joint-mooring system under extreme events and internal solitary wave conditions are computed. A pragmatic approach for the optimization of the configuration of a super long SFT subject to complex hydrodynamic loads is proposed. Multi-scale hydrodynamic models combined with FEM are established for structural dynamic response analysis. A sensitivity analysis of structural parameters is performed in order to determine how to modify the fundamental frequency such that it does not overlap with the hydrodynamic forcing frequency.

1.5. EMBEDDING IN THE SUBMERGED FLOATING TUNNEL PROJECT

The submerged floating tunnel project is a global collaborative research project commissioned by China Communications Construction Co., Ltd. (CCCC), consisting of various research institutes in China and the Netherlands. The CCCC Submerged Floating Tunnel Joint Technical Research Team defined 11 work packages in the SFT General Working Plan, which deal with general interests regarding the development of the SFT concept. In TU Delft, three PhD projects covering two work packages are identified.

- **Dynamic response of the SFT under hydraulic loading - with the aim of identification of hydrodynamic loads, analysis of structural dynamic response, and structural optimization (by Pengxu Zou)**.

- The risk and reliability analysis of the SFT - with the aim to perform a qualitative characterization of the potential risks in an SFT and to obtain a quantitative estimation of the probability of failure and reliability of an SFT (by Gina Torres and Marcel ‘t Hart).

The findings of this dissertation can enhance the understanding of hydrodynamic loading on the SFT, providing references for dynamic response assessment of the SFT, and contributing to further structure reliability and safety assessment for the SFT concept.

REFERENCES

Aashto (2010), *AASHTO LRFD Bridge Design Specifications.*

Budiman, E., Suswanto, B., Wahyuni, E. & Raka, I. G. (2016), 'Experiments on snap force in tethers of submerged floating tunnel model under hydrodynamic loads in case of shallow water', *ARPN Journal of Engineering and Applied Sciences* **11**(24).

Catherine Kennedy (2020), 'Floating underwater tunnel proposed as alternative Irish Sea link'.

CCCC SFT Technical Joint Research Team (n.d.), 'SFT'.

Chao, C. F., Xiang, Y. Q., Yang, Y., He, Y. L. & Wang, Z. (2016), 'Cables dynamic response experiment of submerged floating tunnel based on fluid-structure interaction', *Zhendong Gongcheng Xuebao/Journal of Vibration Engineering* **29**(4).

Chen, W., Li, Y., Fu, Y. & Guo, S. (2016), On Mode Competition during VIVs of Flexible SFT's Flexible Cylindrical Body Experiencing Lineally Sheared Current, *in* 'Procedia Engineering'.

Chen, Z., Xiang, Y., Lin, H. & Yang, Y. (2018), 'Coupled vibration analysis of submerged floating tunnel system in wave and current', *Applied Sciences (Switzerland)* .

Deng, S., Ren, H., Xu, Y., Fu, S., Moan, T. & Gao, Z. (2020), 'Experimental study of vortex-induced vibration of a twin-tube submerged floating tunnel segment model', *Journal of Fluids and Structures* .

Faggiano, B., Landolfo, R. & Mazzolani, F. (2001), 'Design and modelling aspects concerning the submerged floating tunnels: an application to the messina strait crossing', *Krobeborg. Strait Crossing* pp. 511–519.

Faggiano, B., Landolfo, R. & Mazzolani, F. (2005), The sft: an innovative solution for waterway strait crossings, *in* 'IABSE Symposium Report', Vol. 90, International Association for Bridge and Structural Engineering, pp. 36–42.

Faggiano, B., Panduro, J., Rosas, M. T. & Mazzolani, F. M. (2016), The Conceptual Design of a Roadway SFT in Baja California, Mexico, *in* 'Procedia Engineering', Vol. 166.

Felisita, A., Gudmestad, O. T., Karunakaran, D. & Martinsen, L. O. (2016), A review of VIV responses of steel lazy wave riser, *in* 'Proceedings of the International Conference on Offshore Mechanics and Arctic Engineering - OMAE'.

Gang, L., Xiao-jun, Z. & Jian-xun, C. (2018), 'The Dynamic Response of an Experimental Floating Tunnel with Different Cross Sections under Explosive Impact', *Journal of Coastal Research* .

Hong, Y. & Ge, F. (2010), Dynamic response and structural integrity of submerged floating tunnel due to hydrodynamic load and accidental load, *in* 'Procedia Engineering'.

Ikuma, M. (2005), 'Maintenance of the undersea section of the Seikan Tunnel', *Tunnelling and Underground Space Technology* **20**(2).

il Seo, S., suk Mun, H., ho Lee, J. & ha Kim, J. (2015), 'Simplified analysis for estimation of the behavior of a submerged floating tunnel in waves and experimental verification', *Marine Structures* .

Jiang, B., Liang, B., Faggiano, B., Iovane, G. & Mazzolani, F. M. (2018), Feasibility study on a submerged floating tunnel for the Qiongzhou strait in China, *in* 'Maintenance, Safety, Risk, Management and Life-Cycle Performance of Bridges - Proceedings of the 9th International Conference on Bridge Maintenance, Safety and Management, IABMAS 2018'.

Jin, C., Kim, J. M.-H., Choi, J. & Park, W.-S. (2018), Coupled dynamics simulation of submerged floating tunnel for various system parameters and wave conditions, *in* 'International Conference on Offshore Mechanics and Arctic Engineering', Vol. 51265, American Society of Mechanical Engineers, p. V07AT06A050.

Jin, C. & Kim, M. H. (2020), 'Tunnel-mooring-train coupled dynamic analysis for submerged floating tunnel under wave excitations', *Applied Ocean Research* .

Kamphuis, J. (1998), 'Hydrodynamics around cylindrical structures', *Coastal Engineering* .

Kunisu, H. (2010), Evaluation of wave force acting on Submerged Floating Tunnels, *in* 'Procedia Engineering'.

Lai, W. H. (2007), 'Transient dynamic response of submerged sphere shell with an opening subjected to underwater explosion', *Ocean Engineering* **34**(5-6).

Larssen, R. M. & Jakobsen, S. E. (2010), Submerged floating tunnels for crossing of wide and deep fjords, *in* 'Procedia Engineering'.

Li, K. & Jiang, X. (2016), Research on Section Form of Submerged Floating Tunnels Considering Structural Internal Force Optimization under Fluid Action, *in* 'Procedia Engineering'.

Li, K., Li, Q., Zhou, X. & Fan, Z. (2015), 'Durability Design of the Hong Kong–Zhuhai–Macau Sea-Link Project: Principle and Procedure', *Journal of Bridge Engineering* **20**(11).

Li, Q., Jiang, S. & Chen, X. (2018), 'Experiment on Pressure Characteristics of Submerged Floating Tunnel with Different Section Types under Wave Condition', *Polish Maritime Research* .

Lin, H., Xiang, Y. & Yang, Y. (2019), 'Vehicle-tunnel coupled vibration analysis of submerged floating tunnel due to tether parametric excitation', *Marine Structures* .

Liu, G., Li, H., Qiu, Z., Leng, D., Li, Z. & Li, W. (2020), 'A mini review of recent progress on vortex-induced vibrations of marine risers'.

Long, X., Ge, F. & Hong, Y. (2015), 'Feasibility study on buoyancy–weight ratios of a submerged floating tunnel prototype subjected to hydrodynamic loads', *Acta Mechanica Sinica/Lixue Xuebao* **31**(5).

Long, X., Ge, F., Wang, L. & Hong, Y. (2009), 'Effects of fundamental structure parameters on dynamic responses of submerged floating tunnel under hydrodynamic loads', *Acta Mechanica Sinica/Lixue Xuebao* **25**(3).

Lu, W., Ge, F., Wang, L., Wu, X. & Hong, Y. (2011), 'On the slack phenomena and snap force in tethers of submerged floating tunnels under wave conditions', *Marine Structures* **24**(4).

Luoa, G., Chen, J. & Zhou, X. (2015), 'Effects of Various Factors on the Viv-Induced Fatigue Damage In The Cable Of Submerged Floating Tunnel', *Polish Maritime Research* **22**(4).

Mandara, A., Russo, E., Faggiano, B. & Mazzolani, F. M. (2016), Analysis of Fluid-structure Interaction for a Submerged Floating Tunnel, *in* 'Procedia Engineering'.

Martire, G., Faggiano, B., Esposto, M., Mazzolani, F., Zollo, A. & Stabile, T. (2009), The seismic response of submerged floating tunnel under multisupport excitations, *in* 'Proceedings of the XIII Congress on Earthquake Engineering in Italy ANIDIS 2009'.

Martire, G., Faggiano, B., Mazzolani, F. M., Zollo, A. & Stabile, T. A. (2010), Seismic analysis of a SFT solution for the Messina Strait crossing, *in* 'Procedia Engineering', Vol. 4.

Matsuo, S. (1986), 'An overview of the Seikan tunnel project', *Tunnelling and Underground Space Technology incorporating Trenchless* **1**(3-4).

Mazzolani, F. M., Landolfo, R., Faggiano, B., Esposto, M., Perotti, F. & Barbella, G. (2008), 'Structural analyses of the submerged floating tunnel prototype in Qiandao Lake (PR of China)', *Advances in Structural Engineering* .

nan Sun, S., bin Su, Z., fen Feng, Y. & yi Xu, X. (2020), 'Parametric Vibration Analysis of Submerged Floating Tunnel Tension Legs', *China Ocean Engineering* **34**(1).

Oh, S. H., Park, W. S., Jang, S. C., Kim, D. H. & Ahn, H. D. (2020), Physical experiments on the hydrodynamic response of submerged floating tunnel against the wave action, *in* 'Proceedings of the 7th International Conference on Asian and Pacific Coasts, APAC 2013'.

Passano, E., Larsen, C. M., Lie, H. & Wu, J. (2014), 'VIVANA theory manual', *Norwegian Marine Technology Research Institute: Trondheim, Norway. Current profiles with higher velocities produce high damage at both the riser's upper catenary and buoyancy section due to high current exposure at the shallower water depth and the high c* .

Pedersen, S. K. & Brøndum, S. (2018), 'Fehmarnbelt fixed link: The world's longest road and rail immersed tunnel', *Proceedings of the Institution of Civil Engineers: Civil Engineering* **171**(5).

Remseth, S., Leira, B. J., Okstad, K. M., Mathisen, K. M. & Haukås, T. (1999), 'Dynamic response and fluid/structure interaction of submerged floating tunnels', *Computers and Structures* **72**(4).

Sam Han, J., Won, B., Park, W. S. & Ko, J. H. (2016), ‘Transient response analysis by model order reduction of a Mokpo-Jeju submerged floating tunnel under seismic excitations’, *Structural Engineering and Mechanics* **57**(5).

Shengzhong, W., Xiang, C., Qinxi, L. & Gengren, C. (2016), Research on Type Selection of Submerged Floating Tunnel of Qiongzhou Strait, *in* ‘Procedia Engineering’.

van Marrewijk, C. (2020), ‘Form finding for a submerged floating tunnel: The clever cross-section for coastal crossings’.

Vandiver, J. K. & Li, L. (2005), ‘Shear7 V4. 4 program theoretical manual’, *Massachusetts Institute of Technology* .

Wikipedia (n.d.), ‘Submerged floating tunnel’.

Wu, X., Ge, F. & Hong, Y. (2010), Effect of travelling wave on vortex-induced vibrations of submerged floating tunnel tethers, *in* ‘Procedia Engineering’.

Wu, X., Ge, F. & Hong, Y. (2012), ‘A review of recent studies on vortex-induced vibrations of long slender cylinders’, *Journal of Fluids and Structures* .

Yan, H., Zhang, F. & Yu, J. (2016), The Lectotype Optimization Study on Submerged Floating Tunnel Based Delphi Method, *in* ‘Procedia Engineering’.

Yang, Z., Li, J., Zhang, H., Yuan, C. & Yang, H. (2020), ‘Experimental study on 2D motion characteristics of submerged floating tunnel in waves’, *Journal of Marine Science and Engineering* **8**(2).

Zou, P. & Chen, L. (2021), The coupled tube-mooring system sft hydrodynamic characteristics under wave excitations, *in* ‘Proceedings of the 14th International Conference on Vibration Problems’, Springer, pp. 907–923.

2

OPTIMIZATION OF CROSS SECTION BASED ON PARAMETRIC BÉZIER CURVES

The cross-section geometry of a submerged floating tunnel (SFT) has a large effect on hydrodynamic characteristics, structural behavior, and service level, making the tunnel cross section the primary factor in optimizing efficiency. Selecting a suitable cross-sectional shape for an SFT is crucial to minimize the hydrodynamic loads acting on the SFT, increase the safety and reliability of the SFT system, and save construction cost. Based on a parametric Bézier curve dynamically comprising the leading-edge radius, tunnel height and width to define the SFT geometry, a sensitivity analysis of the Bézier curve parameters with prototype dimensions is conducted by applying Computational Fluid Dynamics (CFD), and the pressure distribution around the SFT cross-section surface is analyzed in this chapter. In addition, an effective tool for cross-section optimization is proposed. The key question concerning the ideal cross-sectional shape and aspect ratio that contributes to minimizing the effects of hydrodynamic loads and construction costs is discussed in this chapter. The optimal SFT cross-section forms the basis for dynamic response assessment of an SFT, and lead to research of the impacts of hydrodynamic loads including internal waves (Chapter 3) and extreme events (Chapter 4) on the SFT in Chapter 5. The highlights of this chapter are:

- *A reliable approach based on a dynamically oriented parametric Bezier curve is the first method we use to define the submerged floating tunnel cross-section.*
- *A theoretical method comprising the Kármán vortex street parameters can be employed to verify the CFD results.*

This chapter has been published as: Zou, P., Bricker, J., Uijttewaal, W. (2020). Optimization of submerged floating tunnel cross section based on parametric Bézier curves and hybrid backpropagation-genetic algorithm. ***Marine Structures***, 74, 102807; Zou, P., Bricker, J. D., Uijttewaal, W. (2021). Submerged floating tunnel cross-section analysis using a transition turbulence model. ***Journal of Hydraulic Research***, 1-13.

- *Hybrid Backpropagation - Genetic Algorithm is an effective tool to optimize the combinations of Bézier curve parameters and predict the optimal submerged floating tunnel cross-section.*
- *A rational aspect ratio range of the cross-section under tidal flow conditions is provided.*

2.1. INTRODUCTION

The submerged floating tunnel (SFT), shown in Fig.2.1, also called “Archimedes Bridge”, is a new type of sea crossing that takes advantage of buoyancy to support its weight, and a mooring system to balance the residual buoyancy and limit the displacement of the SFT tube (Ahrens 1997, Lin, Xiang & Yang 2019). Since the concept was brought forward, research is still limited to theoretical and small-scale experimental verification, and no prototype has yet been built (Li & Jiang 2016).

The cross-section geometry of the SFT has a large effect on hydrodynamic characteristics, space utilization, structural behavior, service level and construction cost, making the geometry a primary factor in optimizing efficiency and thus a priority to be optimized at the feasibility analysis stage of design. Moreover, due to the possibility of bidirectional ambient flow incident on both leading and trailing edges, potential flow theory and the Kutta condition (Crighton 1985) applied in traditional airfoil optimization design cannot be used due to flow separation from the bluff body, which makes the flow field complex.

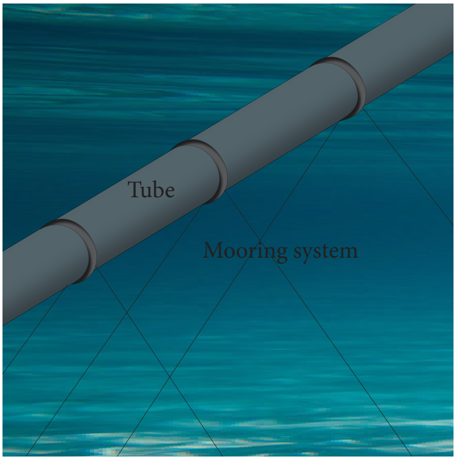

Figure 2.1: Schematic configuration of an SFT system

Li et al. (Li, Jiang & Chen 2018) conducted an experiment to compare the pressure characteristics of SFT’s with circular, elliptical and polygonal sections under wave impacts, and concluded that the circular section experiences the largest wave forces. Li and Jiang (Li & Jiang 2016) conducted numerical simulations to compare the pressure distributions of two cross sections by combining fluid mechanical calculation and structural analysis, concluding that an elliptical section experiences smaller displacements and stress than a rectangular section. Gang et al. (Gang et al. 2018) compared rectangular, circular, and elliptical floating tunnel cross-section forms, and determined the response to an explosion shock wave by using the finite element software LS-DYNA (Murray et al. 2007). Van Marrewijk (van Marrewijk 2020) applied form finding method to determine the optimal SFT cross-sectional shape with the minimal material use. Since research about SFT cross sections is scarce, geometrical optimization and applications from other engineering fields such as aerospace and mechanical engineering are helpful. Hajabdollahi et al. (Hajabdollahi et al. 2012) used a Non-dominated Sorting Genetic Algorithm-II (NSGA-II) to maximize heat transfer rate and fin efficiency for a fin geometry optimization. Basumatary et al. (Basumatary et al. 2018) modified and optimized a conventional two-bladed Savonius water turbine section by considering design parameters including gap width and overlap ratio, using CFD solvers to develop a new, combined lift-drag based blade design method. Wang and Lu (Wang & Lu 2018) presented a new cross section based on a meridian surface optimization strategy with the integration of Medial Axis Transform (MAT) design theory, CFD analysis, Central Composite Design (CCD), Response Surface Method (RSM) and NSGA-II. Lee et al. (Lee et al. 2013) employed the equivalent static load method for non-linear static response structural optimization (ESLSO) to determine workpiece shape in the forging process. Garg et al. (Garg et al. 2019) used a high-fidelity hydrostructural solver combined with a gradient-based optimizer to conduct numerical predictions compared with experimental measurements for a baseline NACA 0009 hydrofoil and an optimized hydrofoil.

Based on SFT cross-section analysis to date, the elliptical cross section has good hydrodynamic characteristics due to its streamlined shape compared with a square bluff shape (Li & Jiang 2016). Though many simple sections including circle, ellipse, polygon, and square have been assessed as SFT cross sections, there is still a need to conduct a detailed parametric study to determine an optimal shape. This chapter is structured as follows. In section 2.2, an SFT cross-section profile with various geometries is determined by a parametric Bézier curve (Bézier 1974)(Wang et al. 2019). Section 2.3 validates the CFD model against a laboratory experiment and theory. The main hydrodynamic characteristics including drag (C_d) and lift coefficients (C_l) are obtained by the ANSYS Fluent version 19.1 CFD solver (ANSYS 2019) applied in a high-performance computing (HPC) cluster to run parallel computation tasks. The dependence of average C_d and C_l magnitude on the Bézier curve parameters is presented in section 2.4. Section 2.5 applies a neural network (NN) optimized by genetic algorithm (GA) to relate tunnel cross-section parameters with optimal hydrodynamic properties, and further verifies this by numerical simulations. Section 2.6 conducts sensitivity analysis of aspect ratio with two types of Bézier curve profiles to determine a reasonable aspect ratio for an SFT.

2.2. PARAMETRIC DESIGN OF TUNNEL CROSS-SECTION

2.2.1. PARAMETRIC BÉZIER CURVE

The Bézier-PARSEC (BP) curve method is one of the most common parametric design methods for airfoils, because it tends to minimize the drag force of the geometry. The BP curve is developed to extend and improve the typical Bezier parameterization, which has been applied frequently in airfoil design (Jung et al. 2016, Nikolaev 2019). The BP curve combines the advantages of both Bézier variables and PARSEC parameters, to reduce the nonlinear interaction among parameters, making the parameters directly link to the objective function, and avoiding the second-order discontinuity problem. Bézier curves have a limited number of degrees of freedom determined by their control points and improve the convergence rate for aerodynamic optimization using Differential Evolution (Derksen & Rogalsky 2010). Moreover, it is desirable to determine parameters such as the leading-edge radius and tunnel height, which affect lift and drag, by using the PARSEC parameters (Rogalsky et al. 2000). As the BP curve method sees widespread use in airfoil design, it is the first method we use to define the SFT cross-section geometry (Zou et al. 2020, 2021). A BP parameterization using a third degree Bezier curve and a quadrant comprising of four control points is applied to define the SFT's geometry, given by Eq. 2.1.

$$\begin{cases} x(u) = -x_0 u^3 + 3x_1(u+1)u^2 - 3x_2(u+1)^2 u + x_3(u+1)^3 \\ y(u) = -y_0 u^3 + 3y_1(u+1)u^2 - 3y_2(u+1)^2 u + y_3(u+1)^3 \end{cases} \tag{2.1}$$

where u is a variable with the range of -1~0.

In this study, however, due to the possibility of bi-directional (i.e., tidal) flow, the leading and trailing halves of the SFT cross section are designed to be symmetric. To describe the tunnel geometry, four control points in each quadrant are considered as variables. These parametric Bézier curve using leading-edge BP profile is shown in Fig.2.2(a). The four control points that determine the shape of one quadrant of the SFT cross section are given by Eq. 2.2.

$$\begin{cases} x_0 = -x_t, y_0 = 0 \\ x_1 = -x_t, y_1 = b \\ x_2 = -x_t + 3b^2/2r, y_2 = y_t \\ x_3 = 0, y_3 = y_t \end{cases} \tag{2.2}$$

where x_t and y_t are half of the SFT's width and height, respectively, r is leading-edge radius, and b is Bezier curve parameters. b is subject to the following restriction

$$0 < b < \min(y_t, \sqrt{2rx_t/3}) \tag{2.3}$$

Since Bezier parameters are standard in airfoil design, a detailed derivation of these parameters and constraint conditions can be found in Rogalsky (Rogalsky 2004).

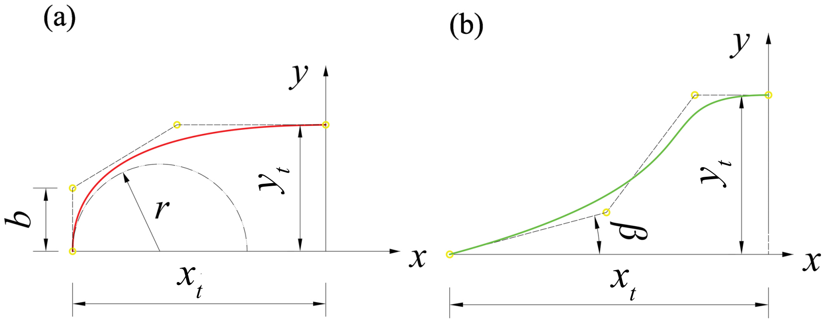

Figure 2.2: Control points of the third-degree Bézier curves of each quadrant. (a) Leading-edge BP curve; (b) Trailing-edge BP curve

2.2.2. DIMENSION LIMITATION

Referring to the current feasibility study and possible considerations of the traffic volume for the SFT cross section (Tveit 2000, Larssen & Jakobsen 2010, Muhammad et al. 2017), two 3.5 m wide lanes and a curb or sidewalk of width R on either side should be considered to meet the requirement for a typical two-lane tunnel (Fig.2.3). Based on the guidelines of AASHTO (AASHTO 2018), the total clearance between walls should be a minimum of 9 m, and the vertical clearance H should be a minimum of 4.3 m or 4.9 m.

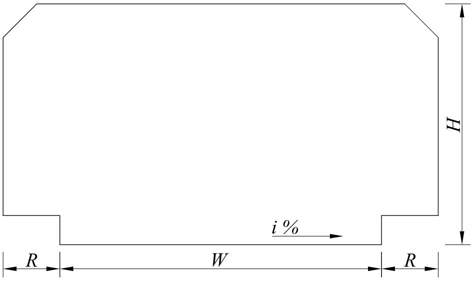

Figure 2.3: Typical two-lane tunnel cross section, i = slope, W = width clearance, H = vertical clearance, R = sidewalk width

2.3. MODELING VALIDATION

In this section, firstly, the performance metrics of hydrodynamic characteristics are defined; Secondly, grid independent limit (GIL) test is conducted to obtain grid convergence. Thirdly, the applied turbulence model in the CFD analysis is introduced. Finally, the CFD results are validated against experimental data and theoretical solutions.

2.3.1. PERFORMANCE METRICS

For hydrodynamic characteristics of an SFT cross section design, the essential parameters are drag and lift coefficients. Due to the uncertainty of current velocity and direction, the lift or drag force of the tunnel cross section exerted by a current can vary substantially, possibly causing excessive loading or fatigue damage to the mooring system, and also difficulty of operation due to the need for regulating ballast water to balance the variable lift force. Hence, the optimization objectives are to decrease the fluctuation amplitude of lift and drag forces. Both the drag and lift forces can be expressed with non-dimensional force coefficients, C_d and C_l, given in Eq. 2.4.

$$C_{l,d} = \frac{F_{l,d}}{\frac{1}{2}\rho U^2 W} \tag{2.4}$$

where $F_{l,d}$ is the lift or drag force per unit meter.

Since the fluctuation amplitude of C_d is small compared with C_l, and the fluctuation amplitude variation of C_l acts as a fatigue load on the mooring system, the variability of C_l is represented by its RMS $C_{l,rms}$, which represents how much the lift coefficient is oscillating. The RMS is given by Eq. 2.5

$$x_{rms} = \sqrt{\frac{\sum_{i=1}^{n} x_i^2}{n}} \tag{2.5}$$

where x_i is a variable comprising a time series of data.

For C_d and S_t, the mean value is much larger than the fluctuation, so the mean (not the RMS) was calculated. To obtain reliable statistics and allow model spin-up time, an unsteady simulation of 4000 non-dimensional time steps is performed and the last 600 time steps are used. S_t is calculated from adjacent peaks of the lift coefficient time series. The objective of the SFT cross-section shape optimization is to minimize $C_{l,rms}$ and $C_{d,m}$.

2.3.2. GRID INDEPENDENT LIMIT TEST

SFT cross section dimensions $H = 5$ m and $W = 10$ m, with an aspect ratio $H/W = 0.5$, are chosen for analysis in this study. Since here we focus mainly on the cross-section shape, it should be noted that in the actual tunnel cross section design, requirements for minimum lateral and vertical clearance must also be met. Each quadrant of parametric Bézier curves is defined by 4 control points. To freeze the aspect ratio of the tunnel cross section, the locations of the leading edge and trailing edge, and the height of the tunnel, are kept fixed. The junction between the upper and lower curves at the leading edge should have the same leading-edge radius to avoid divergence of calculation. Due to the fixed length and height of the cross section (aspect ratio = 0.5), y_{low} can be determined by $H - y_{up}$ (Fig.2.2(b)). As the tunnel profile is comprised of the upper and lower halves and the symmetrical shape of leading and trailing halves, the remaining variables are: y_{up}, r, b_{up} and b_{low}.

Table 2.1 shows the GIL test result for the SFT cross-section profile with parameters $b_{up} = b_{low} = 1$ m, $r = 4$ m, $y_{up} = 2.5$ m under a uniform cross-flow velocity of 0.1 m/s.

Table 2.1: Mesh size for the GIL test, S is cell size, N_{Cells} is cell number

S_{max} (m)	S_{min} (m)	N_{Cells}	Y^+	$C_{d,m}$	$C_{l,rms}$
2	0.03	27572	120~180	0.116	0.102
2	0.01	54416	40~70	0.140	0.153
1	0.01	137990	40~70	0.142	0.156
0.5	0.01	376768	40~70	0.143	0.157

It shows that the wall Y^+ of all the cases are below 300, which is within the acceptable range (Kuzmin et al. 2007), and it signifies the standard wall function condition and the quality of the minimum mesh size are sufficient. The maximum element size (1 m or 0.5 m) seems to have almost no influence on C_d or C_l, proving that numerical stability and mesh size convergence are achieved (Fig.2.4). Hence the maximum element size 1m and the minimum element size 0.01 m are chosen for all analyzed cases, with a minimum orthogonality of 0.41 after mesh improvement.

As the unsteady Reynolds-averaged Navier-Stokes (URANS) calculation has a good accuracy compared with steady RANS (Catalano et al. 2003), URANS is applied in this

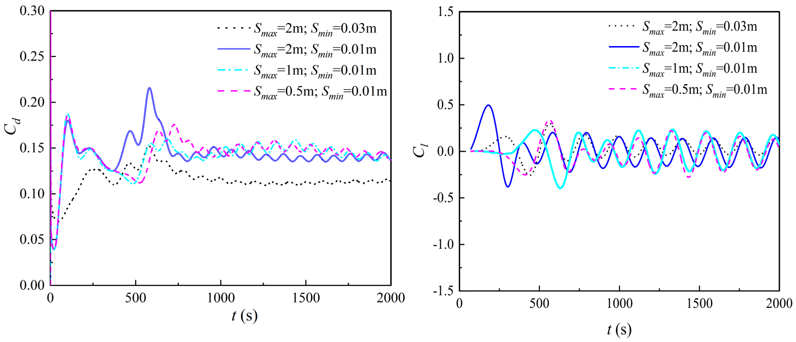

(a) C_d GIL test **(b) C_l GIL test**

Figure 2.4: GIL test results

study. The Pressure-Implicit with Splitting of Operators (PISO) algorithm is applied for pressure-velocity coupling as it maintains a stable calculation with a larger time step with neighbor correction, and it is highly recommended in transient simulations compared with SIMPLE and SIMPLEC (Van Doormaal & Raithby 1984, Zhang et al. 2016, ANSYS 2019). The boundary condition at the sides and cylinder wall is a rough wall layer approximation. The “velocity-inlet” and the “outlet” boundary conditions are employed at the inlet and exit boundaries, respectively. The inlet boundary has a turbulence intensity of 2.8% with a turbulent length scale of 10 m. The wall roughness of the tunnel surface is 3 mm, based on actual concrete. The inlet and upper/lower boundaries are set 5W away from the cylinder axis, and the outlet is set 15W away from the cylinder. The maximum CFL number is 0.5, and the non-dimensional time step $\delta_t U/W$ is kept at 4×10^{-4}. The simulation domain is shown in Fig.2.5.

Figure 2.5: Schematic diagram of the computational domain, W is width of the SFT cross-section

2.3.3. TURBULENCE MODELING

The $k-\epsilon$ turbulence model generally produces accurate results in high Reynolds number conditions (Ong et al. 2009, Lin, Lu & Lin 2019). The RNG $k-\epsilon$ model gives more accurate simulations for dramatically irregular geometry with flow separation via an additional term in its ϵ equation. Also, an analytical formula for the turbulent Prandtl number is provided, in contrast to the constant value used in the standard $k-\epsilon$ model. These features make the RNG $k-\epsilon$ model more accurate and reliable than the standard $k-\epsilon$ model for a wider range of flows. The RNG $k-\epsilon$ model transport equation can be expressed as Eq. 2.6.

$$\begin{cases} \frac{\partial(\rho k)}{\partial t}+\frac{\partial(\rho k u_i)}{\partial x_i}=\frac{\partial(\alpha_k \mu_{eff}\frac{\partial k}{\partial x_j})}{\partial x_j}+G_k+G_b-\rho\varepsilon-Y_M+S_k \\ \frac{\partial(\rho \varepsilon)}{\partial t}+\frac{\partial(\rho \varepsilon u_i)}{\partial x_i}=\frac{\partial(\alpha_\varepsilon \mu_{eff}\frac{\partial \varepsilon}{\partial x_j})}{\partial x_j}+C_{1\varepsilon}\frac{\varepsilon}{k}(G_k+C_{3\varepsilon}G_b)-C_{2\varepsilon}\rho\frac{\varepsilon^2}{K}-R_\varepsilon+S_\varepsilon \end{cases} \tag{2.6}$$

where C_1= 1.42; C_2= 1.68; μ_{eff} is effective viscosity; ρ is fluid density; G_k, G_b are turbulence generation terms, Y_m is the contribution of the fluctuating dilatation of compressible turbulence to the overall dissipation rate; S_k, S_ϵ are source terms; k is a source term; ϵ is turbulence dissipation rate.

The additional term in the ϵ equation is given by Eq.2.7

$$R_\varepsilon=\frac{C_\mu\rho\eta^3(1-\eta/\eta_0)}{1+\beta\eta^3}\frac{\varepsilon^2}{k} \tag{2.7}$$

where $\eta \equiv S_k/\varepsilon$, $\eta_0=4.38$,$\beta=0.012$.

The turbulent viscosity is computed by combining k with ϵ as follows in Eq. 2.8.

$$\mu_t=\rho C_\mu\frac{k^2}{\varepsilon} \tag{2.8}$$

where $C_{1\varepsilon}$ = 1.42, $C_{2\varepsilon}$ =1.68, and C_μ =0.085 are all dimensionless user-adjustable parameters derived using the RNG theory. Hence, a numerical model integrating the two-dimensional, incompressible flow, unsteady RNG $k-\epsilon$ turbulence model with the standard wall function is adopted.

2.3.4. NUMERICAL VERIFICATION

As one of the canonical and classical problems in fluid mechanics, the cylinder-flow case is of great interest and importance for a wide range of offshore engineering applications, including marine pipelines, offshore platform support legs, and thus also the SFT. Considering the prototype scale of the SFT cross section and current conditions in deep sea, the Reynolds number can be higher than 1×10^6, which encompasses both supercritical ($4\sim5\times10^5$ and $2.5\sim4\times10^6$) and transcritical ($>2.5\sim4\times10^6$) flow regimes (James et al. 1980). To date, both experimental tests and numerical simulations of circular cylinders at very high Reynolds number flows are lacking due to the complexity of the flow characteristics and limitations of laboratory equipment. Herein Reynolds number of 1×10^6 is chosen for validation and simulation in the optimal cross section analysis, because sufficient experimental data is available.

To evaluate the model's validity under very high Reynolds numbers, simulated average drag and pressure coefficients are compared with published experimental results by James et al. (James et al. 1980). A cylinder within a rectangular domain is used under the same Reynolds number and relative surface roughness (the ratio of surface roughness to model diameter). The Reynolds number Re (expressed as Eq.2.9), based on the upstream flow speed $U = 0.1$ m/s and a cylinder diameter of 10 m, has a magnitude of 1×10^6.

$$R_e = \frac{\rho U d}{\mu} \tag{2.9}$$

where U is upstream flow velocity; μ is viscosity; d is the characteristic length, which is diameter of the cylinder or chord length applied in airfoil design. Hereinafter the clearance width W is used for the SFT cross-section analysis.

The mean pressure coefficient C_p (expressed as Eq.2.10) distribution around the cylinder compared with the experimental data measured in the counterclockwise direction is shown in Fig.2.6 (a).

$$C_p = \frac{\rho - p_{ref}}{\frac{1}{2}\rho U^2} \tag{2.10}$$

where p is the pressure on the cylinder, and p_{ref} is the reference pressure.

It is noted that the mean C_p curves of both the physical model test and numerical result show the separation point occurring approximately 120° aft of the forward stagnation point, which is a typical characteristic of the supercritical flow régime, indicating the presence of separation in the wake region. A narrower wake can exist caused by boundary layer transition, reattachment and backward turbulent separation; this is associated with lower drag and is commonly known as the drag crisis.

Fig.2.6 (b) shows the results for validation concerning the drag coefficient. In order to verify the drag coefficient distribution clearly in the drag crisis region, Reynolds number from 6×10^5 to 1×10^7 are also added for the validation. The experimental data and numerical results follow the same trend with reasonable agreement.

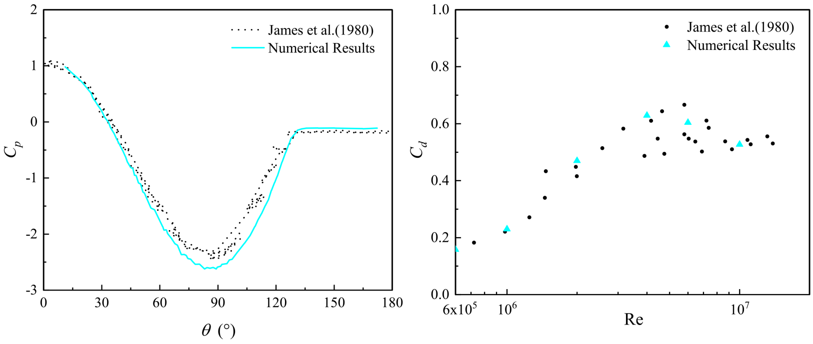

(a) C_p **validation**

(b) C_d **validation**

Figure 2.6: Verification of numerical results against the laboratory experiments of James et al. (1980)

In order to validate simulated lift, CFD results were compared with a theoretical method derived by Sallet (Sallet 1973), which comprises expressions for the fluctuating lift coefficient of any bluff cylindrical body as a function of Kármán vortex street parameters (Sallet 1973): S_t, l, and h by employing potential flow theory. The equations for

Table 2.2: Comparison between numerical and theoretical lift coefficients

r (m)	C_d	S_t	l (m)		C_l		
			Theoretical result	Numerical result	Theoretical result	Numerical result	Relative difference
0.1	0.234	0.213	22.73	12.55	0.191	0.322	40.8%
0.5	0.156	0.216	22.64	12.00	0.131	0.149	11.8%
1.0	0.151	0.221	22.11	11.98	0.130	0.139	6.1%
1.5	0.151	0.222	22.01	11.97	0.130	0.137	5.1%
2.5	0.150	0.223	21.91	11.63	0.131	0.129	1.6%
4.5	0.154	0.220	22.20	11.94	0.131	0.131	0.0%

C_d and C_l are shown as Eq. 2.11 and 2.12, assuming von Kármán's stability criterion of vortex spacing ratio $h/l = 0.280549$.

$$S_t^2(\frac{l}{W})^3 + 0.529(\frac{l}{W})^2 - 1.529\frac{l}{W} + 1.593C_d = 0 \tag{2.11}$$

$$C_l = \sqrt{2}\frac{l}{W}(1 - \frac{S_t l}{W})(3\frac{S_t l}{W} - 2) \tag{2.12}$$

where l is longitudinal consecutive vortex spacing; h is lateral consecutive vortex spacing; S_t is Strouhal number.

The inversely proportional relationship between C_d and S_t is clear from Eq.2.11. Based on the theory, for given numerical results of C_d and S_t, l can be calculated in terms of W by means of Eq.2.11, and then C_l can be determined by employing Eq.2.12. Therefore, numerical simulation results for l and C_l can be validated by this theoretical method within the supercritical Reynolds number range.

The SFT cross section used for this validation test is determined by the parametric Bézier curve with $b_{up} = b_{low} = 0.5$ m, $y_{up} = 2.5$ m, and $r = 0.1$ m, 0.5 m, 1.0 m, 1.5 m, 2.5 m, 4.5 m. The comparison of numerical and theoretical results are shown in Table 2.2, which shows a close agreement in C_l for bluff bodies (larger r). Flow visualization supported by CFD makes observation of von Kármán vortices feasible, and important phenomena like the vortex street parameters and the occurrence of stagnation can be clearly evaluated. The fluctuation of C_l hence can be correctly predicted by applying the vortex street model.

Both l and C_l follow the same trend as C_d and S_t change, and numerical and theoretical C_l values are fairly close when $r > 0.5$ m. The maximum relative C_l difference of 40.8% and the deviation of l can be explained by the limitations of the theoretical method, which is based on idealizing the vortex wake as two parallel rows of vortices, and neglecting the tunnel surface roughness and viscous contribution to the drag force. Despite its basic limitations, the theoretical method can at least reveal the effect of the SFT cross section profile on vortex street parameters and allow verification of the CFD lift coefficient in a Reynolds number range where experimental data are not available.

2.4. MODEL ANALYSIS AND DISCUSSION

2.4.1. EFFECTS OF y

Fig.2.7 shows $C_{l,rms}$, $S_{t,m}$ and $C_{d,m}$ for the cases $b_{up} = b_{low} = 1$ m, $r = 2.5$ m and y_{up} = 3.5 m, 3 m, 2.5m, 2 m, 1.5 m. The velocity magnitude contours of the three cases are shown in Fig.2.8. As the total height of the SFT cross section is 5 m, decreasing y_{up} means increasing y_{low}; thus y_{up} = 2.5 m produces symmetry in the upper and lower halves of the cross section. When y_{up} =2.5 m, half of the total tunnel height, $C_{l,rms}$ and $C_{d,m}$ take their minimum values, and $S_{t,m}$ takes its maximum value. When $y_{up} > 2.5$ m, both $C_{l,rms}$ and $C_{d,m}$ increase. The mechanism underlying this increase of C_d and C_l due to increased y_{up} can be interpreted as follows: as the flow passes around the leading edge of the tunnel profile, the flow streamline is distorted by the bluff shape, which causes an increase in the velocity gradient. The velocity gradient is related to the profile curvature. The curvature of the upper half increases with increasing y_{up}, and thus generates a more cambered upper half and flatter lower half, hence increasing the velocity magnitude (Fig.2.8) and decreasing the pressure around the cross section upper half based on Bernoulli's principle. The lower half shows the opposite tendency, causing an increasing in the overall C_l of the cross section. The large curvature of the upper half also causes the boundary layer separation point to move upstream, so the width of the wake region increases, which leads to an increase of C_d and C_l, and a decrease of S_t. This behavior agrees with experimental results which compare aerodynamic properties of a flat thin plate with a cambered plate in a water tunnel (Pelletier & Mueller 2000).

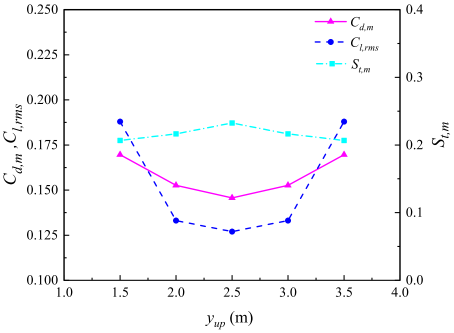

Figure 2.7: Variation of dimensionless lift, drag, and Strouhal number with y_{up}

2.4.2. EFFECT OF r

Fig.2.9 shows $C_{l,rms}$, $S_{t,m}$ and $C_{d,m}$ and Fig.2.10 shows the pressure coefficient along both upper and lower halves of the SFT cross section when lift reaches its peak value for $b_{up} = b_{low} = 0.5$ m, $y_{up} = 2.5$ m, and r = 0.1 m, 0.5 m, 1.0 m, 1.5 m, 2.5 m, 4.5 m.

It can be seen that with increasing r, $C_{l,rms}$ and $C_{d,m}$ decrease remarkably and then increase slightly, with a minimum value around r =2.5m, while $S_{t,m}$ shows an inverse relationship. For r = 0.1 m with a fixed aspect ratio, the sharp leading edge and apex shape are obtained due to the extremely small radius, which causes a complete flow separation from the apex and nadir points (Fig.2.11). At small r, the width of the wake region is large. As a result, lower pressure and a wider wake recirculation region occur near the trailing edge, implying the increase of C_l and C_d. With increasing r, the pressure difference between the upper and lower halves becomes smaller, which can explain the reduction in $C_{l,rms}$ until reaching its lower limit around r = 2.5 m (Fig.2.10(a)). Lift can be generated

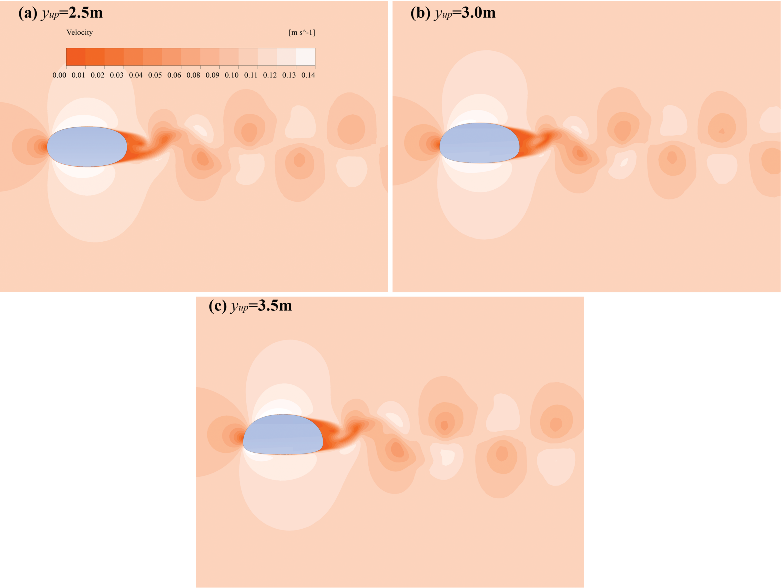

Figure 2.8: Velocity magnitude contours for various y_{up}

by pressure difference between the upper and lower halves, and also the flow separation of the vortex shedding effect due to viscosity. For a symmetrical shape, the RMS lift is determined mainly by vortex shedding. The pressure difference between the upper and lower surfaces of the tunnel results in a minimum RMS lift around $r = 2.5$ m. Hence, a slowly tapering tail with streamlined shape should be considered in the actual design. Furthermore, from Fig.2.10(a), the boundary layer and pressure gradient can be basically categorized into 3 regions: a favorable pressure gradient (FPG), a zero-pressure gradient (ZPG) and an adverse pressure gradient (APG), separated by two inflexion points near the leading and trailing edges due to the free stream flows along the side, separates from the leeward part, and induces comparatively large curvature near the windward and leeward inflexion locations.

For $r \leq 0.5$ m, it is obvious from Fig.2.10(b) that C_p shows a positive correlation with r near the leading edge, with an inverse distribution near the bottom, and the pressures at the leading edge and bottom part of the lower half vary only slightly; thus C_d shows little variation (Fig.2.9). For $r \geq 2.5$ m, the flow velocity increases as it passes around the leading edge of the tunnel cross section. The flow accelerates remarkably due to the large leading-edge stagnation region and the sharp change of flow direction, which causes a large pressure. Additionally, a bluffer tail with a flatter lower half shape develops causes a wider wake region near the trailing edge; both of these mechanisms cause the drag and RMS lift forces to increase.

2.4.3. EFFECT OF b

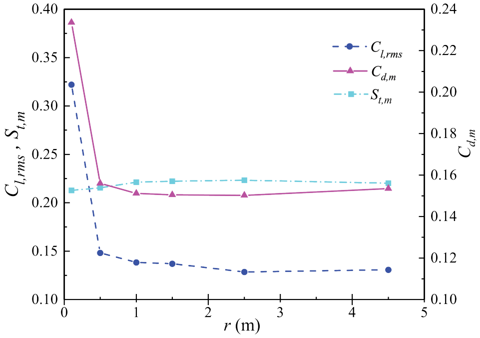

Figure 2.9: Variation of dimensionless lift, drag, and Strouhal number with r

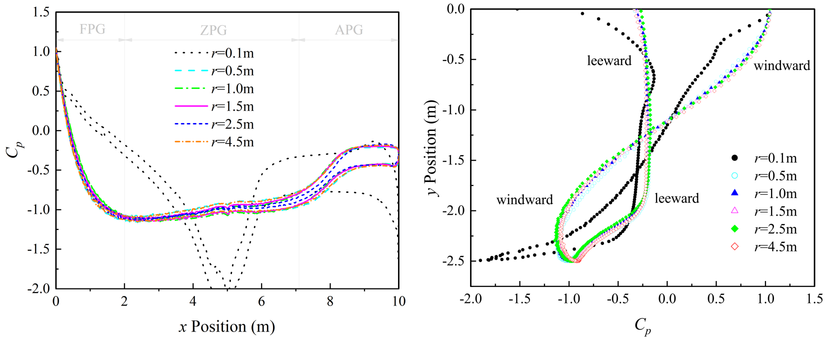

(a) C_p of the cross-section upper and lower halves along x dir. **(b) C_p of the cross-section lower half along y dir.**

Figure 2.10: Pressure distribution along cross section for various r. FPG: favorable pressure gradient; ZPG: zero-pressure gradient; APG: adverse pressure gradient

DIFFERENT b FOR THE UPPER AND LOWER HALVES

Fig.2.12 shows $C_{l,rms}$, $S_{t,m}$ and $C_{d,m}$ for the cases b_{up} = 1.2 m, r = 4.5 m, y_{up} =2.5 m and b_{low} = 0.1 m, 0.6 m, 1.2 m, 1.8 m, 2.4 m. Fig.2.13 shows C_p of the upper and lower halves of the cross section as measured in the counterclockwise direction, when the shear stress vanishes and flow separation occurs on the lower half, and lift reaches its peak value.

It can be noted from Fig.2.13(a), the absolute value of the negative pressure valley at the frontal part is larger than that at the leeward part. The FPG decreases (more negative) with increasing b_{low}. For b_{low} = 0.1 m, the first local minimum is approximately located at x = 2 m, and moves upstream with increasing b_{low} due to a blunter upstream corner on the lower half (Fig.2.14). Similarly, the second local minimum is approximately at x = 7 m, and moves downstream with increasing b_{low}. A plateau exists between these points. It is noted that the average pressure increases with increasing b_{low} due to the flatter profile of the lower half. The thickness of the boundary layer increases quickly and flow separation occurs in the APG region. At the end of the APG region, another plateau represents the leeward wake recirculation region, and the inflection point indicates flow

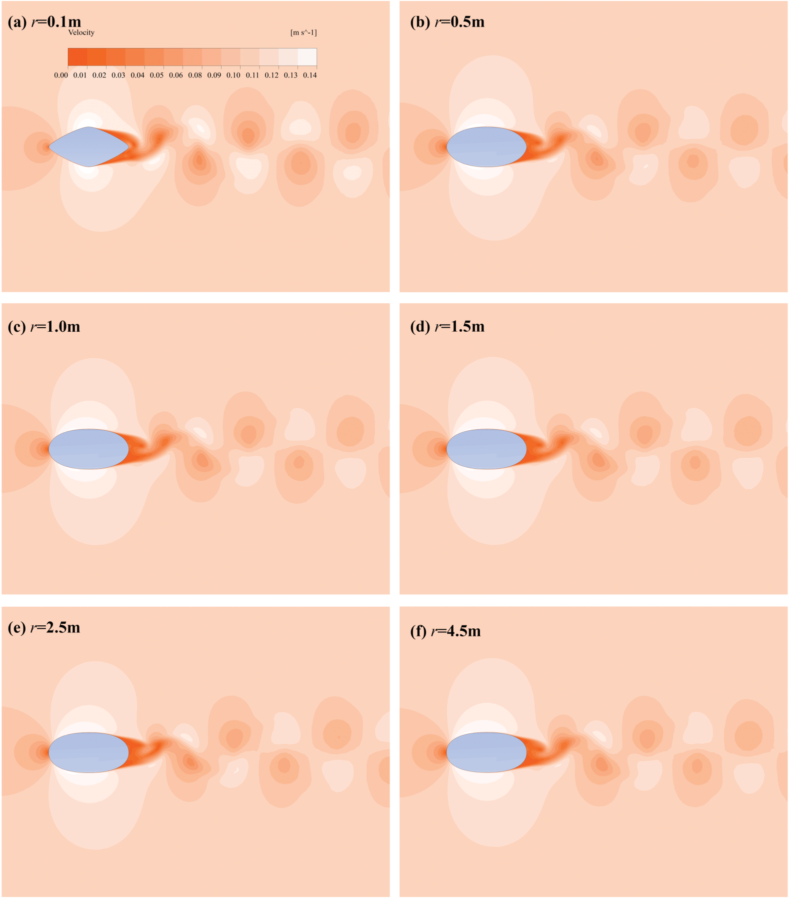

Figure 2.11: Velocity magnitude contours for various r

separation. The lift force induced on a bluff body is mainly due to the pressure difference between its upper and lower halves, and the effect of vortex shedding. It can be deduced from Fig.2.13 (a), comparing the pressure difference between upper and lower halves, that the minimal difference occurs when b values on both halves are the same. It can be concluded that a shape with the same b value shows the minimum pressure difference between the upper and lower halves. That is, it has the minimum C_l.

As for the drag force, it can be observed from Fig.2.13 (b) that with different b_{low}, pressure coefficients of the leeward profile at the lower half keep approximately constant, but a difference becomes apparent on the windward half. In terms of the pressure distribution near the leading edge, C_p increases with increasing b_{low}, although the opposite occurs near the bottom. Consequently, the total pressure along the leading edge increases with b_{low}. Since the pressure distribution difference on the lower half of the leading edge between $b_{low} = 0.1$ m and $b_{low} = 0.6$ m is small, variation in C_d is not obvious. For $b_{low} > 1.2$ m, C_d increases rapidly because C_p near the leading edge increases rapidly with increasing b_{low}.

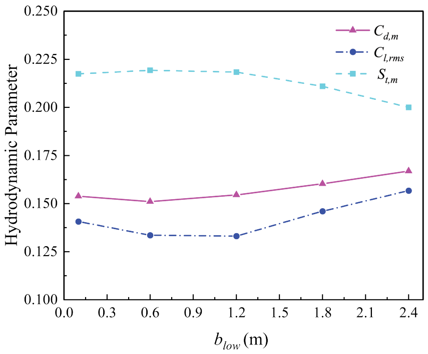

Figure 2.12: Variation of dimensionless lift, drag, and Strouhal number with b_{low}

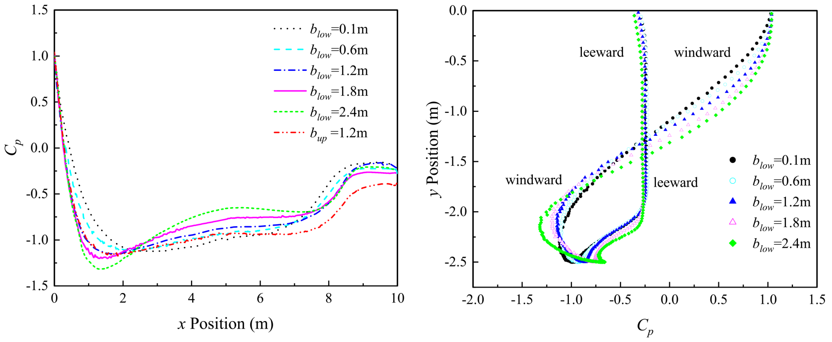

(a) C_p of the cross-section lower and upper halves along x dir. (b) C_p of the cross-section lower half along y dir.

Figure 2.13: Pressure distribution along cross section for various b_{low}

The mechanism of the above phenomenon can be further interpreted as follows. The periodic vortex shedding in the wake region of the bluff body under oncoming uniform cross flow is known as the von Kármán vortex street (Kármán 2013, Abrahamsen Prsic et al. 2016). Hydrodynamic and vortex street parameters show dependence on the cross section shape. The curvature of the upper and lower halves of the SFT cross section affects the interaction of the two separated boundary layers, and, hence the vortex street generation process. For a symmetric shape, the vortex street propagates with a same magnitude of velocity and vorticity on the upper and lower halves, and the two separated shear layers coincide, approach, curve inwards and interact with each other more quickly, forming the von Kármán vortex street with a shorter vortex formation length at the trailing edge and resulting in a more rapid vortex shedding rate, and therefore, a larger S_t, smaller longitudinal vortex spacing l and C_l compared to the asymmetric cross sections.

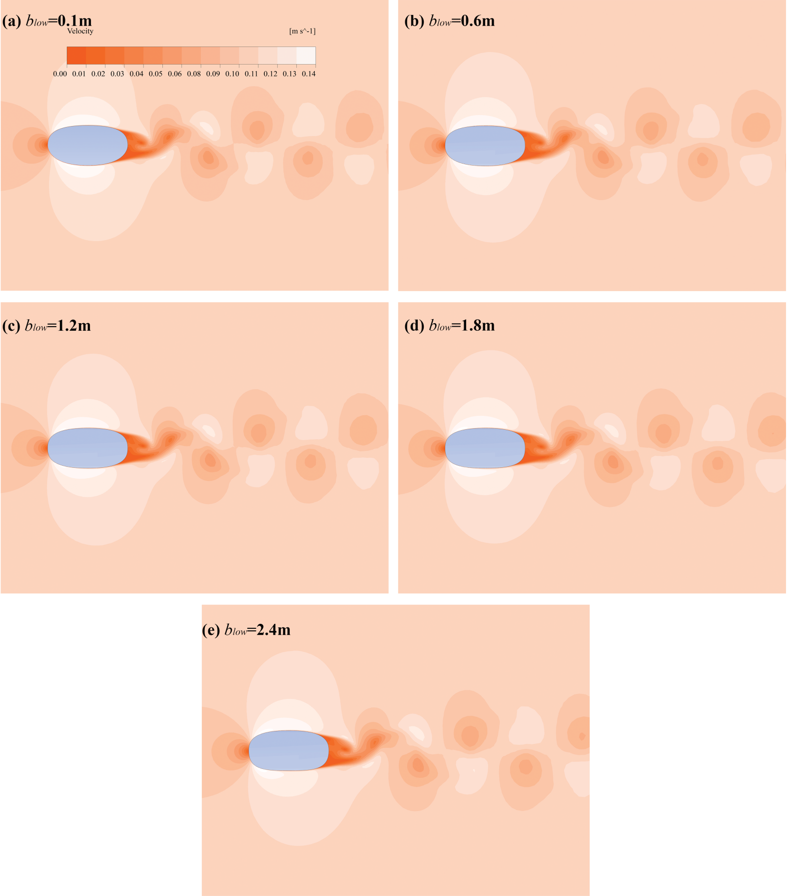

Figure 2.14: Velocity magnitude contours for various b_{low}

SAME b FOR THE UPPER AND LOWER HALVES

As a symmetrical tunnel profile is more favorable for minimizing lift but does not obviously affect drag (section 2.4.3), the drag and lift coefficients for various b on both the upper and lower halves are discussed. Fig.2.15 shows $C_{l,rms}$, $S_{t,m}$ and $C_{d,m}$ for $b_{low} = b_{up} = 0.1$ m, 0.5 m, 1.2 m, 1.8 m, 2.4 m, $r = 4.5$ m, and $y_{up} = 2.5$ m. In order to describe the $C_{l,rms}$ tendency clearly, here C_p curves for only three tunnel profiles are shown. Fig.2.16(a) shows that the pressure difference between upper and lower halves increases with increasing b, thus $C_{l,rms}$ increases. It is clear that the pressure difference between the windward surface and leeward region reflects the magnitude of drag. Fig.2.17 shows the velocity magnitude contours. From Fig.2.16(b), pressure coefficients on the leeward lower part are similarly consistent, but C_p increases gradually with increasing b near the front of the leading edge. This occurs despite the fact that in a localized region near the bottom of the leading edge C_p becomes more negative with increasing b. That is, C_d increases as b increases.

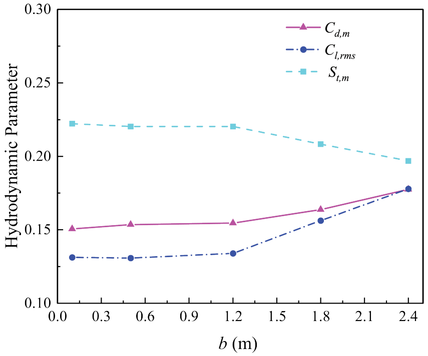

Figure 2.15: Variation of dimensionless lift, drag, and Strouhal number with *b*

It should be noted that increasing *b* or *r* of the parametric Bézier curve doesn't always act to make the body bluffer for a fixed aspect ratio. The combined effect of *b* or *r* affect drag and lift, making optimal profile selection complicated. Nevertheless, from section 2.4.3, $C_{l,rms}$ and $C_{d,m}$ are not always independent. The optimal cross section design should be considered in the arrangement, inclined angle, and stiffness of the mooring system and the buoyancy control of the SFT.

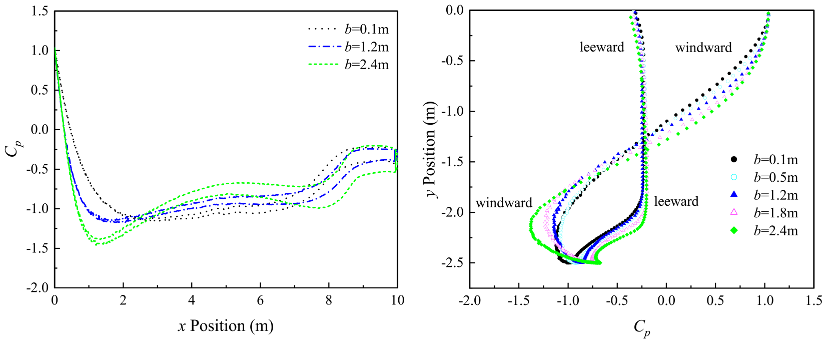

(a) C_p of the cross-section lower and upper halves along *x* dir. (b) C_p of the cross-section lower half along *y* dir.

Figure 2.16: Pressure distribution along cross section for various *b*

2.5. OPTIMIZATION ALGORITHMS

2.5.1. MULTI-OBJECTIVE OPTIMIZATION

A multi-objective problem compromises a vector of decision variables satisfying a number of inequality or equality constraints to give optimal solutions to all objectives simultaneously (Demirkaya et al. 2012). In this study, since it is unrealistic to solve all the possible SFT cross-section shapes with a combination of different variables using the complicated and time-consuming CFD code, and with the problems of the interdependent distributions of $C_{l,rms}$ and $C_{d,m}$, we consider $C_{l,rms}$ and $C_{d,m}$ as two minimization objectives and a function of four Bézier curve parameters varying independently, using an artificial intelligence (AI) optimization algorithm. Concerning the BP parameter constraint conditions in section 2.2.1, the problem can be described as follows:

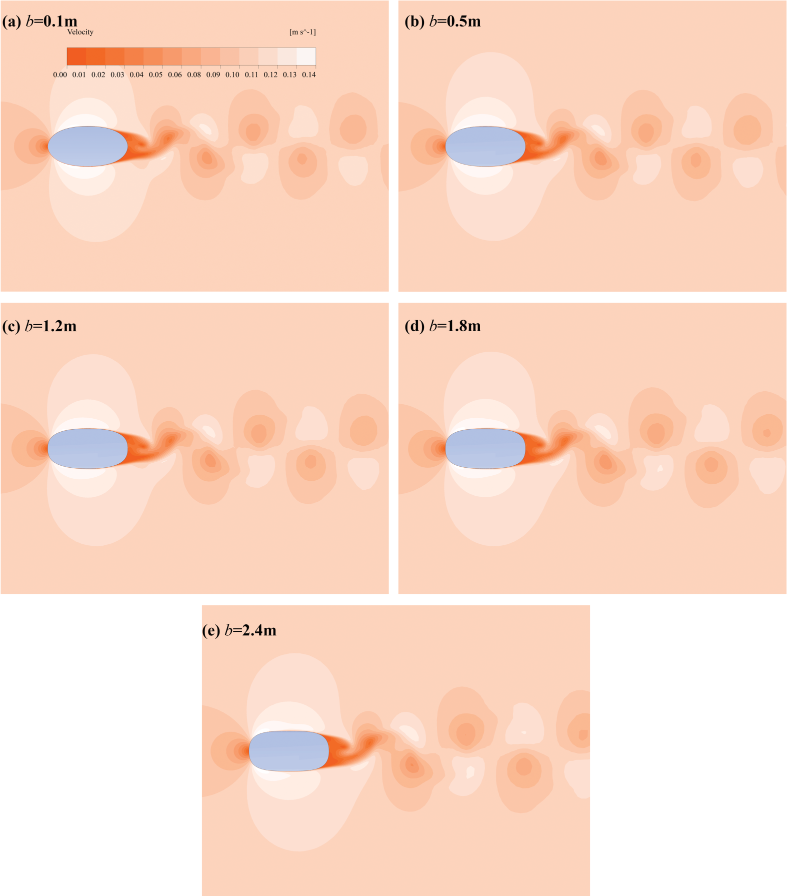

Figure 2.17: Velocity magnitude contours for various b

Optimization parameters: y_{up}, r, b_{up}, b_{low}
Optimization objectives:

$$\begin{cases} \min C_{l,rms}(y_{up}, r, b_{up}, b_{low}) \\ \min C_{d,m}(y_{up}, r, b_{up}, b_{low}) \end{cases} \tag{2.13}$$

Constraint conditions:

$$\begin{cases} 0 \leq y_{up} \leq 5 \\ 0 < r \leq 5 \\ 0 < b_{up} < \min(y_{up}, \sqrt{10r/3}) \\ 0 < b_{low} < \min(5 - y_{up}, \sqrt{10r/3}) \end{cases} \tag{2.14}$$

2.5.2. HYBRID NEURAL NETWORKS AND GENETIC ALGORITHM

A NN (Ahn et al. 2019, Li, Choung & Noh 2018) with multiple layers is applied to predict the hydrodynamic properties under various possible BP curve parameters. NN's have superior capacity in forecasting the relationships between input and output variables for data-driven prediction. The backpropagation (BP) learning algorithm is the most popular NN training method and is well suited for unseen features such as learning from previous experience samples (Papadrakakis et al. 1998). Hence, it is unnecessary to simulate all the possible tunnel cross-section shapes a priori, with the ability of NN's to recognize arbitrary profile features.

In this study, a GA (da Silva et al. 2013) is used to optimize the initial weights and thresholds of the BP algorithm, which is a weight optimization architecture commonly called "GA-BP". With the ability to produce robust and effective results for noisy and discontinuous data, GA can search the entire solution space to find the global optimum via selection, crossover and mutation processes, to avert convergence problems from getting stuck in local minima (Yan et al. 2019).

In this study, a three-layer BP NN structure is applied as a prediction and optimization model. Four neurons are contained in the input layer, denoting y_{up} , r, b_{up}, and b_{low} to determine the tunnel cross-section shape. All these parameters of every case are randomly generated within the constraints and normalized into the range of (-1,1). The hidden layer consisted of 10 neurons with the "tansig" transfer function (Vogl et al. 1988). Two neurons with linear transfer functions are applied as the output layer, denoting $C_{l,rms}$ and $C_{d,m}$. Therefore, a "4-10-2" BP-GA structure is employed in this study. The detailed parameters of the hybrid BP-GA structure are shown in Table 2.3.

Table 2.3: Input parameters used in the hybrid BP-GA model

Input parameters	The BP-GA Model
Training times	500
Total squared error	0.0001
Learning rate	0.01
Population size	50
Max. generations	100
Crossover probability	0.9
Uniform mutation probability	0.01

The BP algorithm optimizes weights and thresholds to minimize prediction error to the training data set, while the GA prevents the BP solution from getting stuck in local minima of the error. To verify the effectiveness of the BP-GA optimization process, further analysis and discussion are conducted in section 2.5.3.

2.5.3. RESULTS ANALYSIS AND VERIFICATION

Fig.2.18 illustrates the optimal cross-section selection process by using hybrid BP-GA including three main steps: establish the initial population model including training and testing data sets; determine the BP training set by applying the GA optimization; and conduct the BP prediction process and verify with CFD analysis.

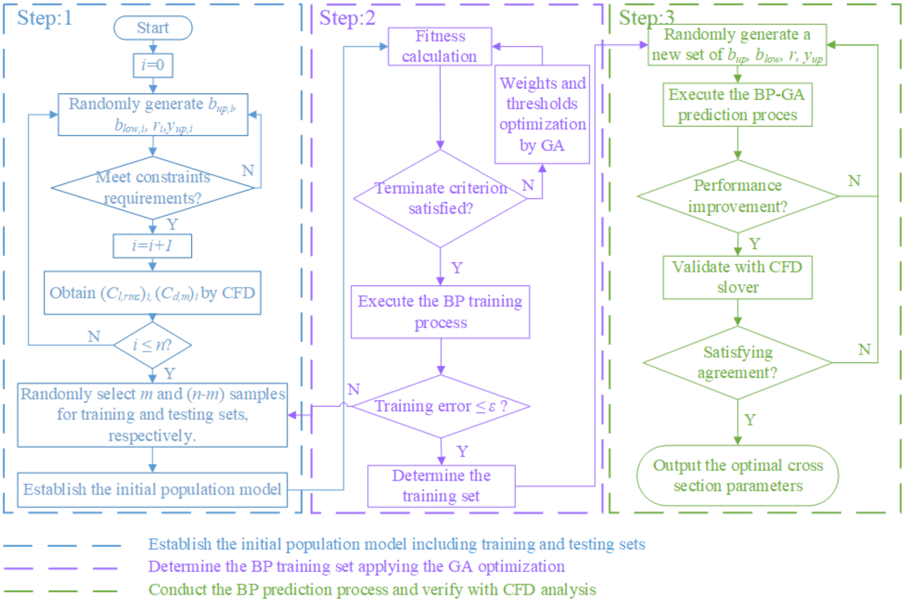

Figure 2.18: Flow chart of the hybrid BP-GA optimization process

Step 1: Two procedures are included in this step: first, randomly generate $n = 60$ groups of Bézier curve parameters within the constraints and obtain $C_{l,rms}$ and $C_{d,m}$ as objective functions by conducting reliable CFD simulations. Note that the randomly generated parameters should be uniformly and reasonably distributed within the constraints to increase the accuracy and reliability of further optimization; second, randomly select $m = 50$ groups of samples as a training set and the remaining 10 samples as a testing set to execute the BP training process.

Step 2: The GA implemented by a roulette-wheel algorithm is applied to the thresholds and weights optimization of the BP NN structure. The target of this optimization is to maximize the fitness value to achieve ideal prediction results. The mathematical relationship between the input parameters comprised of 4 Bézier curve variables and output objectives including $C_{l,rms}$ and $C_{d,m}$ is established after the training process of the hybrid BP-GA. After comparing the prediction results with the testing set, the Average Root Mean Square Error (ARMSE) which is a measure of scatter or lack of precision, and Square Pearson Coefficient R^2 of each case are calculated as two discriminant criteria. Here, the ARMSE and R^2 are expressed by Eq. 2.15 and 2.16

$$ARMSE = \sqrt{\frac{1}{10}\sum_{i=1}^{10}(y_p - y_c)_i^2} \tag{2.15}$$

$$R^2 = \frac{\sum_{i=1}^{10}\left[(y_{p,i} - y_{p,m}) \times (y_{c,i} - y_{c,m})\right]^2}{\sum_{i=1}^{10}\left[(y_{p,i} - y_{p,m})\right]^2 \times \sum_{i=1}^{10}\left[(y_{c,i} - y_{c,m})\right]^2} \tag{2.16}$$

where y_p and y_c represent for the predicted and calculated values of $C_{l,rms}$ and $C_{d,m}$, respectively. The subscript m represents the mean value.

To ensure the representativeness of the training set, the ARMSE is restricted to a maximum training error ϵ, here taken as 0.01, and an $R^2 > 0.8$, which signifies a satisfactory performance (Coulibaly & Baldwin 2005). A statistical comparison of the mean drag and RMS lift coefficients between the BP-GA training results (the predicted values) and the testing set (the CFD results) is performed in Fig.2.19. It clearly shows the max. ARMSE = 0.009 with $R^2 = 0.861$ for $C_{d,m}$, and 0.010 with $R^2 = 0.822$ for $C_{l,rms}$, suggesting a qualitatively good performance of the hybrid BP-GA training process.

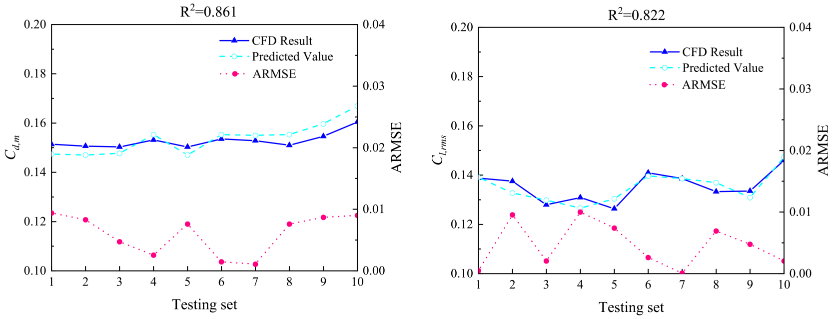

(a) Training results of $C_{d,m}$ (b) Training results of $C_{l,rms}$

Figure 2.19: Comparison of the BP-GA training results with 10 testing samples

Step 3: After determining the training set to use in the optimal cross-section prediction, $C_{l,rms}$ and $C_{d,m}$ of randomly cases comprised of Bézier curve parameters within constrains are predicted with the utilization of the trained hybrid BP-GA NN. The prediction process is terminated by searching for $C_{l,rms}$ and $C_{d,m}$ values smaller than the minimum sample results in the training and testing sets. The output optimal SFT cross-section Bezier parameters are then validated with CFD.

Fig.2.20 shows minimum values of $C_{l,rms}$ and $C_{d,m}$ among the 60 original samples, the predicted values for the optimized cross section as output the by BP-GA, and the actual values output by CFD of the optimal cross section. The Bézier curve parameters of the optimal SFT cross section are: b_{up}=b_{low} = 1 m; r= 3 m; y_{up} = y_{low} = 2.5 m. The forecast has an error of 1.7% compared with the CFD validation result, which illustrates the feasibility and reliability of the hybrid BP-GA prediction. The optimized SFT cross section $C_{d,m}$ is 0.9% lower, and $C_{l,rms}$ is 6.3% lower, than the mean drag and the RMS lift coefficients of the original 60 random samples. In this case, the minimum mean drag value of the sample is small, so the reduction of the optimal value is not obvious. However, it also shows that the sample is representative which the approximate optimal solution has already been covered. Overall, an optimized profile with better hydrodynamic performance than the original 60 samples is achieved by the hybrid BP-GA optimization.

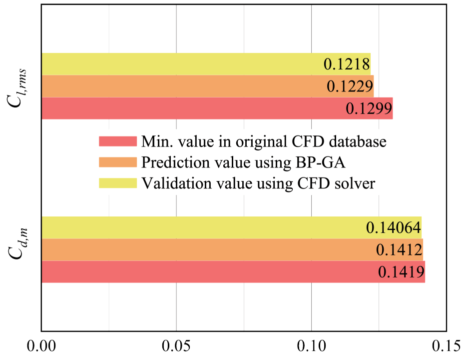

Figure 2.20: Hydrodynamic performance comparison after optimization

2.6. CROSS-SECTIONAL ASPECT RATIO ANALYSIS UNDER TIDAL FLOWS

This section aims to predict the in-line force accurately for the SFT and to determine a well-performing SFT cross-section geometry. In-line force on the SFT cross section (horizontal load comprises the drag and inertial force) has a major impact on the reliability of the SFT, and is mainly determined by cross-sectional geometry and hydrodynamic loading. However, hydrodynamic performance analysis of the SFT under tidal flow conditions and detailed understanding of the physics of flows around the SFT surface, are still absent. Therefore, in this section, a more realistic hydrodynamic condition of bidirectional and transient tidal flow is considered for the effects of cross-sectional aspect ratio analysis, where Reynolds number varies greatly, and may induce transition processes in the boundary layer.

Langtry (Langtry & Menter 2009) has been developed transition SST model ($\gamma - \widetilde{Re_{\theta t}}$ model) for transition turbulent prediction, and flat-plate numerical simulations show good agreement with experimental data ranging from bypass transition to natural transition and separation-induced transition. Thus, transition SST model is adopted, shown in Eq.2.17.

$$\begin{cases} \dfrac{\partial(\rho\gamma)}{\partial t} + \dfrac{\partial(\rho\gamma u_j)}{\partial x_j} = \dfrac{\partial[(\mu+\frac{\mu_t}{\sigma_\gamma})\frac{\partial\gamma}{\partial x_j}]}{\partial x_j} + P_{\gamma 1} - E_{\gamma 1} + P_{\gamma 2} - E_{\gamma 2} \\ \dfrac{\partial(\rho\widetilde{R_{e\theta t}})}{\partial t} + \dfrac{\partial(\rho\widetilde{R_{e\theta t}}u_j)}{\partial x_j} = \dfrac{\partial[\sigma_{\theta t}(\mu+\mu_t)\frac{\partial\widetilde{R_{e\theta t}}}{\partial x_j}]}{\partial x_j} + P_{\theta t} \end{cases} \tag{2.17}$$

where $\sigma_\gamma = 1.0$, $\sigma_{\theta t} = 2.0$. $P_{\gamma 1}, E_{\gamma 1}$ are transition sources, $P_{\gamma 2}, E_{\gamma 2}$ are destruction or relaminarization sources; $P_{\theta t}$ is a source term; $\widetilde{R_{e\theta t}}$ is the transition momentum thickness Reynolds number; U is upstream flow velocity; γ is intermittency; μ is viscosity; μ_t is eddy viscosity; and ρ is fluid density. Detailed formulations of the transition SST model are given in reference (Coder & Maughmer 2013).

Zhu et al. (Zhu et al. 2015) carried out a 15-day coastal acoustic tomography experiment to quantity the tidal current in the Qiongzhou Strait over a fortnightly spring-neap tidal cycle. A representative time series of the section-averaged velocity (station pairs

C3–C4 in (Zhu et al. 2015) is adopted as the CFD inlet boundary condition (Fig.2.21). Due to the slow variation of the tidal current speed, in order to reduce computational cost, we take a 2-hour window around peak velocity (the green circle) from an entire 24h transient tidal cycle as the inlet velocity boundary for all the transient simulations with the freestream turbulence intensity T_{uinlet} and turbulence length scale as $0.006U^{-1}$ and 40 m, respectively.

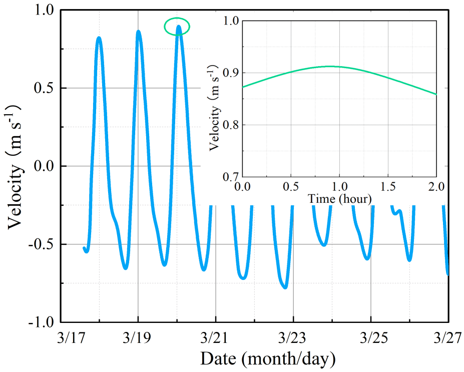

Figure 2.21: Measured tidal velocities in the Qiongzhou Strait

Due to the sharp trailing-edge of normal airfoils, the Kutta condition (Crighton 1985) can be met, which effectively precludes the possibility of vortex shedding, and hence, reduces the in-line force. Therefore, the BP curve composed by the trailing-edge profile is also applied to describe the SFT cross-section. In order to compare the impacts of different types of Bezier curves and aspect ratio (AR) (defined by y_t/x_t) on the hydrodynamic response of the SFT, the BP curve composed by the leading-edge profile and trailing-edge profile are adopted to define the SFT cross-section geometry. The parametric Bézier curve of each quadrant and control points are shown in Fig.2.2.

The four control points that determine the shape of one quadrant of the SFT cross-section using trailing-edge is given by Eq. 2.18.

$$\begin{cases} x_0 = 0, y_0 = y_t \\ x_1 = -x_t + 3b^2/2r, y_1 = y_t \\ x_2 = -x_t + b\cot\beta, y_2 = b \\ x_3 = -x_t 0, y_3 = 0 \end{cases} \tag{2.18}$$

In the sensitivity analysis of cross-sectional AR, $b = 1.5$ m, $r = 0.5$ m, and $\beta = 15°$ are selected and y_t of 3 m, 4 m, and 5 m are applied, respectively, for trailing-edge and leading-edge BP curves. The SFT cross-sections expressed by the leading-edge and trailing-edge BP curves with the same clearance are shown in Fig.2.22(a).

However, an SFT cross-section of the same clearance defined by different BP curves causes inconsistency in AR. In order to determine the best BP curve type in improving the hydrodynamic performance, but eliminate the impacts of AR, another subset of leading-edge and trailing-edge BP curves under the equal AR is chosen for comparison (Fig.2.22(b)).

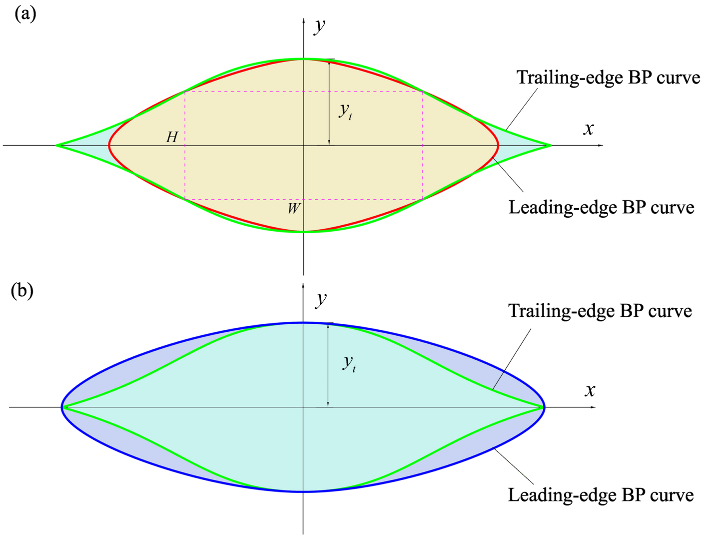

Figure 2.22: Leading-edge and Trailing-edge BP curve geometry. (a) equal clearance; (b) equal AR

2.6.1. CROSS-SECTIONAL GEOMETRY PERFORMANCE COMPARISON

In order to determine the best cross section shape for the hydrodynamic performance of the SFT, $C_{f,m}$ distributions (skin-friction coefficient C_f is defined by $C_f = \tau_\omega/(0.5 \times \rho \times U^2)$, where τ_ω is local wall shear stress) over the SFT cross-section expressed by leading-edge and trailing-edge BP curves under constant AR with varying y_t are illustrated in Fig.2.23.

It can be seen that the peak $C_{f,m}$ increases with increasing y_t for both BP curve formats. $C_{f,m}$ close to zero corresponds to flow separation and the subsequent wake extension. A narrow flow separation at the rear can be observed at y_t = 3 m using the leading-edge BP curve. However, no flow separation occurs with the trailing-edge BP curve, where the Kutta condition can be met (Crighton 1985). The flow separation point moves noticeably forward with increasing y_t. Compared with the leading-edge BP curve, as y_t increases, a further forward separation point and larger wake region can be seen from the trailing-edge BP curve. This can be seen in Fig.2.24, which shows time-averaged velocity contours of the two curve formats at y_t = 4 m. As y_t increases, the apex of the trailing-edge BP curve is sharper and less streamlined. The bluffer shape results in the streamflow passing the apex, detaching from the surface, and forming a large wake of recirculating flow, which also increases the in-line force.

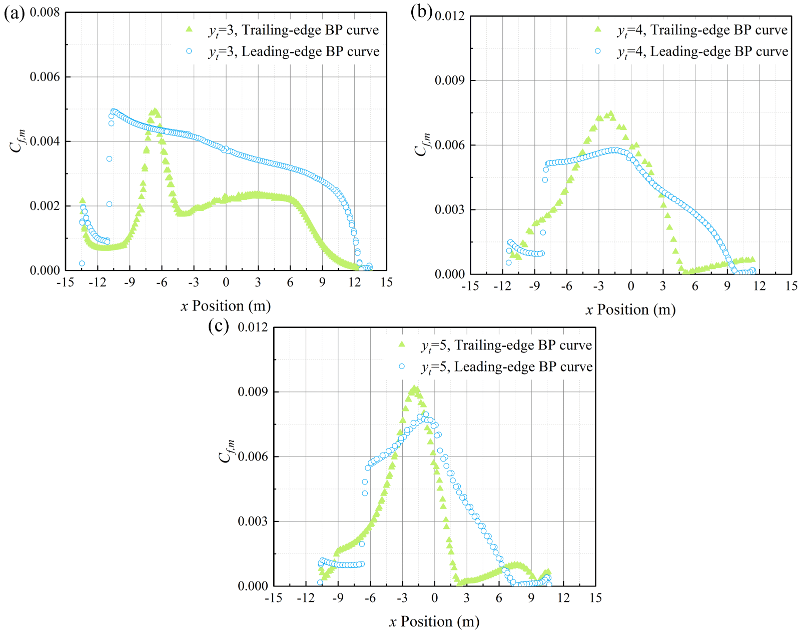

Figure 2.23: Time-averaged skin-friction coefficient distribution. (a) $y_t = 3$ m; (b) $y_t = 4$ m; (c) $y_t = 5$ m

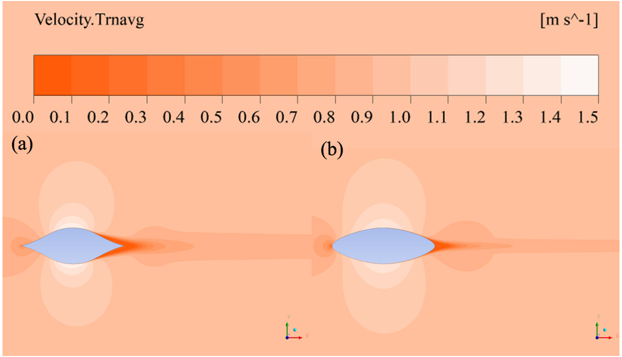

Figure 2.24: Time-averaged velocity contours at $y_t = 4$ m. (a) Trailing-edge BP curve; (b) Leading-edge BP curve

2.6.2. CROSS-SECTIONAL ASPECT RATIO PERFORMANCE COMPARISON

Figure 2.25 shows the mean drag coefficient $C_{d,m}$ and perimeter of the different SFT cross-sectional geometries and aspect ratios. It can be seen clearly that as AR increases, $C_{d,m}$ on the trailing-edge BP curve increases rapidly compared with the leading-edge one (equal AR), indicating the leading-edge format has a better hydrodynamic performance. However, continuously increasing AR makes the geometry bluffer, and $C_{d,m}$ increases dramatically when AR > 0.47. In this case, an AR not exceeding 0.47 using a leading-edge BP curve is preferred. In addition to hydrodynamic performance, the SFT cross-section design is affected by clearance requirements, structural safety, and construction costs. It can be found from Fig.2.25(a) that $C_{d,m}$ on the two formats of leading-edge BP curves (equal AR and equal clearance) are similar in general. However, the SFT cross-sectional perimeter can be effectively shortened with a leading-edge BP curve of equal clearance (Fig.2.25(b)). Therefore, the SFT cross-section with AR = 0.47 using a leading-edge BP curve of equal clearance balances hydrodynamic forcing and material costs well.

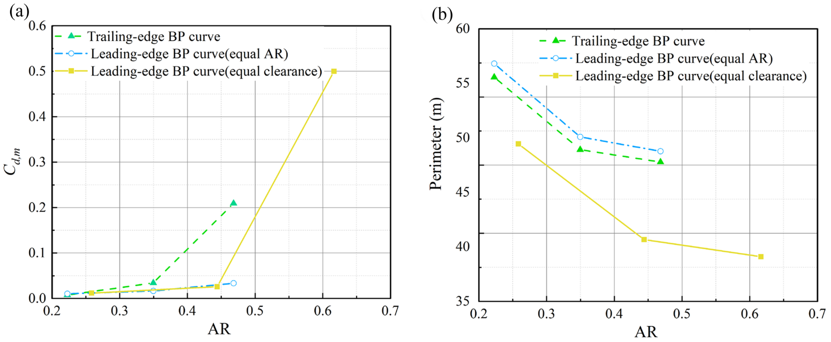

Figure 2.25: Drag coefficient and perimeter of the SFT cross-section. (a) Mean drag coefficient comparison; (b) Perimeter comparison

2.7. CONCLUSIONS

To overcome a lack of research on hydrodynamic performance of SFT cross sections, a parametric Bézier curve is applied to SFT cross section geometry design, and a sensitivity analysis to the Bézier curve parameters is carried out. The RMS lift and mean drag coefficients are considered as objective functions and are optimized by a hybrid BP-GA structure. The main conclusions are briefly summarized as follows:

- The Bézier curve parameters analysis shows y_{up} with a value of half of the total tunnel height achieves the minimum RMS C_l and mean C_d. To reduce the RMS lift force, a symmetrical shape with same b on both upper and lower surfaces should be used. The pressure difference between the leading edge and trailing edge reflects the magnitude of drag. For an SFT cross section with a fixed and relatively thick aspect ratio, a better hydrodynamic performance can't be achieved by continuously minimizing the leading edge radius, because a sharp leading edge and apex shape causes flow detachment.

- The numerical CFD simulation are verified with a theoretical method to determine the drag and lift by employing the Kármán vortex street parameters, despite limitations due to basic assumptions.

- A neural network with a backpropagation learning algorithm benefits from combination with a GA. This reduces the need for time-consuming CFD analyses, and increases the accuracy, reliability and goodness of prediction of the SFT cross section design. Therefore, hybrid BP-GA is an effective tool to optimize the complex interdependency of Bézier curve parameters.

- By increasing the aspect ratio, the SFT cross-section described by the leading-edge BP curve shows better hydrodynamic performance than the trailing-edge BP curve. Additionally, the SFT cross-section with AR = 0.47 using the leading-edge BP curve under the given clearance appears the best option with a balanced consideration of hydrodynamic performances and construction cost.

In spite of these achievements of the Bézier curve parameter analysis and applicability of the hybrid BP-GA method, some restrictions and future work still should be noted in this study:

- A fixed aspect ratio for the SFT cross section is used. It is worth noting that the drag and lift of each Bézier curve parameter combination will be different for different aspect ratios. However, the basic methodology of CFD simulation combined with the hybrid BP-GA optimization process is still applicable.
- The future work should consist of a larger training set to optimize the algorithm variables and increase forecasting robustness and accuracy.

REFERENCES

AASHTO (2018), *A Policy on Geometric Design of Highways and Streets*.

Abrahamsen Prsic, M., Ong, M. C., Pettersen, B. & Myrhaug, D. (2016), ‘Large Eddy Simulations of flow around a circular cylinder close to a flat seabed’, *Marine Structures* .

Ahn, Y., Kim, Y. & Kim, S. Y. (2019), ‘Database of model-scale sloshing experiment for LNG tank and application of artificial neural network for sloshing load prediction’, *Marine Structures* .

Ahrens, D. (1997), ‘Submerged floating tunnels - A concept whose time has arrived’, *Tunnelling and Underground Space Technology* .

ANSYS, F. (2019), ‘ANSYS fluent theory guide 19.1’, *ANSYS, Canonsburg, PA* .

Basumatary, M., Biswas, A. & Misra, R. D. (2018), ‘CFD analysis of an innovative combined lift and drag (CLD) based modified Savonius water turbine’, *Energy Conversion and Management* .

Bézier, P. (1974), MATHEMATICAL AND PRACTICAL POSSIBILITIES OF UNISURF, *in* ‘Computer Aided Geometric Design’.

Catalano, P., Wang, M., Iaccarino, G. & Moin, P. (2003), ‘Numerical simulation of the flow around a circular cylinder at high Reynolds numbers’, *International Journal of Heat and Fluid Flow* .

Coder, J. G. & Maughmer, M. D. (2013), A CFD-compatible transition model using an amplification factor transport equation, *in* '51st AIAA Aerospace Sciences Meeting including the New Horizons Forum and Aerospace Exposition 2013'.

Coulibaly, P. & Baldwin, C. K. (2005), 'Nonstationary hydrological time series forecasting using nonlinear dynamic methods', *Journal of Hydrology* .

Crighton, D. G. (1985), 'The Kutta Condition in Unsteady Flow', *Annual Review of Fluid Mechanics* .

da Silva, R. F., Teófilo, F. A. F., Parente, E., de Melo, A. M. C. & de Holanda, Á. S. (2013), 'Optimization of composite catenary risers', *Marine Structures* .

Demirkaya, G., Besarati, S., Vasquez Padilla, R., Ramos Archibold, A., Goswami, D. Y., Rahman, M. M. & Stefanakos, E. L. (2012), 'Multi-Objective Optimization of a Combined Power and Cooling Cycle for Low-Grade and Midgrade Heat Sources', *Journal of Energy Resources Technology* .

Derksen, R. W. & Rogalsky, T. (2010), 'Bezier-PARSEC: An optimized aerofoil parameterization for design', *Advances in Engineering Software* .

Gang, L., Xiao-jun, Z. & Jian-xun, C. (2018), 'The Dynamic Response of an Experimental Floating Tunnel with Different Cross Sections under Explosive Impact', *Journal of Coastal Research* .

Garg, N., Pearce, B. W., Brandner, P. A., Phillips, A. W., Martins, J. R. & Young, Y. L. (2019), 'Experimental investigation of a hydrofoil designed via hydrostructural optimization', *Journal of Fluids and Structures* .

Hajabdollahi, F., Rafsanjani, H. H., Hajabdollahi, Z. & Hamidi, Y. (2012), 'Multi-objective optimization of pin fin to determine the optimal fin geometry using genetic algorithm', *Applied Mathematical Modelling* .

James, W. D., Paris, S. W. & Malcolm, G. N. (1980), 'Study of viscous crossflow effects on circular cylinders at high reynolds numbers', *AIAA Journal* .

Jung, S., Choi, W., Martins-Filho, L. S. & Madeira, F. (2016), 'An implementation of self-organizing maps for airfoil design exploration via multi-objective optimization technique', *Journal of Aerospace Technology and Management* .

Kármán, T. V. (2013), 'On the mechanism of the drag a moving body experiences in a fluid'.

Kuzmin, D., Mierka, O. & Turek, S. (2007), 'On the implementation of the fr-fturbulence model in incompressible flow solvers based on a finite element discretisation', *International Journal of Computing Science and Mathematics* .

Langtry, R. B. & Menter, F. R. (2009), 'Correlation-based transition modeling for unstructured parallelized computational fluid dynamics codes', *AIAA Journal* .

Larssen, R. M. & Jakobsen, S. E. (2010), Submerged floating tunnels for crossing of wide and deep fjords, *in* 'Procedia Engineering'.

Lee, J. J., Jung, U. J. & Park, G. J. (2013), 'Shape optimization of the workpiece in the forging process using equivalent static loads', *Finite Elements in Analysis and Design* .

Li, C. B., Choung, J. & Noh, M. H. (2018), 'Wide-banded fatigue damage evaluation of Catenary mooring lines using various Artificial Neural Networks models', *Marine Structures* .

Li, K. & Jiang, X. (2016), Research on Section Form of Submerged Floating Tunnels Considering Structural Internal Force Optimization under Fluid Action, *in* 'Procedia Engineering'.

Li, Q., Jiang, S. & Chen, X. (2018), 'Experiment on Pressure Characteristics of Submerged Floating Tunnel with Different Section Types under Wave Condition', *Polish Maritime Research* .

Lin, H., Xiang, Y. & Yang, Y. (2019), 'Vehicle-tunnel coupled vibration analysis of submerged floating tunnel due to tether parametric excitation', *Marine Structures* .

Lin, Y. H., Lu, P. Y. & Lin, C. W. (2019), 'Numerical simulation of maximum wave loads and run-up heights on offshore wind turbine foundations influenced by the instability of bichromatic wave groups', *Marine Structures* .

Muhammad, N., Ullah, Z. & Choi, D. H. (2017), 'Performance evaluation of submerged floating tunnel subjected to hydrodynamic and seismic excitations', *Applied Sciences (Switzerland)* .

Murray, Y. D. et al. (2007), Users manual for ls-dyna concrete material model 159, Technical report, United States. Federal Highway Administration. Office of Research . . . .

Nikolaev, N. V. (2019), 'Optimization of Airfoils along High-Aspect-Ratio Wing of Long-Endurance Aircraft in Trimmed Flight', *Journal of Aerospace Engineering* .

Ong, M. C., Utnes, T., Holmedal, L. E., Myrhaug, D. & Pettersen, B. (2009), 'Numerical simulation of flow around a smooth circular cylinder at very high Reynolds numbers', *Marine Structures* .

Papadrakakis, M., Lagaros, N. D. & Tsompanakis, Y. (1998), 'Structural optimization using evolution strategies and neural networks', *Computer Methods in Applied Mechanics and Engineering* .

Pelletier, A. & Mueller, T. J. (2000), 'Low Reynolds number aerodynamics of low-aspect-ratio, thin/flat/cambered-plate wings', *Journal of Aircraft* .

Rogalsky, T., Kocabiyik, S. & Derksen, R. W. (2000), 'Differential evolution in aerodynamic optimization', *Canadian Aeronautics and Space Journal* .

Rogalsky, T. P. (2004), 'Acceleration of differential evolution for aerodynamic design'.

Sallet, D. W. (1973), 'LIFT FORCE DUE TO VON KARMAN'S VORTEX WAKE.', *J Hydronaut* .

Tveit, P. (2000), 'Ideas on downward arched and other underwater concrete tunnels', *Tunnelling and Underground Space Technology* .

Van Doormaal, J. P. & Raithby, G. D. (1984), 'Enhancements of the simple method for predicting incompressible fluid flows', *Numerical Heat Transfer* .

van Marrewijk, C. (2020), 'Form finding for a submerged floating tunnel: The clever cross-section for coastal crossings'.

Vogl, T. P., Mangis, J. K., Rigler, A. K., Zink, W. T. & Alkon, D. L. (1988), 'Accelerating the convergence of the back-propagation method', *Biological Cybernetics* .

Wang, A., Zhao, G. & Hou, F. (2019), 'Constructing Bézier curves with monotone curvature', *Journal of Computational and Applied Mathematics* .

Wang, X. & Lu, Y. (2018), 'Optimization of the cross section area on the meridian surface of the 1400-MW canned nuclear coolant pump based on a new medial axial transform design method', *Annals of Nuclear Energy* .

Yan, C., Li, M., Liu, W. & Qi, M. (2019), 'Improved adaptive genetic algorithm for the vehicle Insurance Fraud Identification Model based on a BP Neural Network', *Theoretical Computer Science* .

Zhang, J., Wu, W. & Hu, J. (2016), 'A numerical study of the effects of the longitudinal baffle on nickel ore slurry sloshing in a prismatic cargo hold', *Marine Structures* .

Zhu, X. H., Zhu, Z. N., Guo, X., Ma, Y. L., Fan, X., Dong, M. & Zhang, C. (2015), 'Measurement of tidal and residual currents and volume transport through the Qiongzhou Strait using coastal acoustic tomography', *Continental Shelf Research* **108**, 65–75.
URL: *http://dx.doi.org/10.1016/j.csr.2015.08.016*

Zou, P., Bricker, J. D. & Uijttewaal, W. (2021), 'Submerged floating tunnel cross-section analysis using a transition turbulence model', *Journal of Hydraulic Research* pp. 1–13.

Zou, P., Bricker, J. & Uijttewaal, W. (2020), 'Optimization of submerged floating tunnel cross section based on parametric Bézier curves and hybrid backpropagation - genetic algorithm', *Marine Structures* .

3

IMPACTS OF INTERNAL SOLITARY WAVES

A submerged floating tunnel is suspended under water subject to the threat of internal waves. Internal wave can alter structural buoyancy and hence, affect structural safety and reliability. Internal solitary waves (ISWs), associated with non-linear characteristics, are representative of internal waves. In this chapter, The interaction between an oceanic internal solitary wave (ISW) and a prototype submerged floating tunnel (SFT) is numerically investigated. Effect of oceanic internal solitary wave amplitude, the relative distance of the SFT to the pycnocline, cross-sectional geometry of the SFT, and the density ratio of the two fluid layers are analyzed. The proposed parametric shape in Chapter 2 is applied to assess hydrodynamic forcing acting on the tube under the ISW condition. The hydrodynamic load induced by internal waves acting on the SFT in the present chapter is applied for dynamic response assessment in Chapter 5. The highlights of this chapter are:

- *A two-dimensional numerical internal wave tank is established based on mKdV wave theory.*
- *The mechanism of interaction between internal solitary wave and the SFT is revealed.*
- *The influences of internal wave amplitude, cross-sectional shape, relative distance to the pycnocline, and fluid density ratio on the internal wave and structure interaction are quantified.*
- *The most streamlined SFT cross section geometry (the parametric shape) shows better hydrodynamic performance than circular and elliptical shapes.*

This chapter has been published as: Zou, P. X., Bricker, J. D., Uijttewaal, W. S. (2021). The impacts of internal solitary waves on a submerged floating tunnel. ***Ocean Engineering***, 238, 109762.

3.1. INTRODUCTION

Internal waves have been confirmed by satellite images and in situ observations as ubiquitous in oceanic environments (Vázquez et al. 2008, Klymak et al. 2006). The mechanism of internal waves generation is generally as a result of stratified flows over topographic variations such as sills, ridges, and continental shelf edges, corresponding to an energy conversion from barotropic tide into baroclinic internal wave (Ramirez & Renouard 1998, Hibiya 1986). Internal solitary waves (ISWs), associated with non-linear characteristics, are representative of internal waves. ISW's have been recorded with amplitude over 170 m (Klymak et al. 2006), and have been observed to penetrate the entire water depth. These ISWs can induce large wave forcing and hence cause severe hazards to the operation and maintenance of marine engineering structures.

A moored submerged floating tunnel (SFT), as a novel sea-crossing infrastructure suspended under water, is subject to the impacts of hydrodynamic loads induced by ISWs. Therefore, if an SFT is built in regions active with ISW's, it is imperative to analyze the characteristics of interaction between ISWs and the SFT tube body. The SFT tube can be regarded as a cylindrical structure, which is a common component of marine engineering structures. Previous studies of the ISW's effect on cylinders have been carried out using numerous approaches. Ermanyuk and Gavrilov (Ermanyuk & Gavrilov 2005) experimentally investigated the interaction of a small-amplitude internal solitary wave and a horizontal circular cylinder in a two-layer miscible fluid system, and analyzed the effects of the pycnocline (defined by the boundary separating two liquid layers of different densities) thickness and distance between the cylinder and pycnocline on the hydrodynamic loading on the cylinder. ling Wang et al. (ling Wang et al. 2018) carried out an experimental study on the ISW-induced forces acting on a cylinder and explored the effect of splitter plates on force reduction using numerical simulations. Cui et al. (Cui et al. 2019) experimentally studied the motion and mooring force of a floating model under ISW impact, and found that the ISW amplitude and the model size are crucial factors affecting the structural response. Ding et al. (Ding et al. 2020) investigated the hydrodynamic forces exerted by ISWs on extended and tandem cylinders using OpenFOAM and verified their results against experimental data. However, due to the limitations of these small-scale laboratory tests and simple SFT cross-sectional shapes considered, the characteristics of interaction between ISWs and an SFT under realistic oceanic conditions cannot be properly assessed by the experimental and numerical studies completed thus far.

Empirical methods for ISW-induced load estimation mainly applies the Morison equation. Si et al. (Si et al. 2012) adopted the Morison equation to compute the shear forces and torques induced by ISWs on a rigid cylindrical pile under continuously stratified ocean conditions in the South China Sea. Cai et al. (Cai et al. 2003, 2006, 2008) used the Morison equation, modal separation, and linear regression analysis to estimate the forces and torques resulting from ISWs with and without shear flow on vertical cylindrical piles, and proposed a simple ISW-induced force prediction method based on the dominant term of the global force. Lin and Zan (Lin & Zan 2021) discussed the influence of adopting local or global empirical parameters on the predictability of the ISW force on a cylinder using the Morison Equation, and concluded that the contribution of the nonlinear term is significant. However, the resulting modified coefficients in the Morison formula are not universal, but vary with the adopted ISW theory and model settings.

Research on the impacts of ISWs on other marine engineering structures is extensive. Song et al. (Song et al. 2011) established an analytical model to compute the forces and response motion of a spar platform under ISWs where the drag and inertial forces are computed by the Morison equation. Haibin et al. (Haibin et al. 2016) studied the impacts of a parabolic background current on force and torque exerted by ISWs on the tendon legs of a tension leg platform using the Morison equation. Chen et al. (Chen et al. 2017, 2020) experimentally measured the forces and pitch moments exerted by ISWs on a semi-submersible model to obtain empirical coefficients based on the Morison equation, and examined various wave propagation directions, concluding that the inline and transverse forces are affected significantly by ISWs direction. However, most previous studies focused on vertical cylindrical offshore structures with comparatively small diameters, such as vertical piles or tendon legs. Investigations of ISW impacts on a large-diameter horizontal cylinder such as an SFT are lacking. Moreover, due to the specific structural characteristics of an SFT, its buoyancy-weight ratio (BWR) has a dominant effect on its mooring tension and dynamic response, which influences the serviceability and reliability of the coupled SFT system. The internal wave can directly change the structural buoyancy, and hence, change the BWR. Most previous research on ISW's and marine engineering structures focused either on the detailed turbulent flow forces induced by the ISW, or on the structural response, but combining turbulent flow simulation with structural dynamic response analysis in a systematic assessment had not yet been accomplished.

To eliminate the scale effect, this present chapter studies a full-scale prototype SFT subjected to oceanic ISW. Characteristics of the detailed ISW-SFT interaction during ISW evolution are revealed using Computational Fluid Dynamics (CFD). Dynamic response analysis for a coupled tube-joint-mooring system is then carried out to analyze the ISW impacts on the SFT in Chapter 5. The chapter is structured as follows. The applied ISW theory and oceanic ISW properties are described in Section 3.2. Section 3.3 introduces the model set-up and numerical validation. Section 3.4 quantifies the influence of the ISW amplitude, the SFT cross-sectional shape, the distance from the SFT to the pycnocline, and the fluid density ratio, on the ISW-SFT interaction.

3.2. METHODOLOGY

3.2.1. ISW WAVE THEORY

At present, there are several wave theories that can be applied to describe the shape of an ISW. The Korteweg de Vries (KdV) theory, formulated by Diederic Korteweg and Gustav de Vires, can be adopted to analytically define the internal wave profile. This theory is only suitable for small-amplitude and weakly nonlinear and dispersive waves (Koop & Butler 1981). By increasing its nonlinearity, an extended KdV (eKdV) (Kakutani & Yamasaki 1978) wave theory containing both quadratic and cubic nonlinear terms can be applied. Moreover, a modified KdV theory (mKdV) is formulated for large-amplitude internal waves (Michallet & Barthélémy 1998). The interface displacement governed by the mKdV theory is expressed by Eq.3.1

$$\zeta(x,t)=\frac{a\mathrm{sech}^2[\kappa(x-c_{mKdV}t)]}{1-\mu\tanh^2[\kappa(x-c_{mKdV}t)]} \tag{3.1}$$

where a is the internal wave amplitude; c_{mKdV} is the phase velocity, and μ and κ are fluid thickness coefficients, given by

$$c_{mKdV}=c_m+B[(\alpha a+\beta\bar{h})^2-(\beta^2-\alpha)\bar{h}^2] \tag{3.2}$$

$$\mu=\begin{cases}h''/h' \ if \ \bar{h}>0\\ h'/h'' \ if \ \bar{h}<0\end{cases} \tag{3.3}$$

$$\kappa=(-\frac{B}{A}h''h')^{0.5} \tag{3.4}$$

with

$$c_m^2=\frac{gH}{2}[1-\sqrt{1-\frac{4h_1h_2(1-\rho_1/\rho_2)}{H^2}}] \tag{3.5}$$

$$A=\frac{2c_m}{H'}\{\frac{H'-h_c}{h-h_c}[(H'-h_c)^3+(h-H')^3]+h_c^3\} \tag{3.6}$$

$$B=-\frac{c_m}{2(H'-h_c)^2} \tag{3.7}$$

$$h'=-\frac{\beta}{\alpha}\bar{h}-\frac{1}{\alpha}[(c_{mKdV}-c_m)B^{-1}+(\beta^2-\alpha)\bar{h}^2]^{0.5} \tag{3.8}$$

$$h''=-\frac{\beta}{\alpha}\bar{h}+\frac{1}{\alpha}[(c_{mKdV}-c_m)B^{-1}+(\beta^2-\alpha)\bar{h}^2]^{0.5} \tag{3.9}$$

$$\alpha=1+\frac{5}{4}\frac{H-H'}{H'} \tag{3.10}$$

$$\beta=1+\frac{1}{2}\frac{H-H'}{H'} \tag{3.11}$$

$$H=h_1+h_2,\bar{h}=h_2-h_c,H'=H-\frac{c_m^2}{g} \tag{3.12}$$

$$\frac{h_c^2(H-h_c)}{(H'-h_c)^3}=\frac{\rho_2}{\rho_1} \tag{3.13}$$

where h_1 and h_2 are the thickness of the upper-layer and lower-layer, respectively. ρ_1 and ρ_2 are the density of the upper-layer and lower-layer, respectively; H is total water depth; and h_c is the critical level. The polarity of the ISW is determined by the position of the interface with respect to the critical level h_c: when the interface is below (above) h_c the ISW is of elevation (depression).

The horizontal velocities of water particles in the upper and lower layers for a depression-type ISW are given by

$$u_i(x,t) = (-1)^{i+1}\frac{c_{mKdV}\zeta(x,t)}{h_i + (-1)^{i+1}\zeta(x,t)} \tag{3.14}$$

where $i = 1{,}2$ represents the upper and lower layer fluids, respectively.

The characteristic "wavelength" of the mKdV ISW is expressed as

$$\lambda = 2(H-h_c)\sqrt{\frac{(H-h_c)^3 + h_c^3}{3Hh'h''}} \tag{3.15}$$

The integral frequency scale ω_m of the mKdV ISW is shown as

$$\omega_m = \frac{c_{mKdV}\kappa\mu^{1/2}}{\operatorname{arctanh}\mu^{1/2}} \tag{3.16}$$

3.2.2. ISW PROPERTIES

Based on field observations and high-resolution satellite images at Wenchang Station (112° E, 19°35' N) (shown in Fig.3.1) from April to October, 2005, strong ISWs were identified in the continental shelf area, with the largest ISW amplitude 25~35 m, and the ISW packet near Hainan Island is dominated by the diurnal tide (Xu et al. 2010). As one of the potential SFT construction sites in China (Yan et al. 2016), the Qiongzhou Strait is close to Wenchang Station. Note that detailed reproduction of internal wave structure inside the strait is not the aim of this research, but rather to approximate the ISW's observed in the region for a conservative analysis of the SFT dynamic response. Therefore, the ISW characteristics recorded at Wenchang Station are applied for the analysis of hydrodynamic forces, serviceability, and reliability of the SFT in this study (Zou et al. 2021*a*). Since the measured ISW amplitude is quite large compared with the strait depth of around 100 m, the mKdV theory is adopted for the ISW description.

3.3. NUMERICAL MODEL

3.3.1. MODEL SETUP

CROSS-SECTION GEOMETRY

Most SFT cross-sections have been designed with a circular shape (Lin et al. 2019, Jin & Kim 2020, Deng et al. 2020), primarily due to the superior hydrodynamic and blast load behaviour compared with a rectangular shape (Gang et al. 2018, Kristoffersen et al. 2019). An elliptical cross-section has more streamlined hydrodynamic behaviour, experiencing smaller displacement and less stress than circular and rectangular shapes (Li & Jiang 2016, Mandara et al. 2016). However, in this chapter, the parametric shape based on the Bézier-PARSEC (BP) curve in Chapter 2 to describe the SFT cross-section is applied. In order to determine the optimal SFT cross-section, the hydrodynamic performance of this parametric shape is tested and compared with the simpler circular and elliptical

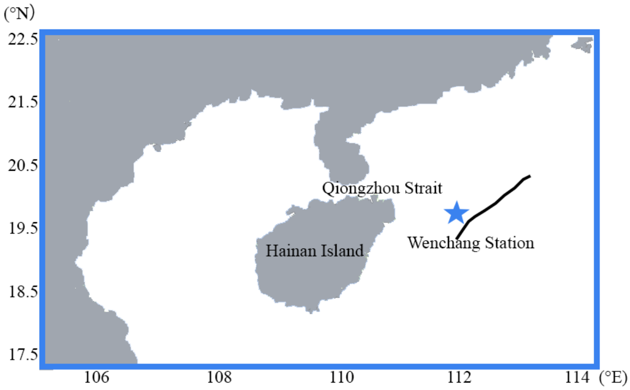

Figure 3.1: The locations of Wenchang station and the Qiongzhou Strait. The blue star denotes Wenchang observation station. The black line indicates the sketch of the leading solitary wave

shapes under the tsunami impact. The detailed parametric Bézier curve information (the definitions of b, y_t, r) is described in Chapter 2. In this study, we choose the Bezier parameters $b = 1.5$ m, $r = 0.5$ m, and $y_t = 4$ m to design the SFT cross-section. As per the current technical standards and feasibility studies (Muhammad et al. 2017, AASHTO 2018), the cross-section must provide sufficient space for traffic, evacuation, ventilation, ballast, inspection and other services and utilities. In order to fix the shape parameters for comparison, SFT cross-sections with lateral and vertical clearances of $H = 5$ m and $W = 11$ m, respectively (as required by road tunnel construction guidelines), is selected for the hydrodynamic analysis of all the three shapes (Fig.3.2). The semi-minor axis of elliptical shape is 4 m, to keep the same vertical clearance as the parametric Bezier curve SFT profile. Assuming the tunnel wall thickness is 1 m, the maximum width and height of the parametric, circular, and elliptical shapes are 20 m × 10 m, 14 m × 14 m, and 16 m × 10 m, respectively.

NUMERICAL MODEL SETTING

A two-dimensional numerical ISW tank is generated using ANSYS Fluent to simulate the interaction between an ISW and the SFT (Fig.3.3 (a)). The computational domain is 4500 m in length and 100 m in height, filled with a stratified two-layer fluid. The center of the SFT is located 200 m from the inlet. The thicknesses of the upper-layer and lower-layer fluids are 30 m and 70 m, respectively. For a typical case the ISW, the amplitude a is selected as 20 m with a characteristic “wavelength” of 144 m. The densities of the fluids in the upper-layer and lower-layer are 1022 $\mathrm{kg\,m^{-3}}$ and 1024 $\mathrm{kg\,m^{-3}}$, respectively, based on the actual oceanic condition, in which the oceanic density difference is generally less than $3 \sim 4\,\mathrm{kg\,m^{-3}}$ (Zhu et al. 2016). The VOF method (Hirt & Nichols 1981) with a dispersed-type interface model is applied to capture the pycnocline. The VOF method is accomplished by the solution of a continuity equation for the volume fraction σ of the i^{th} phase. The volume fraction equation is obtained with Eq. 3.17, and the fluid viscosity μ and density ρ in each grid cell are reconstructed by volume phase averaging with

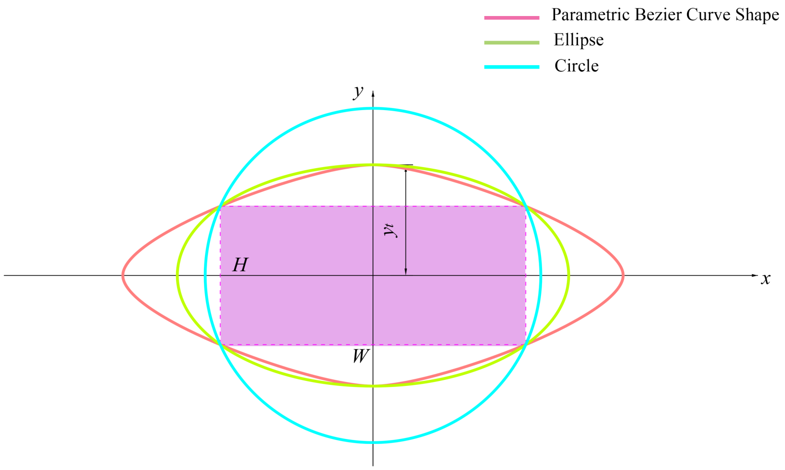

Figure 3.2: Three SFT cross-sections dimension sketch

Eqs.3.18 and 3.19:

$$\frac{\partial \sigma_i}{\partial t} + \nabla \cdot (\sigma_i \vec{v}_i) = 0 \tag{3.17}$$

$$\rho = \sum_{i=1}^{n} \sigma_i \rho_i \tag{3.18}$$

$$\mu = \sum_{i=1}^{n} \sigma_i \mu_i \tag{3.19}$$

where σ_i is the volume fraction of the i^{th} phase, and v_i is the velocity of the i^{th} phase.

Since the surface wave amplitude is relatively small compared with the ISW amplitude, the top boundary is assumed to be a “rigid lid” in all simulations. Freestream quantities of turbulence intensity and turbulence length scale are specified at the inlet boundary in Chapter 2 section 2.6(Zou et al. 2021*b*). An outflow boundary is employed at the outlet. A simplified no-slip hydraulically smooth wall condition is applied on the SFT cross-section surface and the bottom boundary. The unsteady Reynolds-Averaged Navier-Stokes (URANS) equations with an RNG $k-\epsilon$ turbulence model are applied with a standard wall function. The reliability of this model for hydrodynamic force prediction of the SFT at high Reynolds numbers was verified in Chapter 2(Zou et al. 2020). The URANS model was verified for its ability to provide sufficiently efficient and accurate ISW-induced force predictions (Liu et al. 2020) and vortex generation simulation (Hsu et al. 2004). However, the detection of small flow features such as vortex dynamics in the boundary layer should be simulated by LES or DNS models, which incur additional computation loads and are beyond the scope of this research. The computational domain is divided into several blocks of different resolutions (Fig.3.3 (b)). The subdomain around the SFT cross-section surface is a 30 m × 30 m rectangular block with a

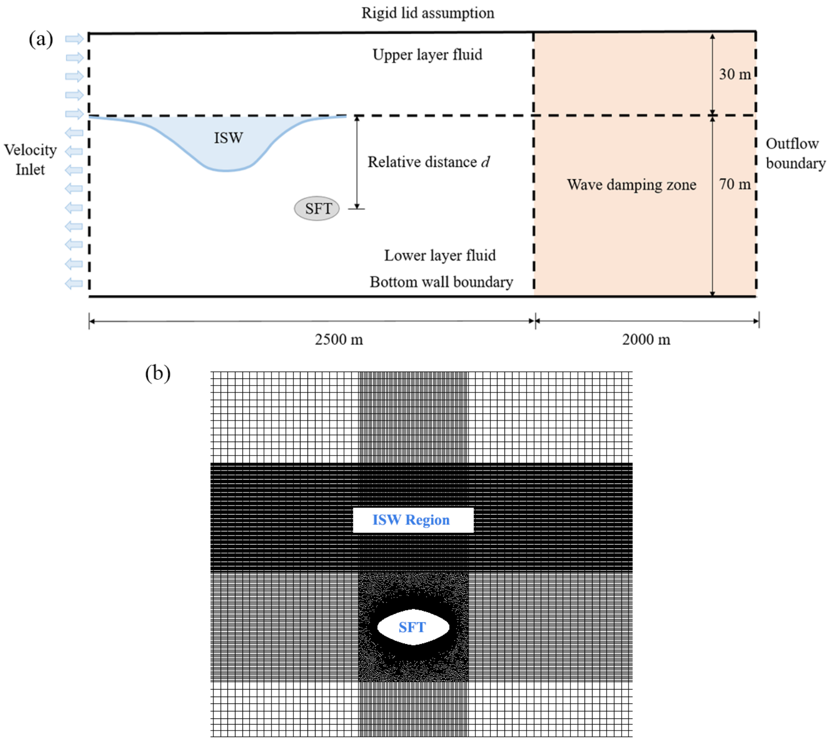

Figure 3.3: Model sketch. (a) Computational domain; (b) Local grid settings in different regions

high-quality unstructured mesh , including 40 layers of quadrangular cells that cover the boundary layer. The first grid layer cell thickness normal to the SFT surface is 0.003 m, within the acceptable range of Y^+ at 30 ~ 200 (Kuzmin et al. 2007). Above this first cell, the cell thickness stretches with a growth rate of 1.2. The subdomain within the ISW propagation region has a horizontal and vertical mesh size of 2 m and 0.2 m, respectively. The adjacent subdomain crossing the SFT has a minimum grid size of 0.4 m. The structured mesh size in the rest of the subdomain is generally 2 m, and in the damping zone, an increasingly coarse mesh with a bias factor of 2 is set to cause extra numerical diffusion. An adaptive time-step was selected, and the maximum Courant number is set to 0.25. The PISO (Pressure-Implicit with Splitting of Operators) algorithm is used for pressure-velocity coupling. A high-performance computing (HPC) cluster is applied to run parallel computation tasks.

WAVE GENERATION AND ABSORPTION

The direct inlet velocity prescription method is used to generate an ISW at the inlet boundary by a User Defined Function (UDF) (ANSYS 2019), where the theoretical horizontal orbital velocities and surface elevation are imposed directly (Miquel et al. 2018), and the pressure is set to be hydrostatic. The UDF specifies the velocity components and fluid volume fraction for each cell on the boundary. Cavaliere et al. (Cavaliere et al. 2021) revealed that the pycnocline thickness affects ISWs kinematics. For a thick pycnocline layer condition, both the wave celerity and the velocity gradients decrease, and the hydrodynamic force on the SFT induced by the ISW is reduced. Therefore, as a conservative calculation of the hydrodynamic force on the SFT, only a thin pycnocline between the two-layer fluid is added. The thin pycnocline was set by a smooth "tanh" initial density distribution between the upper and lower layers as in (Zhu et al. 2016, Ding et al. 2020). To avoid numerical instability at the interface, in this study, the ISW horizontal velocity distribution in the pycnocline layer is given by a linear velocity transition between the upper and lower layers, as shown in Eq.3.20.

$$u(y) = -\frac{u_1 + u_2}{d_p}[y - (y_c - \frac{d_p}{2})] + u_2 \tag{3.20}$$

where y is the vertical coordinate of the grid; y_c is the position of the mid-pycnocline layer; d_p is thickness of the pycnocline layer.

In order to determine the appropriate pycnocline layer thickness, a sensitivity analysis is carried out. We consider three different pycnocline layer thicknesses (0.05 m, 1 m, and 5 m). These are tested for the case with ISW amplitude of 20 m, SFT relative distance from the pycnocline of 10 m, and parametric cross section shape. In order to shorten the simulation time, fluid densities of 1022 $\mathrm{kg\,m^{-3}}$ and 1054 $\mathrm{kg\,m^{-3}}$ in the upper-layer and lower-layer are selected, respectively. Time series of the ISW-induced horizontal and vertical forces per meter on the SFT for each pycnocline layer thickness are shown in Fig.3.4. It can be found that flow instabilities occur (Fig.3.4 (a)) with $d_p = 0.05$ m, while spikes can be effectively eliminated with d_p = 1 m or 5 m. However, as d_p increases to 5 m, the hydrodynamic forces on the SFT are underpredicted with a maximum force deviation around 2 kN compared to $d_p = 0.05$ m, whereas the difference in force computation between d_p = 1 m and 0.05 m is minor. This indicates that stable and accurate results are achieved with a pycnocline layer thickness of 1 m; and hence, d_p = 1 m is adopted in subsequent simulations.

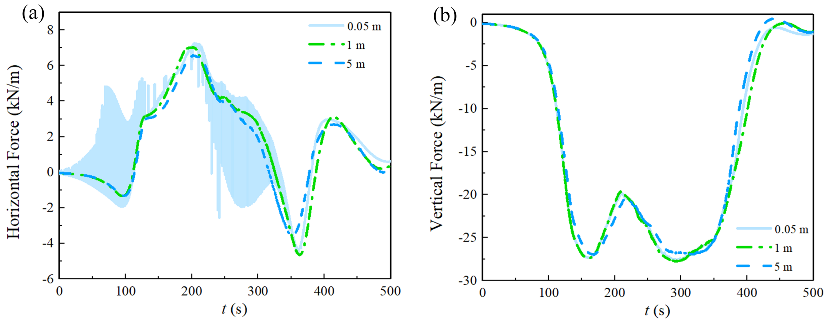

Figure 3.4: Sensitivity of force per meter to pycnocline layer thickness. (a) horizontal unit force on the SFT; (b) vertical unit force on the SFT.

For wave absorption, a dampening sink term given by Eq. 3.21 is added in the momentum equation within a damping length of 2000 m from the outlet boundary to avoid wave reflection (ANSYS 2019).

$$S = -[C_1 \rho v + \frac{1}{2} C_2 \rho |v| v] f(x) f(y) \tag{3.21}$$

where C_1 and C_2 are linear and quadratic damping resistance, respectively; $f(x)$ and $f(y)$ are damping functions for inline and cross flow directions, respectively; v is flow vertical velocity. It features a combination of linear and quadratic damping, which allows the use of either one or a combination of both approaches. In this research, $C_1 = 10\,\mathrm{s}^{-1}$; $C_2 = 10\,\mathrm{m}^{-1}$.

3.3.2. MODEL VALIDATION

The dimensionless hydrodynamic force on an isolated cylinder is defined in Eq.3.22.

$$C_{x,y} = \frac{F_{x,y}}{(\rho_2 - \rho_1) g A} \tag{3.22}$$

where F_x and F_y are horizontal and vertical force per meter on the cylinder, respectively; g is gravitational acceleration; and A is the cross-sectional area of the cylinder. Note that the forces on the cylinder are normalized in Eq.3.22, and hence, $C_{x,y}$ is dimensionless. If ρ_1 is close to ρ_2, the hydrodynamic force $F_{x,y}$ will be close to 0. Thus, $C_{x,y}$ will not be infinite.

Numerical results are further verified by comparison to experimental data of horizontal force on the cylinder (Ermanyuk & Gavrilov 2005) and an empirical formula. In this experiment, the fluid densities of the upper-layer and lower-layers are $\rho_1 = 1000\,\mathrm{kg\,m}^{-3}$ and $\rho_2 = 1021\,\mathrm{kg\,m}^{-3}$, respectively. The thicknesses of the upper-layer and lower-layers are $h_1 = 4$ cm and $h_2 = 8.5$ cm, respectively. The center of the 1.5 cm diameter cylinder is located a distance of $h_0 = 9$ cm from the flume bottom. The ISW amplitude is 0.77 cm. Per the Morison Equation, the horizontal hydrodynamic load per meter can be estimated by the sum of the inertial and drag forces, given by Eq. 3.23

$$F_x(t) = \frac{1}{2} C_d \rho D |u| u + C_m \rho A \frac{\partial u}{\partial t} \tag{3.23}$$

where u is the horizontal velocity component of the ISW fluid particles which can be computed by using Eq.3.14; C_m and C_d are inertia and drag coefficients, respectively, and can be set as $C_m = 2.0$, $C_d = 1.2$, based on previous studies (Cai et al. 2003, 2006).

The comparison of the horizontal hydrodynamic loads on the cylinder from each study is shown in Fig.3.5, where Vt/H_0 is a dimensionless value from (Ermanyuk & Gavrilov 2005). It illustrates that the Morison equation generally overpredicts the negative hydrodynamic force and underestimates the positive hydrodynamic force, while the numerical simulation results provide a better agreement with the experimental data. The discrepancy between the numerical and experimental results can be attributed to a difference of the ISW generation mechanism, where a hump-type ISW was produced by the wave-maker in the experiment, while the mKdV theory is applied in the numerical simulation.

To elucidate the mechanism of ISW-SFT interaction under oceanic conditions and investigate the influence of factors including the ISW amplitude, the SFT relative distance to the pycnocline (defined as the vertical distance between the centre position of the SFT and the initial location of the interface between the two-layers of fluids), the SFT cross-sectional shape, and fluid density on the SFT hydrodynamics, a sensitivity analysis is conducted by comparing the temporal variation of force coefficients on the SFT, the velocity and pressure fields in the vicinity of the SFT at specific moments, and the corresponding interface position of the two fluid layers.

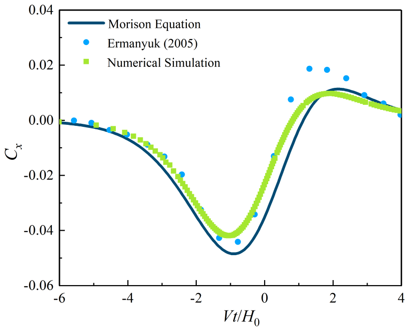

Figure 3.5: Comparison of horizontal force coefficients among the Morison Equation, experimental data, and numerical simulation.

3.4. SENSITIVITY ANALYSIS OF INFLUENCE FACTORS

3.4.1. EFFECT OF ISW AMPLITUDE

Cases of ISW amplitude a = 20 m, 25 m, 30 m, and 35 m are selected, with a relative distance to the pycnoclilne of 40 m, parametric cross-sectional shape, and upper- and lower-layer densities of $1022\,\mathrm{kg\,m^{-3}}$ and $1054\,\mathrm{kg\,m^{-3}}$, respectively, to investigate the influence of ISW amplitude on the hydrodynamic force on the SFT. Time series of force coefficient variation in horizontal and vertical directions for different ISW amplitudes are illustrated in Fig.3.6. Positive horizontal force means the force direction is the same as the ISW propagation direction, and positive vertical force means the force direction is upward (assuming that the initial condition is when the SFT is neutrally buoyant). It can be found that C_x drops firstly to its negative maximum and undergoes a sharp increase to about double the maximum magnitude, followed by a plunge and oscillation around the equilibrium after the ISW passes over the SFT. It is worth noting that the larger the ISW amplitude is, the later the maximum negative force occurs. For a large ISW amplitude, the ISW can act on the SFT surface directly, and a strong interaction between the ISW and the SFT occurs, along with fluid mixing and wave dissipation and reflection, which prolongs the interaction time. Thus, the larger the ISW amplitude is, the later the maximum negative force occurs.

However, according to Eqs.3.1 and 3.14, the ISW's flow velocities increase with increasing the ISW's amplitude; and hence, the ISW with a large amplitude propagates faster than those smaller amplitude cases. The irregularity in the temporal distribution of C_x and C_y for large ISW amplitudes also indicates the complex mechanisms of the strong interaction between the ISW and the SFT. It can be deduced that reflected waves bounce back from the SFT, contributing to secondary peaks and interfacial instabilities. This also shows that the absolute maximum C_x and C_y increase with increasing ISW amplitude. The absolute maximum C_x reaches 0.6 at $a = 35$ m, while the absolute maximum C_y is 2.7.

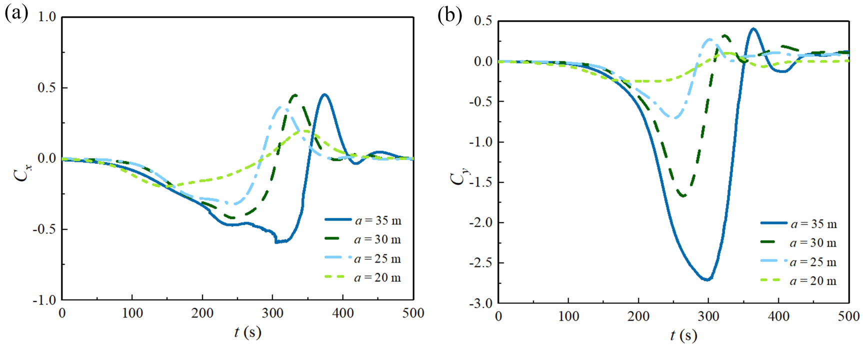

Figure 3.6: Time series of force coefficients on the SFT for different ISW amplitudes. (a) horizontal force coefficient (positive direction is ISW propagation direction) ; (b) vertical force coefficient (positive direction is upward)

Fig.3.7 shows the volume fraction and velocity field distributions of the two layers of fluids when the horizontal force coefficient on the SFT reaches its negative maximum. Thus, different characteristics of the ISW-SFT interaction for various ISW amplitudes can be clearly elaborated. Note that the negative maximum of C_x increases with increasing ISW amplitude, which corresponds an increase of the ISW water particle velocity magnitude in each fluid layer.

At $a = 20$ m (Fig.3.7 (a, b)), the pycnocline keeps stable, and no evident deformation of the ISW profile or fluid mixing can be observed. However, at $a = 25$ m (Fig.3.7 (c, d)), the ISW profile gets distorted, and mixing of fluids across the pycnocline is gradually generated above the leading-edge of the SFT. As the ISW trough approaches the SFT, the increasing velocities of both the convergence flow in the upper layer and divergence flow in the lower layer enlarge the shear stress at the interface, which enhances disturbance of the flow, and triggers mixing instabilities. The thickness of the mixing layer increases with increasing ISW amplitude. The flow area is partially blocked by the SFT, and the ISW profile distorts. The interface of the ISW is generally parallel to the upper left quadrant SFT surface and steepens with increasing ISW amplitude. The ISW energy is dissipated, and backflow and mixing are generated, making the flow field at the interface complex (Fig.3.7 (d, f)).

For $a = 35$ m (Fig.3.7 (e, f)), as the ISW propagates, the ISW can act on the SFT surface directly, which can lead to reflection of the ISW. The irregularity at the local negative maximum of the horizontal force (Fig.3.6 (a)) can be attributed to distortion of the ISW shape and strong interaction between the ISW and the SFT. However, C_x for $a = 35$ m does not show an increase after the ISW trough passes over the SFT compared with a = 30 m since the strong ISW-SFT interaction for a = 35 m dissipates the wave energy ; therefore, the ISW amplitude is reduced after passing over the SFT.

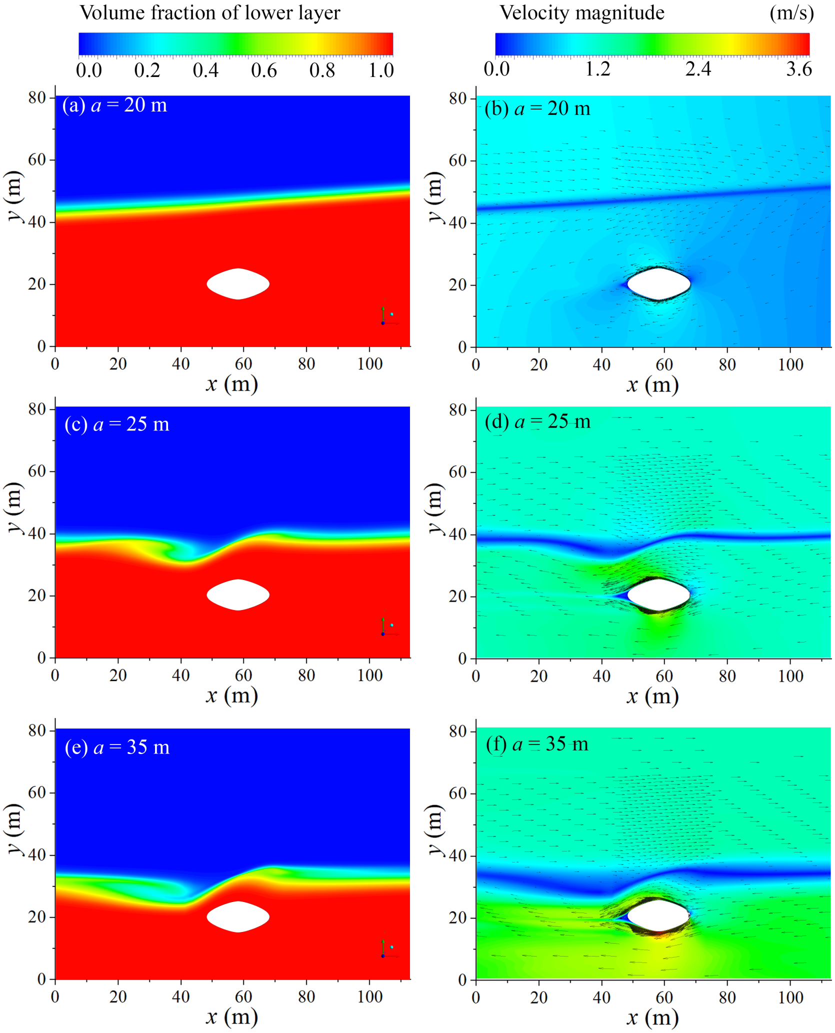

Figure 3.7: Volume fraction and velocity field around the SFT for different ISW amplitudes. The ISW amplitudes from top to bottom are 20 m, 25 m, and 35 m, respectively.

3.4.2. EFFECT OF SFT CROSS-SECTION GEOMETRY

Circular, elliptical, and parametric SFT cross section shapes are investigated for an ISW amplitude of 20 m, relative distance to the pycnocline of 40 m, and upper- and lower-layer fluid densities of 1022 $\mathrm{kg\,m^{-3}}$ and 1054 $\mathrm{kg\,m^{-3}}$, respectively, to investigate the influence of the SFT cross-section shape on the hydrodynamic forcing of the SFT.

Time series of force coefficients in horizontal and vertical directions are illustrated in Fig.3.8. The circular shape has the largest maximum absolute values of forces, while the parametric shape, with its streamlined curvature, generates the minimum forcing oscillation among the three shapes. It can also be found that C_x of all three shapes in both directions decreases at first, continuously increases afterward, and gradually decreases back to its equilibrium. The parametric shape experiences its negative maximum of C_x at 150 s, while the elliptical and circular shapes reach their negative maxima after 200 s. As shown in Fig.3.8, the circular shape's force signal has a lower oscillation frequency than the elliptical shape.

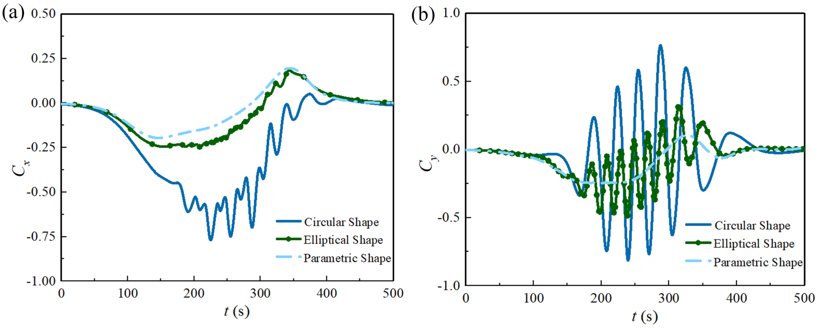

Figure 3.8: Time series of force coefficients on the SFT for different SFT cross-sectional shapes. (a) horizontal force coefficient (positive direction is ISW propagation direction) ; (b) vertical force coefficient (positive direction is upward).

Fig.3.9 shows the volume fraction and velocity field distributions of the two layers of fluids when C_x on the SFT reaches its negative maximum. Characteristics of the ISW-SFT interaction as a function of SFT cross-sectional shape can be clearly elaborated. For the circular and elliptical cross-sectional shapes (Fig.3.9 (b, d)), the negative maximum value of C_x generally occurs when the ISW trough is above the apex of the SFT. The flow streamlines at the edges of the SFT are distorted by the bluff body, and the shape curvature in turn increases the velocity magnitude at the apex and nadir points. Furthermore, as the flow passes over the SFT, the shear stress near the SFT surface grows, and the flow separates from the SFT due to the strong adverse pressure gradient (APG) resulting from the shape curvature, triggering a wide wake recirculation regime and periodic vortex shedding at the left edge (note that the ISW trough travels to the right, resulting in flow toward the left in the lower fluid layer). The vortex shedding process, together with the steady pressure gradient, amplifies the gross hydrodynamic force on the SFT. The horizontal force induced by vortex shedding partially compensates for the reduction in horizontal force when the ISW trough is above the SFT (Fig.3.8 (a)).

From Fig.3.8 (b), the frequency of vortex shedding can be estimated to be around 0.03 Hz. The intrinsic ISW characteristic frequency is 0.0078 Hz based on Eq.3.16. It can be deduced that the vortex shedding frequency is much faster than the intrinsic ISW characteristic frequency. Vortex shedding affects the SFT around 170 s before the ISW trough passes over the SFT, and dissipates after the back shoulder of the ISW passes over the right edge of the SFT at around 380 s. If the vortex shedding frequency is close to the structural natural frequency, the occurrence of fatigue damage to the SFT tube and its support connections should be considered as a design criterion. The circular shape with its large curvature increases the form drag on the SFT. The ISW profile shoals above the circular shape, and the distorted wave profile entrains the fluid from the upper layer into the lower layer, causing significant fluid mixing, strong ISW-SFT interaction, and energy dissipation (Fig.3.9 (a, b)). Furthermore, for the circular shape, Fig.3.8 shows that the hydrodynamic force induced by vortex shedding dominates the oscillation of vertical force on the SFT, whereas the parametric shape experiences reduced flow separation and vortex shedding.

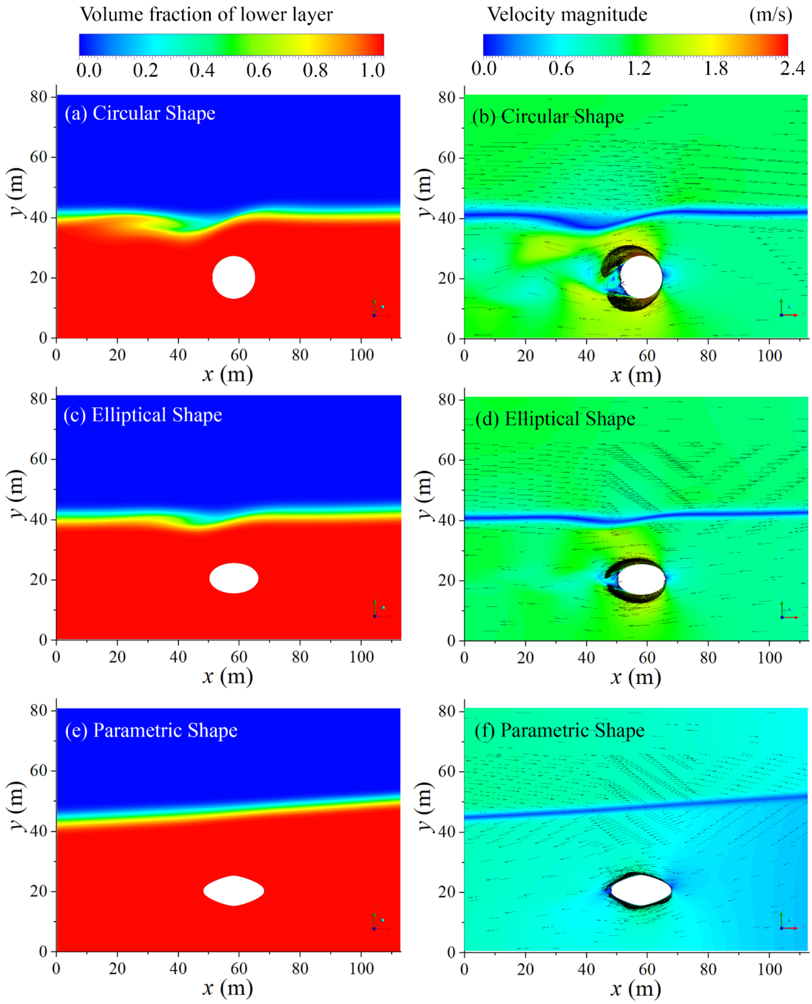

Figure 3.9: The volume fraction and velocity field around the SFT for different SFT cross-sectional shapes. The SFT cross-sectional shapes from top to bottom are circle, ellipse, and parametric shape, respectively. The undisturbed ISW amplitude is 20 m.

3.4.3. EFFECT OF SFT RELATIVE DISTANCE TO PYCNOCLINE

The relative distance of the SFT to the pycnocline is defined as the vertical distance between the centre position of the SFT and the initial interface between the two fluid layers. Cases with SFT relative distance of $d = 0$ m, 10 m, 20 m, 30 m, and 40 m are selected with an ISW amplitude of 20 m, parametric cross-sectional shape, and upper- and lower-layer densities of $1022\,\mathrm{kg\,m^{-3}}$ and $1054\,\mathrm{kg\,m^{-3}}$, respectively, to investigate the influence of the SFT relative distance to the pycnocline on the hydrodynamic forcing of the SFT. Forces on the SFT for different relative distances from the SFT to the pycnocline are shown in Fig.3.10. The oscillatory component of force on the SFT is quite different with different relative distances, due to a complex combination of buoyancy, drag, and inertia force contributions. Apart from the case of $d = 0$ m, the absolute maximum force on the SFT decreases with increasing relative distance. The maximum horizontal force coefficient is for $d = 10$ m, with a value of $C_x = 0.5$, while the absolute maximum C_y is for $d = 10$ m with a value of $|C_y| = 2.0$. In order to further elaborate the effect of relative distance on the forces affecting the SFT, the evolution of the pycnocline location and velocity field in the vicinity of the SFT at different time instants are explored for the cases relative distance of 10 m and 40 m.

For $d = 10$ m (Fig.3.11), as the ISW propagates and approaches the SFT, the SFT is fully submerged in the bottom-layer fluid at the outset. The horizontal water particle velocity above the upper left quadrant surface of the SFT increases when the SFT's front shoulder touches the top left edge of the SFT at 96 s due to the narrowed flow cross-sectional area (Fig.3.11 (a, b)). The increased pressure acting on the right edge increases the horizontal force on the SFT until its local negative maximum is reached (Fig.3.10 (a)). Afterwards, the ISW profile is distorted when it interacts with the SFT and separates into two parts: one part of the ISW is transmitted over the SFT and the other part is reflected. Assuming that the initial condition is when the SFT is neutrally buoyant; as the front shoulder of the ISW gradually crosses over the SFT, the buoyancy continuously reduces while the vertical force increases (Fig.3.10 (b)) until the interface between the two layers of fluid hits the lower surface of the SFT at 200 s (Fig.3.11 (c, d)). The upper surface of the SFT is fully submerged in the upper layer fluid and the tangential water particle velocity increases near SFT apex at 200 s, while the velocity near the lower surface reduces to 0. This ultimately causes a clear velocity difference between the upper and lower half of the SFT, inducing an upward force on the SFT, shown as a "hump" in Fig.3.10 (b). The water particle velocity near the right edge half is generally higher than near the left edge half. Furthermore, a small amount of reverse flow is generated below the lower right edge, enhancing the horizontal force on the SFT (Fig.3.10 (a)). At around 368 s, the back shoulder of the ISW hits the SFT (Fig.3.11 (e, f)), increasing the local water particle velocity. The increased pressure acting on the right edge increases the horizontal force to its local negative maximum (Fig.3.10 (a)). Similarly, as the back shoulder of the ISW crosses over the SFT, the buoyancy of the SFT continuously increases (Fig.3.10 (b)), and as the back shoulder of the ISW hits the SFT upper right quadrant at 419 s (Fig.3.11 (g, h)), the water particle velocity magnitude near the right edge surface increases, and hence, the horizontal force ranks to its local positive peak value (Fig.3.10 (a)). Also note that the fluid mixing layer thickness increases as the ISW propagates and interacts with the SFT.

For $d = 40$ m (Fig.3.12), the forcing time series on the SFT is less complex because the SFT is fully submerged in the bottom layer during the whole ISW propagation process. When the ISW front shoulder passes above the SFT, the horizontal water particle velocity is opposite the ISW propagation direction, generating a stagnation point at the upper right quadrant. The flow velocity rapidly increases near the lower surface of the SFT, resulting in a larger dynamic pressure (so lower static pressure in the non-stagnated area) along the lower surface than the upper half of the SFT (Fig.3.12 (a, b)).Both the horizontal and vertical forces in Fig.3.10 decrease at $t = 150$ s. When the ISW trough propagates above the SFT apex at around 242 s (Fig.3.12 (c, d)), the stagnation point at the rear moves to the right edge tip, and the dynamic pressure difference between the right and left quadrants of the SFT decreases. As the ISW back shoulder propagates above the SFT at 348 s (Fig.3.12 (e, f)), the stagnation points at the rear moves to the lower surface. At the same time, water particle speed acting on the upper right surface is higher than the lower right surface. The flow separates and forms a wake region at the left edge, which increases the pressure difference between the front and rear surfaces of the SFT, resulting in an increase in the horizontal force (Fig.3.10 (a)). From Fig.3.10 (b), it is clear that the vertical force on the SFT is affected significantly by the relative distance of the SFT to the pycnocline. The buoyancy of the SFT also changes significantly as a function of the relative distance to the pycnocline, and contributes to the vertical force, leading to a clear enhancement of the vertical force on the SFT for $d = 10$ m compared with $d = 40$ m. It can be deduced that in this study, the buoyancy change dominates the vertical force distribution.

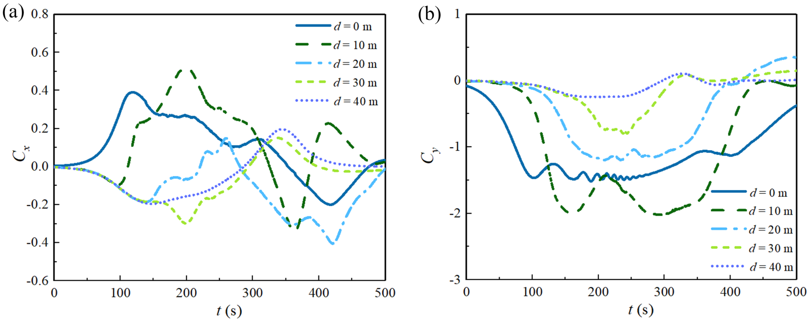

Figure 3.10: Time series of force coefficients on the SFT for different SFT relative distances to the pycnocline. (a) horizontal force coefficient (positive direction is ISW propagation direction) ; (b) vertical force coefficient (positive direction is upward)

However, we note that the results above partially contradict the achievements by Ermanyuk (Ermanyuk & Gavrilov 2005) and Ding et al. (Ding et al. 2020), which concluded that the horizontal load is maximum when the cylinder is located on the bottom of the flume and is minimum when the cylinder is near the interface. This discrepancy is induced by the ISW properties, and the ratio of ISW amplitude to SFT cylinder cross-section diameter is very different. With the confined model scales and a small ISW amplitudes of their studies, they did not observe the complex flow field, strong interaction between ISW and structure, nor the dramatic buoyancy shift of the structure seen in our research. This underscores the necessity of large-scale modeling of the SFT under real oceanic conditions that cannot be simulated in laboratory experiments.

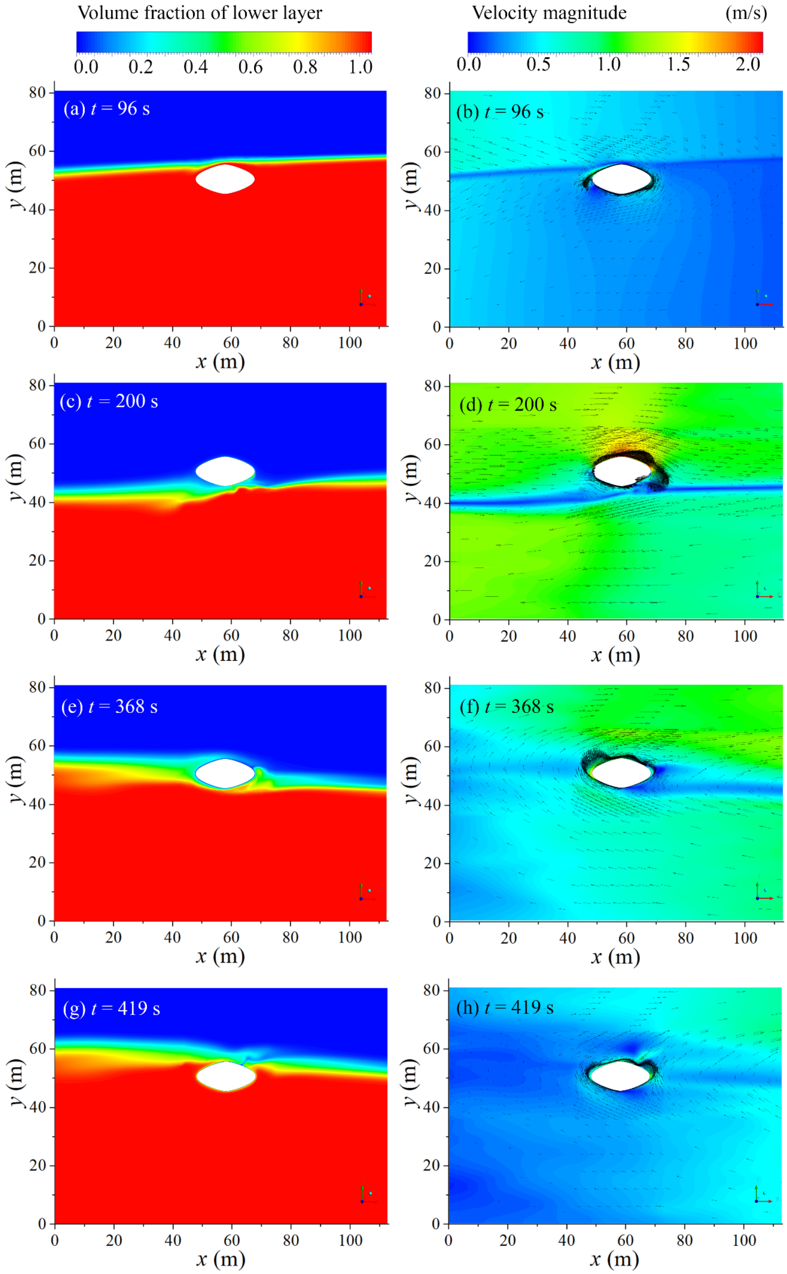

Figure 3.11: The volume fraction and velocity field around the SFT for relative distance to the pycnocline of 10 m. The simulation times from top to bottom are 96 s, 200 s, 368 s, and 419 s, respectively. The undisturbed ISW amplitude is 20 m

Note that the existence of buoyancy change and large velocity gradients at the fluid interface induces prominent vertical loads and shear flows, which should be further evaluated in dynamic structural analysis.

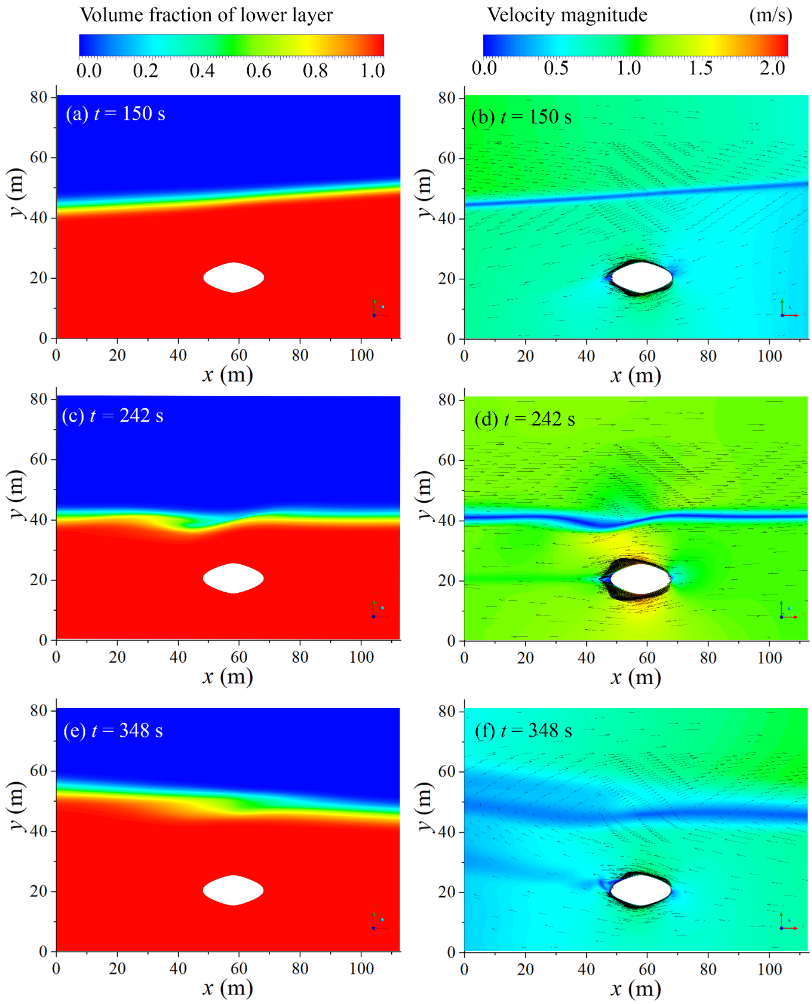

Figure 3.12: The volume fraction and velocity field around the SFT for relative distance to the pycnocline of 40 m. The simulation times from top to bottom are 150 s, 242 s, and 348 s, respectively. The undisturbed ISW amplitude is 20 m

3.4.4. EFFECT OF FLUID DENSITY

Cases with the fluid density ratio of the two layers $\rho_1/\rho_2 = 0.970$, 0.980, 0.990, and 0.998 with a fixed upper-layer density of $1022\,\mathrm{kg\,m^{-3}}$ but varying lower-layer density are selected. An ISW amplitude of 20 m, relative distance to the pycnocline of 40 m, and parametric cross-sectional shape are used for all the cases, to investigate the influence of the fluid density on the hydrodynamic forcing of the SFT.

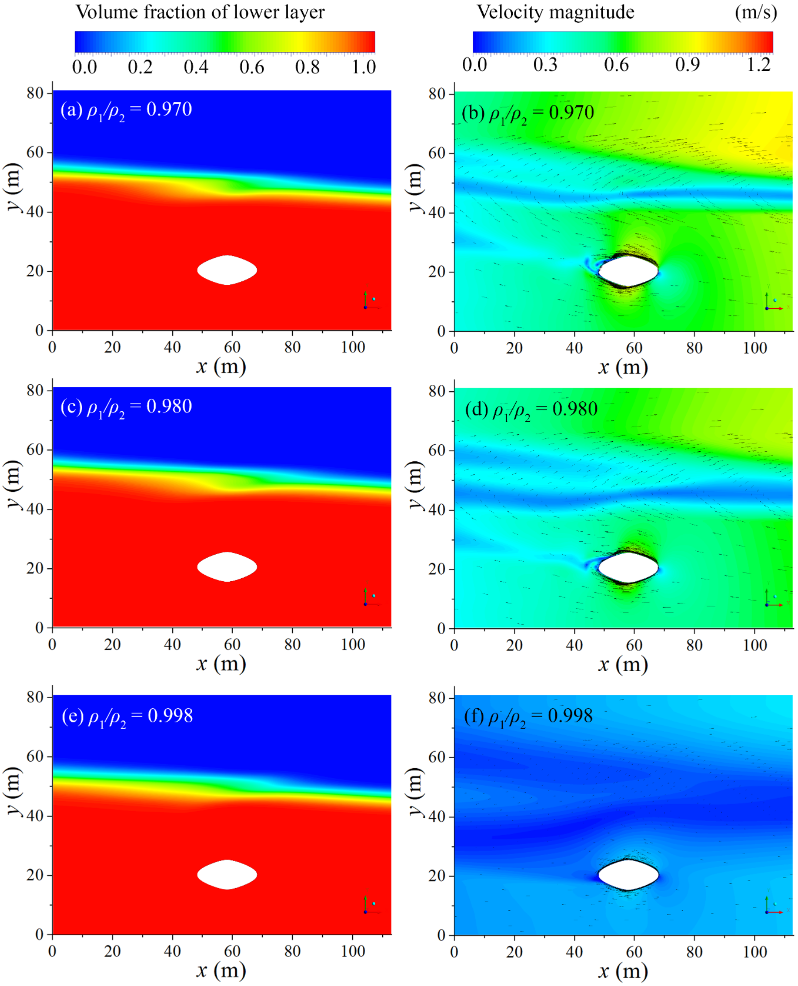

Figure 3.13: The volume fraction and velocity field around the SFT for different fluid density ratios. The fluid density ratios, from top to bottom, are 0.970, 0.980, and 0.998 s, respectively. The undisturbed ISW amplitude is 20 m

Fig.3.13 shows the volume fraction and velocity field distributions in the two layers when C_x reaches its positive maximum. As the fluid density ratio increases, the velocity magnitude of water particles decreases in both the upper- and lower-layers. Also, the water particle speed at the nadir/apex of the SFT decreases with increasing fluid density ratio. However, from Fig.3.13 (b, d, f), it is seen that the thickness of fluid mixing at the interface increases with increasing fluid density ratio. Fig.3.14 illustrates that the absolute maximum of the force coefficient remains almost unchanged for different fluid density ratios, indicating the fluid density ratio is not a crucial factor for the dimensionless hydrodynamic force on the SFT. According to Eq.3.22, the ISW-induced hydrodynamic force on the SFT is generally proportional to the fluid density difference. Per the mKdV theory in Eq.3.14, the convection-diffusion process is inhibited as the fluid density ratio increases, due to the decrease of travelling wave speed.

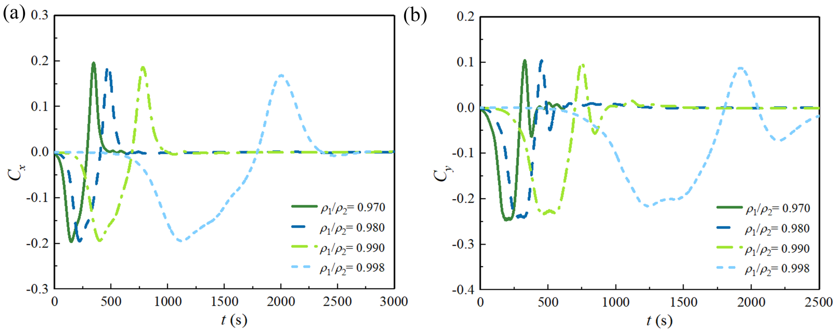

Figure 3.14: Time series of force coefficients on the SFT for different fluid density ratios. (a) horizontal force coefficient (positive direction is ISW propagation direction) ; (b) vertical force coefficient (positive direction is upward)

3.5. CONCLUSION

In this chapter, the CFD software Fluent is applied to simulate the oceanic ISW's generation and propagation. The mechanism of interaction between the ISW and SFT is revealed by elucidating the velocity fields around the SFT during the ISW propagation. The fluid mixing process between the two layers and the shape of the ISW profile are compared among different conditions. The forces induced by ISW on the SFT are calculated under various cases of ISW amplitude, SFT cross-sectional shape, relative distance of the SFT to the pycnocline, and fluid density ratio. The main conclusions are briefly summarized as follows:

- The maximum SFT forces in both horizontal and vertical directions and the thickness of the mixing layer increase with increasing ISW amplitude. Strong ISW-SFT interaction and severe energy dissipation can be found when the ISW amplitude is large.

- The most streamlined SFT cross section geometry (the parametric shape) experiences reduced flow separation and vortex shedding, as well as the minimum ISW-induced force, compared with the circular and elliptical shapes. Furthermore, the ISW-induced forces on the parametric cross section shape SFT are mainly caused by the pressure gradient, while vortex shedding contributes comparatively larger forces on the SFT with the circular shape.

- A clear enhancement of the vertical force on the SFT is shown for the relative distance of 10m compared with 40 m. The influence of the relative distance from the SFT to the pycnocline is crucial due to a complex combination of buoyancy, drag, and inertia force contributions. The buoyancy change induced by the ISW evolution can remarkably alter the vertical force and BWR of the SFT. It is imperative to simulate a prototype SFT under real ISW conditions including a complex flow field, strong interaction between the ISW and structure, and the structural buoyancy change.

- The ISW-induced forces on the SFT are proportional to the fluid density difference. The fluid mixing thickness at the interface increases with increasing fluid density ratio.

Nevertheless, it should be clarified that in the present study, the ISW-induced forces on the SFT are assumed to act uniformly and transverse to the tunnel tube as a worst-case scenario. Discrepancy in the dynamic response estimation can be induced by the two-dimensionality of hydrodynamic forces and by neglect of the impacts on the surrounding fluid field of structure deformation and movement. A related and practical hazard comes from ISW fissions into rank-ordered packets of internal solitons, which can propagate shoreward from the edge of the continental shelf; the impacts of internal wave packets on the SFT should be also be investigated in follow-on research.

REFERENCES

AASHTO (2018), *A Policy on Geometric Design of Highways and Streets.*

ANSYS, F. (2019), 'ANSYS fluent theory guide 19.1', *ANSYS, Canonsburg, PA* .

Cai, S., Long, X. & Gan, Z. (2003), 'A method to estimate the forces exerted by internal solitons on cylindrical piles', *Ocean Engineering* .

Cai, S., Long, X. & Wang, S. (2008), 'Forces and torques exerted by internal solitons in shear flows on cylindrical piles', *Applied Ocean Research* .

Cai, S., Wang, S. & Long, X. (2006), 'A simple estimation of the force exerted by internal solitons on cylindrical piles', *Ocean Engineering* .

Cavaliere, D., la Forgia, G., Adduce, C., Alpers, W., Martorelli, E. & Falcini, F. (2021), 'Breaking Location of Internal Solitary Waves Over a Sloping Seabed', *Journal of Geophysical Research: Oceans* **126**(2).

Chen, M., Chen, J. & You, Y. X. (2020), 'Forces on a semi-submersible in internal solitary waves with different propagation directions', *Ocean Engineering* .

Chen, M., Chen, K. & You, Y. X. (2017), 'Experimental investigation of internal solitary wave forces on a semi-submersible', *Ocean Engineering* .

Cui, J., Dong, S., Wang, Z., Han, X. & Yu, M. (2019), 'Experimental research on internal solitary waves interacting with moored floating structures', *Marine Structures* .

Deng, S., Ren, H., Xu, Y., Fu, S., Moan, T. & Gao, Z. (2020), 'Experimental study of vortex-induced vibration of a twin-tube submerged floating tunnel segment model', *Journal of Fluids and Structures* .

Ding, W., Ai, C., Jin, S. & Lin, J. (2020), 'Numerical investigation of an internal solitary wave interaction with horizontal cylinders', *Ocean Engineering* .

Ermanyuk, E. V. & Gavrilov, N. V. (2005), 'Experimental study of the dynamic effect of an internal solitary wave on a submerged circular cylinder', *Journal of Applied Mechanics and Technical Physics* .

Gang, L., Xiao-jun, Z. & Jian-xun, C. (2018), 'The Dynamic Response of an Experimental Floating Tunnel with Different Cross Sections under Explosive Impact', *Journal of Coastal Research* .

Haibin, L., Xie, J., Xu, J., Chen, Z., Liu, T. & Cai, S. (2016), 'Force and torque exerted by internal solitary waves in background parabolic current on cylindrical tendon leg by numerical simulation', *Ocean Engineering* .

Hibiya, T. (1986), 'Generation mechanism of internal waves by tidal flow over a sill', *Journal of Geophysical Research* .

Hirt, C. W. & Nichols, B. D. (1981), 'Volume of fluid (VOF) method for the dynamics of free boundaries', *Journal of Computational Physics* .

Hsu, T. W., Hsieh, C. M. & Hwang, R. R. (2004), 'Using RANS to simulate vortex generation and dissipation around impermeable submerged double breakwaters', *Coastal Engineering* **51**(7).

Jin, C. & Kim, M. H. (2020), 'Tunnel-mooring-train coupled dynamic analysis for submerged floating tunnel under wave excitations', *Applied Ocean Research* .

Kakutani, T. & Yamasaki, N. (1978), 'Solitary Waves on a Two-Layer Fluid', *Journal of the Physical Society of Japan* .

Klymak, J. M., Pinkel, R., Liu, C. T., Liu, A. K. & David, L. (2006), 'Prototypical solitons in the South China Sea', *Geophysical Research Letters* .

Koop, C. G. & Butler, G. (1981), 'An investigation of internal solitary waves in a two-fluid system', *Journal of Fluid Mechanics* .

Kristoffersen, M., Minoretti, A. & Børvik, T. (2019), 'On the internal blast loading of submerged floating tunnels in concrete with circular and rectangular cross-sections', *Engineering Failure Analysis* .

Kuzmin, D., Mierka, O. & Turek, S. (2007), 'On the implementation of the fr-fturbulence model in incompressible flow solvers based on a finite element discretisation', *International Journal of Computing Science and Mathematics* .

Li, K. & Jiang, X. (2016), Research on Section Form of Submerged Floating Tunnels Considering Structural Internal Force Optimization under Fluid Action, *in* 'Procedia Engineering'.

Lin, H., Xiang, Y. & Yang, Y. (2019), 'Vehicle-tunnel coupled vibration analysis of submerged floating tunnel due to tether parametric excitation', *Marine Structures* .

Lin, Z. & Zan, X. (2021), ‘Numerical study on load characteristics by internal solitary wave on cylinder sections at different depth and its parameterization’, *Ocean Engineering* .

ling Wang, L., Xu, J., Wang, Y., Wei, G., Lin, C. & Zhu, H. (2018), ‘Reduction of internal-solitary-wave-induced forces on a circular cylinder with a splitter plate’, *Journal of Fluids and Structures* .

Liu, S., He, G., Wang, Z., Luan, Z., Zhang, Z., Wang, W. & Gao, Y. (2020), ‘Resistance and flow field of a submarine in a density stratified fluid’, *Ocean Engineering* **217**.

Mandara, A., Russo, E., Faggiano, B. & Mazzolani, F. M. (2016), Analysis of Fluid-structure Interaction for a Submerged Floating Tunnel, *in* ‘Procedia Engineering’.

Michallet, H. & Barthélémy, E. (1998), ‘Experimental study of interfacial solitary waves’, *Journal of Fluid Mechanics* .

Miquel, A. M., Kamath, A., Chella, M. A., Archetti, R. & Bihs, H. (2018), ‘Analysis of different methods for wave generation and absorption in a CFD-based numerical wave tank’, *Journal of Marine Science and Engineering* .

Muhammad, N., Ullah, Z. & Choi, D. H. (2017), ‘Performance evaluation of submerged floating tunnel subjected to hydrodynamic and seismic excitations’, *Applied Sciences (Switzerland)* .

Ramirez, C. & Renouard, D. (1998), ‘Generation of internal waves over a shelf’, *Dynamics of Atmospheres and Oceans* .

Si, Z., Zhang, Y. & Fan, Z. (2012), ‘A numerical simulation of shear forces and torques exerted by large-amplitude internal solitary waves on a rigid pile in South China Sea’, *Applied Ocean Research* .

Song, Z. J., Teng, B., Gou, Y., Lu, L., Shi, Z. M., Xiao, Y. & Qu, Y. (2011), ‘Comparisons of internal solitary wave and surface wave actions on marine structures and their responses’, *Applied Ocean Research* .

Vázquez, A., Bruno, M., Izquierdo, A., Macías, D. & Ruiz-Cañavate, A. (2008), ‘Meteorologically forced subinertial flows and internal wave generation at the main sill of the Strait of Gibraltar’, *Deep-Sea Research Part I: Oceanographic Research Papers* .

Xu, Z., Yin, B., Hou, Y., Fan, Z. & Liu, A. K. (2010), ‘A study of internal solitary waves observed on the continental shelf in the northwestern South China Sea’, *Acta Oceanologica Sinica* .

Yan, H., Zhang, F. & Yu, J. (2016), The Lectotype Optimization Study on Submerged Floating Tunnel Based Delphi Method, *in* ‘Procedia Engineering’.

Zhu, H., Wang, L., Avital, E. J., Tang, H. & Williams, J. J. (2016), ‘Numerical simulation of interaction between internal solitary waves and submerged ridges’, *Applied Ocean Research* **58**.

Zou, P., Bricker, J. D. & Uijttewaal, W. (2021*a*), ‘The impacts of internal solitary waves on a submerged floating tunnel’, *Ocean Engineering* **238**, 109762.

Zou, P., Bricker, J. D. & Uijttewaal, W. (2021*b*), ‘Submerged floating tunnel cross-section analysis using a transition turbulence model’, *Journal of Hydraulic Research* pp. 1–13.

Zou, P., Bricker, J. & Uijttewaal, W. (2020), ‘Optimization of submerged floating tunnel cross section based on parametric Bézier curves and hybrid backpropagation - genetic algorithm’, *Marine Structures* .

4

IMPACTS OF EXTREME HYDRAULIC EVENTS

To evaluate the hydrodynamic loads of the SFT in this hazardous zone subject to severe tsunami and typhoon impacts, the Delft3D-FLOW hydrodynamic model and SWAN wave model are coupled, and a Computational Fluid Dynamics (CFD) method is adopted. The maximum probable tsunami and typhoon Rammasun (July 2014) are selected as hazard assessment conditions in the Qiongzhou Strait. Whether the tsunami and hindcast storm surge cause extreme forcing and bring challenges to the SFT engineering design, operation, and maintenance in the Qiongzhou Strait are discussed in this chapter. In order to determine the optimal SFT cross-section under extreme events, parametric shape in Chapter 2 is applied and compared with two simpler shapes including circular and elliptical cross sections. In-line force and lift are respectively applied to evaluate the SFT's hydrodynamic behaviour. The hydrodynamic loads acting on the SFT assessed in the present chapter is adopted for dynamic response research in Chapter 5. The highlights of this chapter are:

- *Extreme disasters including mega tsunamis and severe storm surges are assessed in the Qiongzhou Strait*
- *An integrated large-scale atmosphere-ocean modelling combined with CFD method framework is established for submerged floating tunnel hydrodynamic forcing evaluation*
- *The parametric shape shows preferable property under extreme hydraulic events compared with the simpler shapes*
- *The typhoon impacts are more devastating than tsunami for the submerged floating tunnel in the Qiongzhou Strait*

This chapter has been published as: Zou, P. X., Bricker, J. D., Uijttewaal, W. S. (2020). Impacts of extreme events on hydrodynamic characteristics of a submerged floating tunnel. ***Ocean Engineering***, 218, 108221.

4.1. INTRODUCTION

A potential SFT construction site, the Qiongzhou Strait (Fig.4.1), located between Hainan Island and Leizhou Peninsula (Guangdong) in the South China Sea (SCS), is subject to extreme events (Zhang et al. 2010, Yan et al. 2016, Jiang et al. 2018). The SFT is at risk of damage due to current and wave actions, internal flooding and submergence. Extreme hydraulic events further exacerbate the structural vulnerability.

The Qiongzhou Strait is located approximately 1000 km away from the Manila Trench, and is conceivably threatened by a Manila Trench tsunami. The Manila Trench and the north fault system are identified as being the most likely sources to generate mega submarine earthquake-tsunamis in the SCS and adjacent areas (Michel et al. 2001). Research about earthquake-tsunami generation along the Manila Trench has been conducted over the past two decades. Wu and Huang (Wu & Huang 2009) generated a hypothetical tsunami scenario from the Manila Trench and performed tsunami run-up and inundation simulations around Taiwan. Liu et al. (Liu et al. 2009) discussed the characteristics of tsunamis generated by earthquakes along the Manila subduction zone and proposed an early warning system for the SCS region. Nguyen et al. (Hong Nguyen et al. 2014) assessed the impact of a Manila Trench tsunami on the Vietnamese coast using the COMCOT model. Zhao et al. (Zhao et al. 2017) discussed a range of potential tsunami source magnitudes in the Manila Trench and analysed the tsunami impacts near Haikou. Ren and Liu (Ren & Liu 2015) investigated the potential extreme hazard of the Manila Trench, and the impacts on Hainan Island, Taiwan Island, and Lingding Bay. As one of the most devastating natural coastal disasters, tsunamis frequently occur and caused approximately 250,000 casualties and US$280 billion in economic losses during the past twenty years. Devastating tsunami damages, characterized by human fatalities and infrastructure failures, have increased over the previous two decades (Imamura et al. 2019, Bernard & Titov 2015). Thus, assessing large-scale tsunami impact in the Qiongzhou Strait is important for hazard mitigation, and tsunami warning capacity improvement is needed for intensive growth of infrastructure and critical engineering facilities such as an SFT in this region.

Storm surges are also catastrophic natural disasters for marine and coastal zones. Storm surge is an abnormal sea level rise driven by physical mechanisms including the inverse barometer (pressure) effect setup, wind-induced setup and breaking-wave setup (Bricker & Nakayama 2014). The Northwest Pacific basin holds the highest tropical storm surge frequency and intensity occurrence in the world with approximately 26.9 events annually. Guangdong and Hainan, where the Qiongzhou Strait is located, are particularly vulnerable to catastrophic typhoon strikes (biu Liu et al. 2001). Moreover, the frequency of tropical storm surges and coastal floods in the coastal areas of China over the past 65 years has risen significantly. Amongst the coastal provinces, Guangdong suffered the most storm surge events, while Hainan ranked fourth for storm surge frequency (Shi et al. 2015). The losses caused by storm surges accounted for over 75% of total economic losses, an annual average of more than CNY 3.9 billion in these tropical coastal provinces (Megawati et al. 2009). However, little is known about the effects of cross-oceanic tsunami and typhoon-related strait hydrodynamics on the SFT. Risk and vulnerability assessment due to tsunami and typhoon hazards on an SFT in this region had not yet been conducted.

In this chapter, the worst-case tsunami scenario along the Manila Trench and super typhoon Rammasun (2014) are selected as the extreme scenarios. To better understand hydrodynamic performance of the SFT under the tsunami and storm surge, we ask (1) how to determine the typical wave and current input conditions for the SFT analysis under these extreme cases, (2) which SFT cross-section shape is favourable and should be adopted for locations subject to extreme events, and (3) what is the effect of storm surge and tsunami on an SFT? To address these questions, first, descriptions of the selected scenarios and potential SFT application sites are depicted in section 4.2, and the modelling methods are then expanded in section 4.3. In section 4.4, tsunami and storm surge model validations are conducted. Finally, the wave and current characteristics induced by extreme events at the optimal SFT construction location in the Qiongzhou Strait are addressed in section 4.5, along with detailed discussions about the optimal SFT cross-section geometry and hydrodynamic characteristics.

4.2. DESCRIPTION OF SELECTED EXTREME EVENTS AND ANALYSIS LOCATION

4.2.1. TSUNAMI GENERATED IN THE MANILA TRENCH

The largest historical tsunamigenic earthquake in the Manila Trench (Wu & Huang 2009) was simulated as six fault segments acting as one long earthquake source in this study. The worst-case Manila Trench source parameters used in our model are proposed by Nguyen et al. (Hong Nguyen et al. 2014), which modifies Wu and Huang 's (Wu & Huang 2009) model with more precise fault width values by an interpolation method (Megawati et al. 2009). Table 4.1 shows the hypothetical fault parameters along the Manila Trench source applied in this study, with epicenters set at the midpoint of each segment. The earthquake magnitude is 9.3.

Table 4.1: Fault Parameters of the Manila Trench

Fault	Long.	Lat.	Length (km)	Width (km)	Dislocation (m)	Depth (km)	Strike (°)	Dip (°)	Rake (°)
E1	120.5	20.2	190	120	25	30	354	10	90
E2	119.8	18.7	250	160	40	30	22	20	90
E3	119.3	17	220	160	40	30	2	28	90
E4	119.2	15.1	170	90	28	30	356	20	90
E5	119.6	13.7	140	110	12	30	344	22	90
E6	120.5	12.9	95	80	5	30	331	26	90

4.2.2. TYPHOON RAMMASUN

As the most powerful and strongest typhoon to make landfall on Hainan Island since 1949, super typhoon Rammasun (2014) is selected as an extreme event for hydrodynamic assessment of the SFT. Rammasun made first landfall on Wenchang, Hainan at 7:00 UTC on July 18, 2014 with a maximum wind speed of 60 m/s and a minimum pressure of 910 hPa. After that, Rammasun retained super typhoon intensity while crossing the Qiongzhou Strait and moving north-westward. It weakened when it entered Beibu Gulf, and dissipated when it made its second landfall in Guangxi province on July 19.

Rammasun is the most devastating typhoon that affected Hainan Island since 1949. It affected 3.26 million people, collapsed 23,160 residences, and caused direct economic losses of CNY 11.95 billion in Hainan (Haikou Meteorological Service n.d.). The track (Fig.4.1) and intensity data are obtained from the China Meteorological Administration tropical cyclone database (Data n.d.).

Figure 4.1: Typhoon Rammasun track

4.2.3. OPTIMAL SUBMERGED FLOATING TUNNEL HEADING

Yan et al. (Yan et al. 2016) and Shengzhong et al. (Shengzhong et al. 2016) compared seven possible sea-crossing locations in the Qiongzhou Strait, considering submarine geomorphological features, structure reliability, and economy. “Line V” (from Sitang in Leizhou Peninsula to Tianwei in Haikou), shown in Fig.4.2, was recommended as the optimal SFT construction heading. It is selected for SFT hydrodynamic analysis under the tsunami and storm surge impacts in this study. Seven virtual gauges are set uniformly along this optimal heading to obtain the hydrodynamic conditions in the strait during the simulated events. The coordinate of each virtual gauge is listed in Table 4.2.

Table 4.2: Coordinates of virtual gauges

	Latitude (°N)	Longitude (°E)
Gauge #1	20.084	110.168
Gauge #2	20.108	110.166
Gauge #3	20.132	110.164
Gauge #4	20.156	110.162
Gauge #5	20.180	110.160
Gauge #6	20.204	110.158
Gauge #7	20.252	110.154

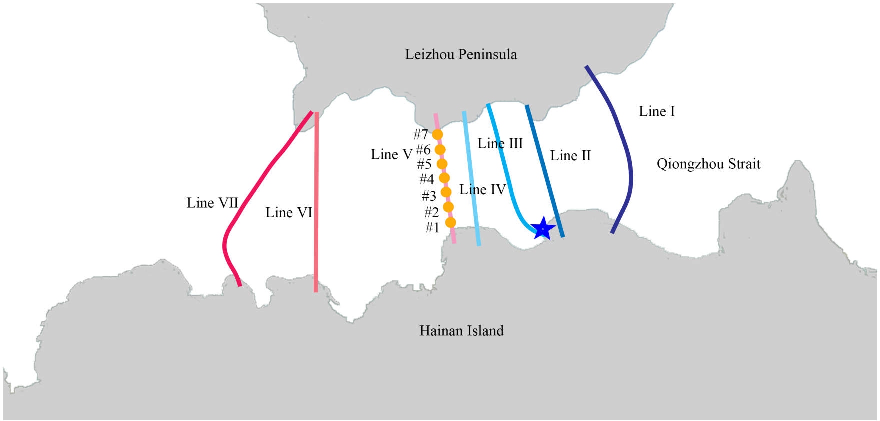

Figure 4.2: The seven alternative headings for sea-crossing in the Qiongzhou Strait and the virtual gauge locations (yellow circles) along "Line V". The blue star denotes the observation station at Xiuying (110.34°E, 20.05°N) used for model validation

4.3. METHODOLOGY

4.3.1. MODEL DESCRIPTION

The numerical hydrodynamic modelling system Delft3D-FLOW is applied to perform both the tsunami and storm surge simulations. It solves the unsteady, non-linear shallow water equations. Delft3D-FLOW is a widely-used prediction tool for tsunami events, tidal flows and wind-pressure fields (Yin et al. 2020, Roeber & Bricker 2015). For tsunami simulation, the seafloor deformation of a tsunami-generating earthquake can be computed by the Okada model derived from a Green's function solution to the elastic half space problem (Okada 1992). The static deformation of the seafloor after the oceanic earthquake is then estimated as an initial free-surface profile. The initial water level of the Manila Trench tsunami is shown in Fig.4.3.

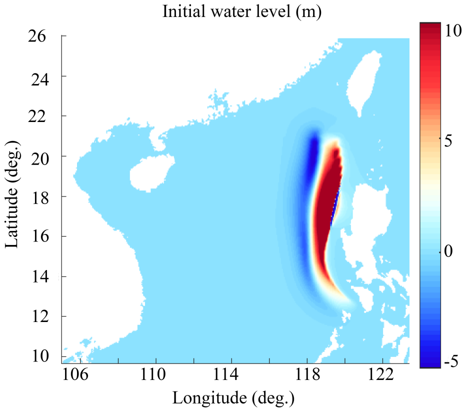

Figure 4.3: Initial water level profile along Manila Trench

The behaviour of typhoon Rammasun is hindcast with track data (Data n.d.) spatialized into wind and pressure fields by the Holland (Holland et al. 2010) parametric hurricane method, which improves the Holland (Holland 1980) parametric approach by applying wind-pressure parameters readily available from hurricane archives. Empirical relations for central pressure and maximum wind speed are devised by Holland (Holland 2008). The wind field is asymmetric due to the inflow angle caused by friction. Here, a constant angle of 25° is applied (Wankang et al. 2019). A wind conversion factor of 0.93 is adopted. The radius of maximum winds R_m is expressed per Gross et al. (Gross et al. 2004) in Eq.4.1.

$$R_m = 35.37 - 0.111 V_m + 0.570(\Phi - 25) \tag{4.1}$$

where V_m is the maximum wind speed and Φ is latitude.

An integrated atmosphere-ocean storm surge modelling framework is established for SFT hydrodynamic forcing evaluation. The typhoon Rammasun wind-pressure fields drive a Delft3D-FLOW hydrodynamic model and SWAN wave model. In order to account for wave-current interaction and radiation stresses, online coupling of SWAN with Delft3D-FLOW is activated. The air-sea drag coefficient is 0.003, and a Manning's n of 0.025 $\mathrm{sm}^{-1/3}$ is used for bottom stress. Open boundaries use a water level prescribed by the Global Inverse Tide Model TPXO 7.2 (TPXO n.d.) (M2, S2, N2, K2, K1,O1, P1, Q1, MF, MM, SSA components) with the “pavbnd” command to prevent instability when interacting with meteorological forcing (Caldwell & Edmonds 2014). The bathymetry data is taken from the General Bathymetric Chart of the Oceans (GEBCO n.d.).

In this study, large-scale tsunami and typhoon models are established respectively to analyze depth-averaged flow characteristics in the Qiongzhou Strait (Zou et al. 2020*a*). The in-line component of the current and wave loads at planes perpendicular to the optimal SFT heading line (“Line V”) are emphasized in the evaluation of the SFT cross-section forcing.

4.3.2. MODEL CONFIGURATION

The geographic extent of the model domain ranges from 105°E, 26°N to 126°E, 10°N. Three nested grids, referred to as Grid 1, Grid 2, and Grid 3, are adopted with spherical coordinates. The finest grid covers the Qiongzhou Strait to obtain the flow and wave conditions (Fig.4.4). Detailed grid information is shown in Table 4.3. A 0.5 s computational time step for a duration of 12 h is applied in the tsunami simulation. In the storm surge simulation, a 1 s computational time step is selected for the storm surge model, which is coupled with a stationary SWAN wave simulation every 60 min. Wind-stress and tidal forcing are added to run the simulation from 0:00 on July 14 to 0:00 on July 20.

4.3.3. FORCES ON THE SUBMERGED FLOATING TUNNEL

The CFD code ANSYS FLUENT v19.1 is applied to conduct field-scale simulations of the SFT by solving the RANS equations using a finite-volume discretization scheme. Considering the different hydrodynamic performance of the SFT under tsunami and typhoon impacts, the computational domain is different for each case.

Table 4.3: Three-level grid parameters

Level	Grid 1	Grid 2	Grid 3
Grid resolution (degree)	0.05	0.01	0.002
Central Point	115.5°E, 18°N	110.2°E, 19.7°N	110.2°E, 20.15°N
Number of cells in longitude direction	420	520	2200
Number of cells in latitude direction	320	580	350

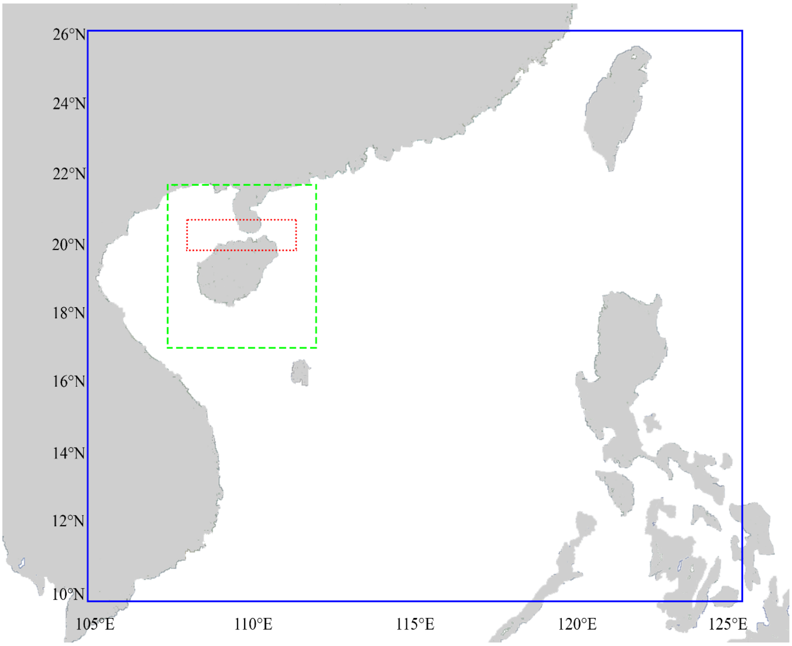

Figure 4.4: Computational domain and nested grids

GOVERNING EQUATIONS

The tsunami affects the SFT by generating strong currents. Strong acceleration of these currents causes the SFT boundary layer to alternate between laminar and turbulent flow, and inertial forces on the SFT are significant. To resolve these processes, a transient simulation is conducted with the transition SST (shear stress transport) turbulence model, which has been validated to accurately predict the laminar to turbulent transition process (Zou et al. 2021*b*). Previous studies show the reliability of this turbulence model at both low and high Reynolds numbers (Wauters & Degroote 2018, Pawar & Brizzolara 2019, Xu et al. 2018). The transition SST model is based on coupling of the SST $k-\omega$ transport equations with the intermittency and momentum-thickness Reynolds number transport equations for the transition onset criterion. The intermittency factor used to describe transition development is computed by additional transport equations in the form of Eq.2.17 in Chapter 2.

For the storm surge case, however, strong flow acceleration is not observed in the Qiongzhou Strait as per section 4.5.2. Hence, the inertial force of the SFT can be neglected. In order to achieve a conservative hydrodynamic force evaluation for the SFT, a worst case scenario of the maximum current velocity and wave height is applied at the numerical inlet. The Reynolds number of the SFT cross-section is on the order of 10^7. Therefore, a fully-turbulent model can be used. The RNG $k-\epsilon$ model is applied at high Reynolds numbers, and is more accurate and reliable for a wider class of flows than the standard $k-\epsilon$ model (Jeong et al. 2002). It more accurately simulates blunt geometry and flow separation with an additional term in the ϵ equation and an analytical formula for the turbulent Prandtl number. The RNG $k-\epsilon$ model transport equation can be expressed as Eqs.2.6, 2.7, and 2.8 in Chapter2. The volume-of-fluid (VOF) method (Hirt & Nichols 1981) is adopted to track the air-water interface. Fifth-order Stokes wave theory (Fenton 1985) is used for nonlinear wave generation at the inlet open channel wave boundary. The generalized expression for fifth-order Stokes waves is given by Eqs.4.2 and 4.3.

$$\zeta(X,t) = \frac{1}{k}\sum_{i=1}^{5}\sum_{j=1}^{i} b_{ij}(ka)^2\cos(j\alpha) \tag{4.2}$$

$$\alpha = k_x x + k_y y - \omega_e t + \epsilon \tag{4.3}$$

The generalized expression for the associated velocity potential is defined as Eq. 4.4.

$$\Phi(X,t) = \frac{1}{k}(\frac{g}{k}\tanh(kH))^{\frac{1}{2}}\sum_{i=1}^{5}(ka)^i\sum_{j=1}^{i} a_{ij}\cosh[jk(z+H)]\cos(j\alpha) \tag{4.4}$$

Velocity components for surface gravity waves are shown in Eq.4.5.

$$\begin{cases} u = \frac{\partial\Phi}{\partial x}\cos\theta \\ v = \frac{\partial\Phi}{\partial x}\sin\theta \end{cases} \tag{4.5}$$

The wave frequency ω is given by Eq.4.6

$$\omega = [gk\tanh(kH)]^{\frac{1}{2}}[1 + c_3(ka)^2 + c_5(ka)^4] \tag{4.6}$$

where ω_e is effective wave frequency; t is time; k is wave number; H is water depth; g is the gravity magnitude; a_{ij}, b_{ij}, c_i are the complex expressions of kH; a is wave amplitude; θ is the wave heading angle.

COMPUTATIONAL DOMAINS

A parametric method using Machine Learning to predict the optimal SFT cross-section shape for improving the hydrodynamic performance was presented in Chapter 2(Zou et al. 2020*b*), where the objective is to minimize the hydrodynamic forces (time-averaged drag and root mean square lift) on the SFT. The parametric shape has been compared with the simpler circular and elliptical shapes under internal solitary waves in Chapter 3(Zou et al. 2021*a*). In the current study, parametric, circular, and elliptical shapes for the SFT cross-section with equal clearance (5 m × 11 m), applied in previous research, are compared under extreme events.

For the tsunami, a time series of flow speed during the 12 h tsunami simulation period is applied at the inlet boundary. A transient analysis with a symmetrical (in the vertical) computational domain is adopted. The computational domain is 400 m in length and 100 m in height (Fig.4.5(a)). The distances from the inlet and outlet boundaries to the SFT cross-section center are 100 m and 300 m, respectively. A zero-reference pressure and zero-gradient condition for velocity are employed at the pressure-outlet boundary. A no-slip, hydraulically smooth wall condition is applied to the SFT cross-section surface. For the upper and lower boundaries, symmetry (free-slip) is used to avoid wall effects. Multiple grid sizes were used to evaluate grid independence in (Zou et al. 2020*b*). The computational domain comprises three regions as illustrated in Fig.4.5(a). The first region: a high-quality unstructured mesh is generated around the SFT cross-section, and an inflation tool is used to generate 40 layers of quadrangular cells covering the boundary layer of the SFT surface. The first grid layer cell size normal to the SFT cross-section surface is 3×10^{-5} m with a growth rate of 1.2, resulting in Y^+ around 1 (Fig.4.5(c)). The cell size parallel to the surface is 0.01 m. The second region: the 4 zones around the first region have a grid resolution of 0.5 m. The third region: a structured mesh with a grid resolution of 1 m is applied in the rest of the domain. The total number of cells in this model is about 300,000. The PISO (Pressure-Implicit with Splitting of Operators) algorithm is used for pressure-velocity coupling. The CFD simulation runs for the full tsunami generation and propagation process of 12h. A high-performance computing (HPC) cluster is used to run parallel computation tasks.

4

Since wind-induced wave effects need to be considered in the storm surge case, a numerical open channel wave flume is established. The computational domain is 400 m in length and 140 m in height, allowing 9 wavelengths to propagate in the numerical flume (Fig.4.5(b)). The water depth is 100 m based on the topography of the optimal SFT heading in the Qiongzhou Strait. The height of the air phase is 40 m. The SFT is submerged at a depth of generally 30~50 m below the free surface as per the feasibility studies and relevant research to date with the consideration of reducing surface wave impacts and meeting navigation requirements (il Seo et al. 2015, Kunisu 2010). Herein, an SFT submergence depth of 40 m is adopted. From section 4.5.2, the maximum current acceleration is below $8 \times 10^{-5}\,\mathrm{m\,s^{-2}}$ during the storm surge simulation, indicating the inertial force (due to storm-surge-induced current) acting on the SFT can be neglected. In order to simulate the most unfavorable condition, a combined steady current and wave condition is applied. From the results of section 4.5.2, an open channel wave boundary condition with wave height = 4.8 m and wave length $L = 45$ m, coupled with a mean current speed of $1.65\,\mathrm{m\,s^{-1}}$ are specified at the inlet boundary. 5^{th} order Stokes wave theory with an Ursell number of 0.0097 is applied to depict the wave profile. The wave and current propagate in the same direction (left to right). Zero-reference pressure is employed at the open channel pressure outlet and the top boundary in the air region to avoid back flow into the domain. A hydraulically smooth no-slip wall condition is applied on the SFT cross-section surface and at the bottom boundary. The grid is almost the same as tsunami case except for two differences:

1) Since the Reynolds number in the storm surge study is higher than the tsunami case, and each case uses a different turbulence model, in order to meet the required Y^+, the first grid layer length normal to the SFT cross-section surface is 1×10^{-3} m.

2) A fine grid near the free surface and higher order discretization are applied to reduce numerical dissipation of waves. The grid resolution near the free surface covers 100 nodes per wave height and 45 nodes per wave length. This local refinement sufficiently captures the wave profile as per previous studies (Tian et al. 2019, Li & Zhang 2019). The total number of cells in this model is 473,252 after mesh refinement. A 400 s simulation is performed, and the last 100 s of data, in which the force oscillation is stable, is used for force analysis.

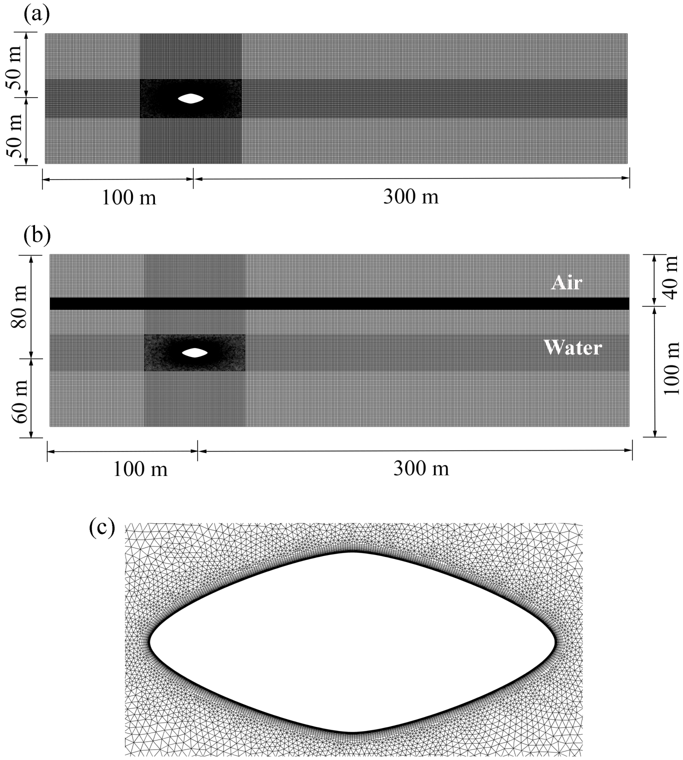

Figure 4.5: Schematic of meshes used. a) Computational domain for tsunami simulation. b) Computational domain for storm surge simulation. c) Detailed mesh around the SFT

4.4. Model Validation

4.4.1. Tsunami Case

Modelled surface elevations at several locations from Ren and Liu (Ren & Liu 2015) are used to validate our results. Fig.4.6 shows our simulated tsunami surface levels and phases are in close agreement with Ren and Liu (Ren & Liu 2015)'s model in general. Mesh precision differences and steep topography near the coastal regions may cause slight deviation of the peak values at Sanya, KaoShiung, and Shantou. Fig.4.7 shows the

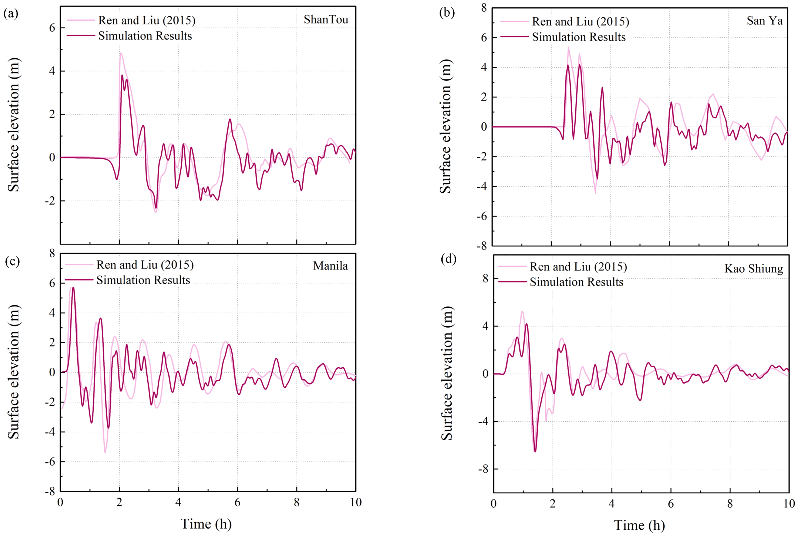

Figure 4.6: Time series of water levels at different locations. a)~d): temporal variation of surface elevation at Shantou, San Ya, Manila, and Kao Shiung, respectively

water level change during tsunami propagation near the Qiongzhou Strait. The tsunami wave first hits the south-eastern shore of Hainan Island at around 2 h, and thereafter refracts around Hainan Island into two separate parts: one propagates from north-eastern Hainan Island into the Qiongzhou Strait, and another bypasses south-western Hainan Island into the Beibu Gulf. The onset of tsunami waves in the Qiongzhou Strait appears at 4 h, and the confluence of the two waves occurs at 6.5 h near north-western Hainan Island. The arrival time and temporal variation of tsunami amplitude around the Qiongzhou Strait agree with Ren and Liu (Ren & Liu 2015), indicating the robustness and reliability of our results.

4.4.2. TYPHOON CASE

In order to verify our results, two simulations are carried out. One contains only astronomical tidal forcing, and the other is comprised of tidal forcing plus the meteorological forcing from the typhoon to compute the total storm tide elevations. Here, during typhoon Rammasun, the measured data of tidal station Xiuying (Fig.4.2), which is located in the Qiongzhou Strait, is utilised to validate model results. The model results of Wang et al. (Wang et al. 2017) are also used for comparison.

Fig.4.8(a) shows the validation results for astronomic tides at Xiuying (110.34°E, 20.05°N). Even though the simulated results show a positive bias of 16 cm at the maximum surface elevation, the astronomical tides are generally consistent with Wang et al. (Wang et al. 2017)'s model results and $t-tide$ harmonic analysis. The storm tide elevation during typhoon Rammasun in Xiuying is shown in Fig.4.8 (b). Typhoon Rammasun crossed over the Qiongzhou Strait during high tide. The maximum water elevation (storm tide) is almost 2 m above mean sea level. The peak storm tide is underestimated by 20 cm in our model, whereas Wang et al. (Wang et al. 2017)'s model underestimated observed data by approximately 40 cm. Both our model and (Wang et al. 2017) predicted the highest storm tide about 3 h earlier than observed. Since the best track data for the storm is reported at 6 hour intervals, the meteorological input data cannot be expected to produce a result more accurate than this, as the storm location and propagation speed is not constant during the 6 hours between reported track times. Therefore, our results show less discrepancy with observations than (Wang et al. 2017) does, indicating a reasonable and reliable storm surge simulation and confirming the capacity of the model.

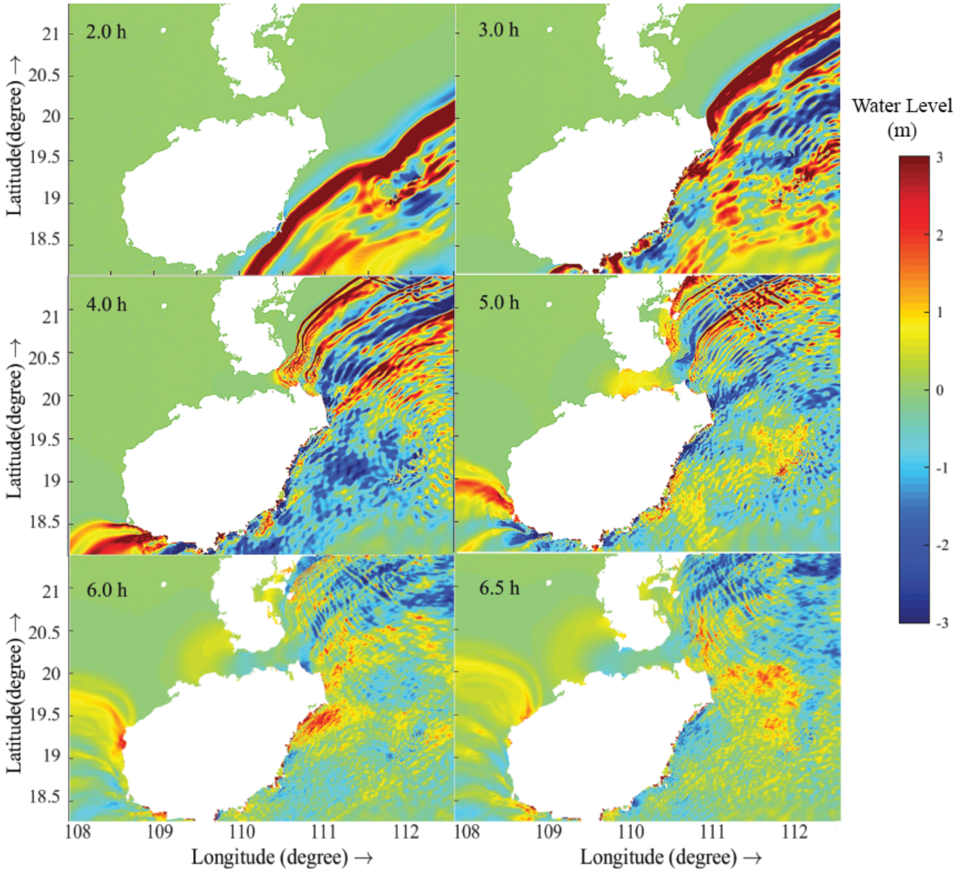

Figure 4.7: Tsunami propagation near the Qiongzhou Strait at different times

4.5. RESULTS AND DISCUSSION

4.5.1. TSUNAMI CHARACTERISTICS IN THE QIONGZHOU STRAIT

To investigate the tsunami characteristics in the Qiongzhou Strait, the maximum water elevation at each grid cell during the entire 12 h simulation is shown in Fig.4.9(a). Generally, water elevations decrease from the east at around 2 m to the west at less than 1 m in

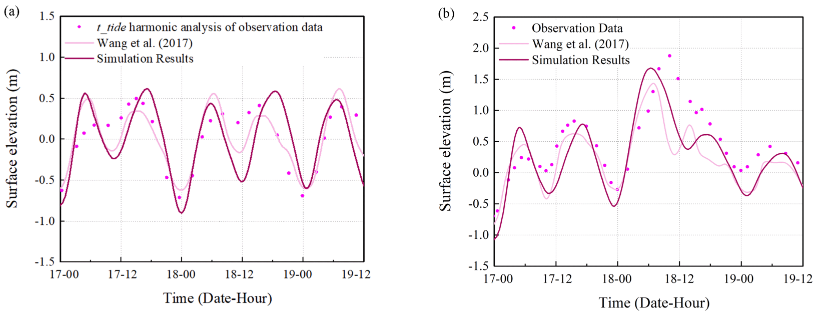

Figure 4.8: Time series of water levels at different locations. a) Astronomical tide validation. b) Storm tide validation. The water elevation is referenced to Mean Sea Level

the Qiongzhou Strait. Throughout the simulation, our results show that the Qiongzhou Strait is sheltered by Hainan Island, preventing the devastating inundation that could occur in Hainan, Guangdong, Taiwan, and Hong Kong (yuan Ren et al. 2017, Wu & Huang 2009).

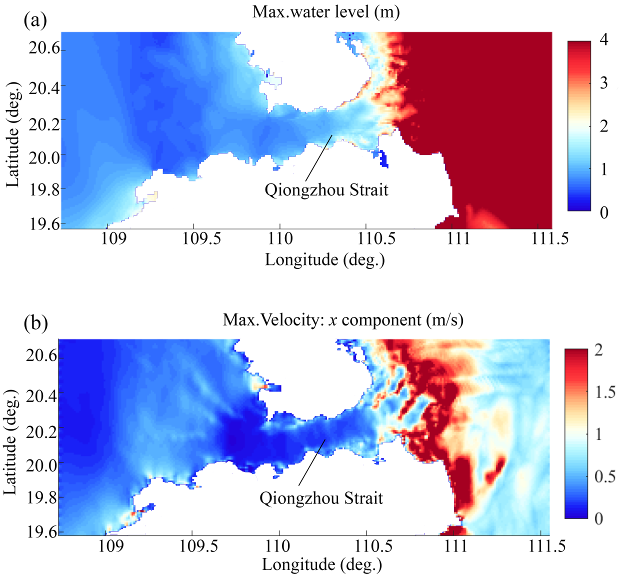

Figure 4.9: Hydraulic properties of the Manila Trench tsunami in the Qiongzhou Strait. a) Maximum water surface elevation. b) Maximum east-west current magnitude

Since the optimal SFT heading is generally transverse to the strait, the components of current speed and wave direction parallel to the strait heading are most relevant for evaluation of the SFT cross-section hydraulic performance. Fig.4.9(b) shows the maximum east-west current speed induced by the tsunami in the Qiongzhou Strait. In most of the Qiongzhou Strait, the current speed is less than 1 m/s. The current direction is generally east-west, moving between the Beibu Gulf and the northern SCS. Since the tsunami is unsteady, the time-varying current speed and inflow acceleration may change dramatically, and hence may cause large drag and inertial forces on the SFT compared with the local astronomical tide, jeopardizing the SFT structure and mooring system. To assess the effect of this east-west reversing tsunami current on the SFT, the current in the Qiongzhou Strait is extracted for the simulation of forces on the SFT.

Fig.4.10 (a) shows the depth-averaged along-strait current speed at the seven gauges (Fig.4.2) in the Qiongzhou Strait during the tsunami simulation. Note that it takes 4.2 h for the first tsunami wave to arrive at the SFT site. The first current peak occurs at 4.8 h, with a maximum speed of 0.6 m/s in the westward direction. However, the largest current speed occurs at around 11.3 h, flowing from west to east with a maximum speed of 0.9 m/s. Generally, gauge #7 records the most severe current speed variation, so is used for further SFT hydrodynamic analysis. Fig.4.10 (b) shows the current speed and flow acceleration at gauge # 7. It should be noted that the peak values of flow speed and acceleration do not occur simultaneously. The largest flow acceleration magnitude is $6 \times 10^{-4}\,\mathrm{m\,s^{-2}}$ in the westward direction at 4.5 h.

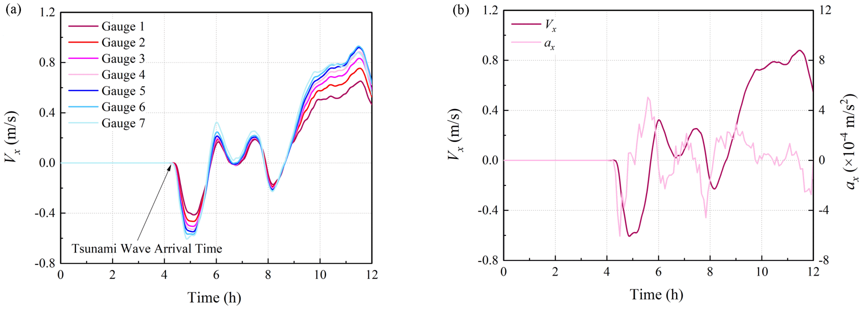

Figure 4.10: Tsunami characteristics in the Qiongzhou Strait. a) Current speed at the seven virtual gauges. b) Current speed and acceleration at virtual gauge #7. x direction: positive eastward and negative westward

4.5.2. STORM SURGE CHARACTERISTICS IN THE QIONGZHOU STRAIT

Fig.4.11 shows the spatial distribution of maximum water level (storm tide) in the Qiongzhou Strait during the typhoon simulation. Typhoon Rammasun passed over north eastern Hainan Island with a counterclockwise wind field. These effects were conductive to the sea water rising rapidly to the east of the Qiongzhou Strait and piling up along the coasts, especially near the Leizhou Peninsula and northeastern Hainan Island. The maximum water level on the eastern coast of the Leizhou Peninsula reached over 3 m. However, due to the sheltering effect of the Leizhou Peninsula and Hainan Island, and additionally the gradually weakened strength of Rammasun when it crossed over the Qiongzhou Strait, the maximum water elevation in the strait was less than 2 m, dropping rapidly to the west. The current speed and wave direction transverse to the SFT are extracted for hy-

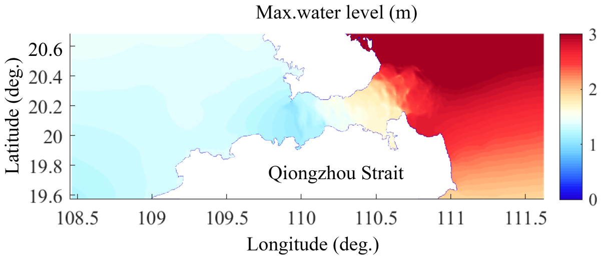

Figure 4.11: Maximum water level (storm tide) in the Qiongzhou Strait

draulic performance analysis. As illustrated in Fig.4.12 (a), the maximum absolute value of depth-averaged flow speed observed in gauge #3 in the x direction is 1.65 m/s westward. The peak value occurred at 6:00~9:00 on July 18 at different virtual flow gauges along the optimal SFT heading; this is consistent with the time of the peak storm tide level (Fig.4.8(b)). However, unlike the tsunami, the maximum current acceleration of the typhoon storm surge is below $8 \times 10^{-5}\,\mathrm{m\,s^{-2}}$, resulting in the drag force dominating the in-line forces of the SFT, with negligible inertia force. However, the vertical distribution of wind-driven flow is complex. In order to evaluate the SFT hydraulic forcing accurately, the current speed input to the inlet boundary of the CFD program should be carefully examined. Therefore, a three-dimensional Delft3D-FLOW hydrodynamic model with 10 uniform vertical sigma layers, forced by the same conditions as the two-dimensional typhoon Rammasun model above, is adopted and compared. Fig.4.12(c) shows the current speed in x direction at 40 m below the surface (the SFT submergence depth) is around 1.64 m/s, which is nearly equal to the 1.65 m/s depth-averaged flow speed from the two-dimensional model. Hence, using the depth-averaged current speed is sufficient for SFT force analysis.

Fig.4.13 shows the typhoon-induced wind velocity magnitude fields superimposed on wind speed vectors. The SFT cross section is affected by wave-induced orbital velocities normal to the tunnel tube, rather than the component parallel to the tunnel. To obtain the component of the wave-induced orbital velocity vector normal to the tube, the orbital velocity vector is multiplied by the sine of the angle between the velocity vector and the SFT heading. Since orbital velocities are proportional to the wave height, we determine the wave height using the corresponding x-component of the orbital velocities.The wave height at the seven virtual wave gauges on the optimal SFT heading is illustrated in Fig 4.12(b). At 10:00 on July 18, the typhoon eye entered the strait accompanied by low wind speed, resulting in low wave height in the Qiongzhou strait. As typhoon Rammasun moved northwestward at 14:00 on July 18, the wind speed in the strait dramatically increased. The maximum wind speed at gauge #3 (110.164°E, 20.132°N) increased to around 30 m/s, and westerly wind dominated the strait, thus the wave height increased . The wave height reached its maximum value of 4.8 m, with a corresponding wave period of 5.08 s. The sheltering effect of Hainan Island reduces the wave height and wave period in the strait compared to the open sea. After the typhoon crossed over the strait, entered Beibu Gulf and made landfall in Guangxi Province, the wind intensity and wave height continuously decreased.

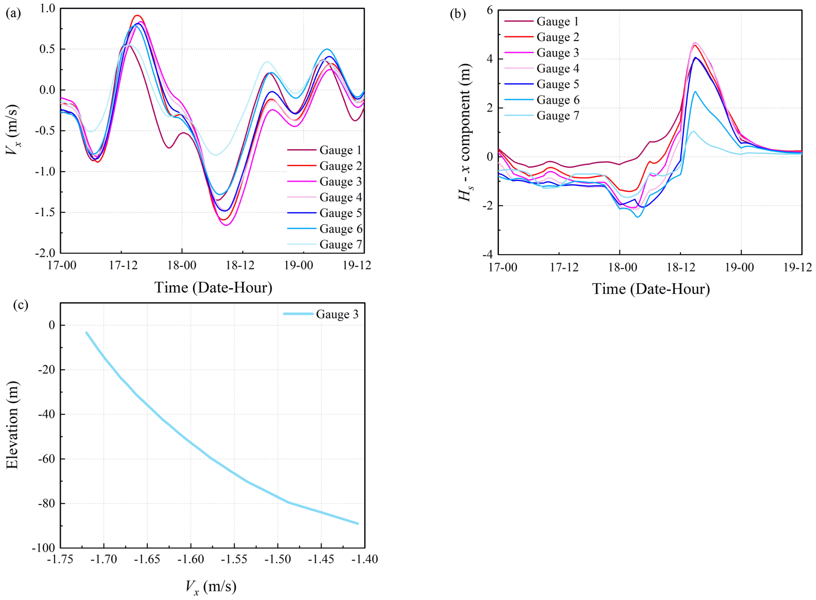

Figure 4.12: Storm tide in the Qiongzhou Strait. a) Along-strait depth-averaged current speed at the seven virtual gauges. b) Along-strait wave height at the seven virtual gauges. c) Vertical distribution of current speed when gauge #3 reached its maximum current speed value. x direction: positive to east and negative to west

4.5.3. TSUNAMI IMPACTS ON THE SFT

Fig.4.14(a) shows the temporal variation of in-line force (combined drag and inertial force) during the tsunami simulation with different SFT cross-sections. The maximum in-line force on all cross sectional shapes occurs at around 11.3 h, which is the same time as the peak inlet current speed (Fig.4.10(b)). For the parametric Bezier curve shape, the maximum in-line force is 200 N/m, which is half that of the elliptical SFT cross-section. However, the circular cross section shape experiences a maximum in-line force of 1700 N/m, which is over 8 times the force on the parametric Bezier curve cross section. In addition to this, the times of peak in-line force are not the same for all shapes. For the parametric Bezier curve shape, the first negative and positive maxima of inline force occur at around 4.5 h and 5.5 h, respectively, which are almost identical to the times of local peaks in acceleration (Fig.4.10(b)), indicating dominance of the inertia force. However, for the circular cross section, the first negative and positive maxima of inline force occur at around 4.8 h and 6.0 h, respectively, (Fig 4.10(b)), indicating dominance of the drag force. The elliptical cross section displays a phase between the other two shapes. Therefore, the in-line force on the elliptical SFT is a combined effect of inertial and drag forces.

Fig.4.14(b) shows the lift force during the tsunami simulation for different SFT cross-

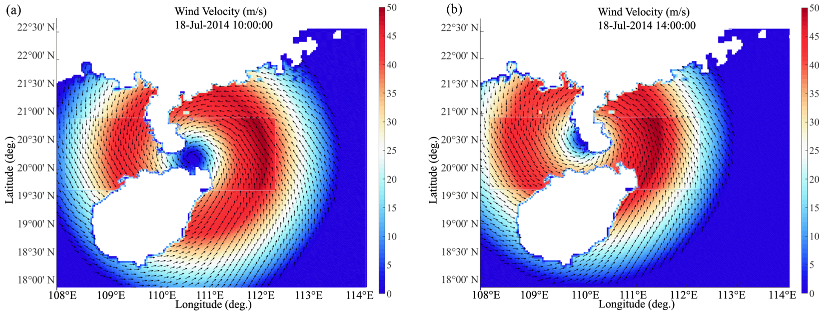

Figure 4.13: Wind velocity field near the Qingzhou Strait. a) wind velocity at 10:00 on July 18. b) wind velocity at 14:00 on July 18

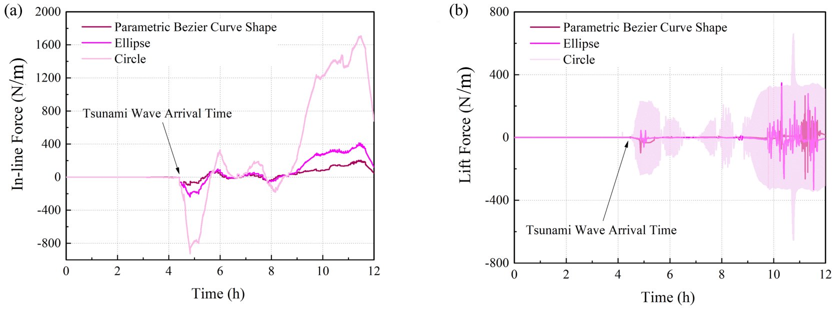

Figure 4.14: Hydrodynamic forces on the SFT. a) The in-line force on the SFT for different cross-sections. b) The lift force on the SFT for different cross-sections

sections. The results indicate that severe vortex shedding occurs at about 11 h for the parametric Bezier curve shape, while it shows vortex shedding beginning before 10 h for the ellipse. The circular cross section experiences a larger lift force than the other shapes and vortex shedding begins just after the tsunami reaches the SFT heading in the Qiongzhou Strait. It should also be noted that the vortex shedding frequency of the circular SFT is higher than that of the other two SFT cross-sections.

Fig.4.15 shows time-averaged velocity contours for the three different SFT cross-sections. The parametric Bezier curve profile (Fig.4.15(c)) is the most streamlined shape, with the furthest downstream separation point and the smallest wake region, thereby mitigating the in-line force on the SFT. This shape also experiences a maximum velocity lower than the other two cross-section shapes, resulting in a pressure more uniformly distributed along the SFT surface.

4.5.4. TYPHOON IMPACTS ON THE SFT

Section 4.5.3 shows that the parametric Bezier curve SFT cross-section has more favourable hydrodynamic performance than simpler shapes. Therefore, the parametric Bezier curve SFT cross-section is adopted for storm surge impact analysis. Fig.4.16(a) shows time se-

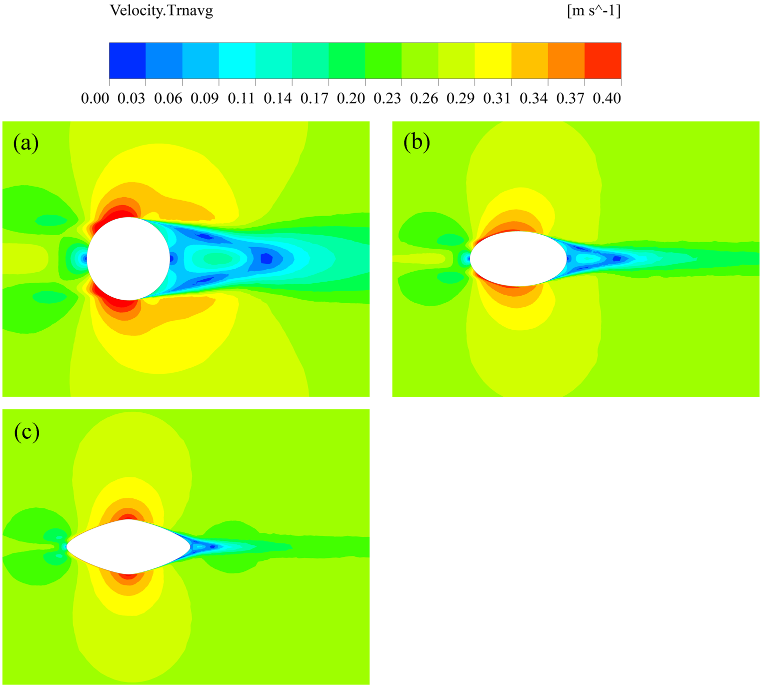

Figure 4.15: Time-averaged velocity contours of different cross sectional shapes. a) Circle. b) Ellipse. c) Parametric shape

ries of in-line force and lift force on the SFT in the typhoon scenario. The maximum in-line force on the SFT is approximately 2500 N/m, whereas maximum lift is 4000 N/m. The in-line force and lift have the same fluctuation period of about 4.3 s, driven by the combined wave and current forcing at the inlet of the ANSYS Fluent simulation. The in-line force lags behind the lift with a phase difference, as expected for orbital flow induced by progressive surface waves.

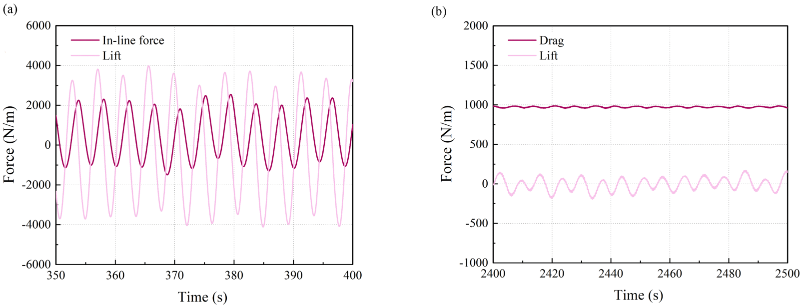

Figure 4.16: Typhoon forces on the SFT in the Qiongzhou Strait. a) Coupled wave-current model. b) Steady current only model

Fig.4.17 presents velocity contours around the SFT cross-section at $t = 400$ s. In the water phase, the velocity near the wave crest is high, whereas below the wave trough it is low. The velocity field is distorted near the SFT.

To better understand the differences of the wave and current impacts on the SFT, a simulation with only current (no wave) is conducted as a comparison. The mean current speed remains 1.65 m/s, the same as in the coupled wave-current model. The simulation ran for 2500 s, and time series of drag and lift during the final 100 s are shown in Fig.4.16(b). The maximum drag in this steady flow model is about 1000 N/m, half that of the wave-current case, indicating that waves and current contribute equally to the in-line force. However, the lift in the current-only model is below 250 N/m, indicating the waves play a dominant role in lift. The large velocity fluctuation at the wave period disrupts the uniform pressure distribution on the upper and lower SFT surfaces, resulting in an apparent increase of lift. In the current-only case, the drag and lift both fluctuate with a small amplitude at a period of about 6.8 s, which is longer than the fluctuation period in the coupled wave-current case.

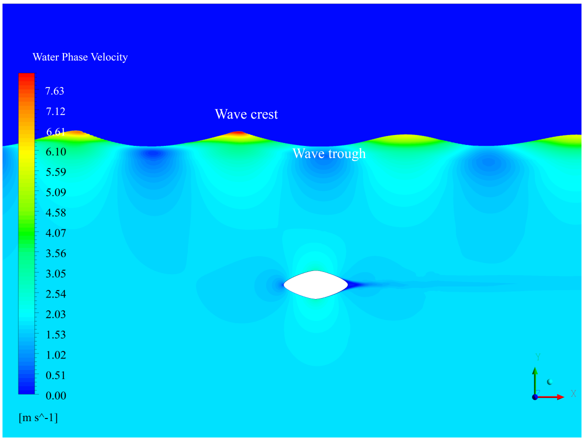

Figure 4.17: Velocity contours around the SFT cross-section at $t = 400$ s. The upper dark blue region is air, and the lower region is water

Since the wave height is determined using the corresponding x-component of the orbital velocities, the inline force of the SFT cross-section can be accurately calculated. However, the vertical force due to both the pressure fluctuation, and the vertical component of the orbital velocity is underestimated.

Table 4.4 summarizes the along-strait hydraulic properties of the SFT with the parametric shape under tsunami and typhoon scenario. The maximum in-line force on the SFT in the typhoon case is 12.5 times larger than in the tsunami scenario, demonstrating that for an SFT in the Qiongzhou Strait, typhoon impacts are more destructive and challenging than tsunami. The SFT mooring system design and net buoyancy adjustment ability should take these hazards into account.

Table 4.4: Summary of along-strait hydraulic properties of the SFT with the parametric shape

Extreme hydraulic events	Max. depth-averaged current speed (m/s)	Max. in-line force on the SFT (N/m)
Tsunami	0.9	200
Typhoon	1.65	2500

4.6. CONCLUSION

In this chapter, we calculated the worst-case tsunami and hindcast typhoon impacts on hydrodynamic forcing on an SFT in the Qiongzhou Strait. In order to determine the optimal SFT cross-section under extreme events, we proposed a parametric Bezier curve SFT profile and compared the hydrodynamic response with other simpler cross-sections. The main conclusions are briefly summarized as follows:

- The Qiongzhou Strait is sheltered by Hainan Island, so is partially spared extreme event hazards. The tsunami arrival time at the optimal SFT heading is about 4.2 h after an earthquake in the Manilla Trench. The maximum current speed along the strait is 0.9 m/s. During the hindcast typhoon, however, maximum current speed along the strait is 1.65 m/s, and significant wave height in the in-line direction is 4.8 m.

- Considering the in-line force components in the tsunami scenario, inertia plays an important role in the parametric Bezier curve shape, while for the circle shape, drag dominates the force. However, in the typhoon case, due to the slow variation of the mean current speed (from the storm surge, not from the waves, for which drag and inertia are both important), the inertial force can be neglected compared with the drag.

- The SFT cross-section using the parametric Bezier curve profile is recommended due to its streamlined shape and hydraulic force-mitigating effects. It experiences the minimum in-line force and the smallest wake region. Furthermore, serious vortex shedding is limited to a shorter time period and lower amplitude compared with other simpler shapes.

- In the typhoon scenario, the wave and current provide an approximately equal contribution to the in-line force. However, the waves play a dominant role in lift.

- The typhoon is more devastating than the tsunami for an SFT in the Qiongzhou Strait. The maximum in-line force on the SFT in the typhoon case is 12.5 times higher than in the tsunami scenario. The necessity and importance of hazard assessment and structural vulnerability in typhoon scenarios should be emphasized throughout the processes of engineering design, construction, operation and maintenance of an SFT.

The present study investigated forces on an SFT cross-section under extreme events. Additional research is required to further analyse the SFT dynamic and structural response. The impacts of super typhoon on the SFT, especially for the typhoon track in the SW direction, is required to further investigate. The three-dimensional effects of the SFT will also be addressed in follow-on research.

REFERENCES

Bernard, E. & Titov, V. (2015), ‘Evolution of tsunami warning systems and products’.

biu Liu, K., Shen, C. & sheun Louie, K. (2001), ‘A 1,000-year history of typhoon landfalls in Guangdong, Southern China, reconstructed from Chinese historical documentary records’, *Annals of the Association of American Geographers* .

Bricker, J. D. & Nakayama, A. (2014), ‘Contribution of trapped air, deck superelevation, and nearby structures to bridge deck failure during a tsunami’, *Journal of Hydraulic Engineering* .

Caldwell, R. L. & Edmonds, D. A. (2014), ‘Delft3D-Flow: Simulation of Multi-Dimensional Hydrodynaminc Flows and Transport Phenomena, Including Sediments-User Manual’, *Journal of Geophysical Research: Earth Surface* .

Data, C. T. C. (n.d.), ‘TC Size Analysis’.

Fenton, J. D. (1985), ‘A fifth-order stokes theory for steady waves’, *Journal of Waterway, Port, Coastal and Ocean Engineering* .

GEBCO (n.d.), ‘General Bathymetric Chart of the Oceans’.

Gross, J. M., DeMaria, M., Knaff, J. A. & Sampson, C. R. (2004), A new method for determining tropical cyclone wind forecast probabilities, *in* ‘26th Conference on Hurricanes and Tropical Meteorology’.

Haikou Meteorological Service (n.d.), ‘Haikou Meteorological Information sharing Service System’.

Hirt, C. W. & Nichols, B. D. (1981), ‘Volume of fluid (VOF) method for the dynamics of free boundaries’, *Journal of Computational Physics* .

Holland, G. (2008), ‘A revised hurricane pressure-wind model’, *Monthly Weather Review* .

Holland, G. J. (1980), ‘An analytic model of the wind and pressure profiles in hurricanes.’, *Monthly Weather Review* .

Holland, G. J., Belanger, J. I. & Fritz, A. (2010), ‘A revised model for radial profiles of hurricane winds’, *Monthly Weather Review* .

Hong Nguyen, P., Cong Bui, Q., Ha Vu, P. & The Pham, T. (2014), ‘Scenario-based tsunami hazard assessment for the coast of Vietnam from the Manila Trench source’, *Physics of the Earth and Planetary Interiors* .

il Seo, S., suk Mun, H., ho Lee, J. & ha Kim, J. (2015), ‘Simplified analysis for estimation of the behavior of a submerged floating tunnel in waves and experimental verification’, *Marine Structures* .

Imamura, F., Boret, S. P., Suppasri, A. & Muhari, A. (2019), ‘Recent occurrences of serious tsunami damage and the future challenges of tsunami disaster risk reduction’, *Progress in Disaster Science* .

Jeong, U. Y., Koh, H. M. & Lee, H. S. (2002), ‘Finite element formulation for the analysis of turbulent wind flow passing bluff structures using the RNG k - ϵ model’, *Journal of Wind Engineering and Industrial Aerodynamics* .

Jiang, B., Liang, B., Faggiano, B., Iovane, G. & Mazzolani, F. M. (2018), Feasibility study on a submerged floating tunnel for the Qiongzhou strait in China, *in* ‘Maintenance, Safety, Risk, Management and Life-Cycle Performance of Bridges - Proceedings of the 9th International Conference on Bridge Maintenance, Safety and Management, IABMAS 2018’.

Kunisu, H. (2010), Evaluation of wave force acting on Submerged Floating Tunnels, *in* ‘Procedia Engineering’.

Li, X. & Zhang, W. (2019), ‘3D numerical simulation of wave transmission for low-crested and submerged breakwaters’, *Coastal Engineering* .

Liu, P. L., Wang, X. & Salisbury, A. J. (2009), ‘Tsunami hazard and early warning system in South China Sea’, *Journal of Asian Earth Sciences* .

Megawati, K., Shaw, F., Sieh, K., Huang, Z., Wu, T. R., Lin, Y., Tan, S. K. & Pan, T. C. (2009), ‘Tsunami hazard from the subduction megathrust of the South China Sea: Part I. Source characterization and the resulting tsunami’, *Journal of Asian Earth Sciences* .

Michel, G. W., Becker, M., Reigber, C., Tibi, R., Yu, Y. Q. & Zhu, S. Y. (2001), ‘Regional GPS data confirm high strain accumulation prior to the 2000 June 4 Mw = 7.8 earthquake at Southeast Sumatra’, *Geophysical Journal International* .

Okada, Y. (1992), ‘Internal deformation due to shear and tensile faults in a half-space’, *Bulletin - Seismological Society of America* .

Pawar, S. & Brizzolara, S. (2019), ‘Relevance of transition turbulent model for hydrodynamic characteristics of low Reynolds number propeller’, *Applied Ocean Research* .

Ren, Z.-Y. & Liu, H. (2015), ‘Numerical study of potential extreme tsunami hazard in south china sea’, *Procedia Engineering* **126**, 332–338.

Roeber, V. & Bricker, J. D. (2015), ‘Destructive tsunami-like wave generated by surf beat over a coral reef during Typhoon Haiyan’, *Nature Communications* .

Shengzhong, W., Xiang, C., Qinxi, L. & Gengren, C. (2016), Research on Type Selection of Submerged Floating Tunnel of Qiongzhou Strait, *in* ‘Procedia Engineering’.

Shi, X., Liu, S., Yang, S., Liu, Q., Tan, J. & Guo, Z. (2015), ‘Spatial–temporal distribution of storm surge damage in the coastal areas of China’, *Natural Hazards* .

Tian, W., Song, B. & Ding, H. (2019), ‘Numerical research on the influence of surface waves on the hydrodynamic performance of an AUV’, *Ocean Engineering* .

TPXO (n.d.), 'OSU TPXO Tide Models'.

Wang, Y., Gao, T., Han, Z. & Liu, Q. (2017), 'Impacts of wind-field correction on the numerical simulation of storm-surge inundation during typhoon "Rammasun"', *Estuarine, Coastal and Shelf Science* .

Wankang, Y., Baoshu, Y., Xingru, F., Dezhou, Y., Guandong, G. & Haiying, C. (2019), 'The effect of nonlinear factors on tide-surge interaction: A case study of Typhoon Rammasun in Tieshan Bay, China', *Estuarine, Coastal and Shelf Science* .

Wauters, J. & Degroote, J. (2018), 'On the study of transitional low-Reynolds number flows over airfoils operating at high angles of attack and their prediction using transitional turbulence models'.

Wu, T. R. & Huang, H. C. (2009), 'Modeling tsunami hazards from Manila trench to Taiwan', *Journal of Asian Earth Sciences* .

Xu, J., Fu, Z., Bai, J., Zhang, Y., Duan, Z. & Zhang, Y. (2018), 'Study of boundary layer transition on supercritical natural laminar flow wing at high Reynolds number through wind tunnel experiment', *Aerospace Science and Technology* .

Yan, H., Zhang, F. & Yu, J. (2016), The Lectotype Optimization Study on Submerged Floating Tunnel Based Delphi Method, *in* 'Procedia Engineering'.

Yin, K., Xu, S., Zhao, Q., Huang, W., Yang, K. & Guo, M. (2020), 'Effects of land cover change on atmospheric and storm surge modeling during typhoon event', *Ocean Engineering* .

yuan Ren, Z., Zhao, X., long Wang, B., Dias, F. & Liu, H. (2017), 'Characteristics of wave amplitude and currents in South China Sea induced by a virtual extreme tsunami', *Journal of Hydrodynamics* .

Zhang, K., Xiang, Y. & Du, Y. (2010), Research on tubular segment design of submerged floating tunnel, *in* 'Procedia Engineering'.

Zhao, X., Jiang, Y., Ren, Z. & Liu, H. (2017), 'Historical tsunami records and potential tsunami scenarios near Haikou coastal region', *Natural Hazards* .

Zou, P., Bricker, J. D. & Uijttewaal, W. (2021*a*), 'The impacts of internal solitary waves on a submerged floating tunnel', *Ocean Engineering* **238**, 109762.

Zou, P., Bricker, J. D. & Uijttewaal, W. (2021*b*), 'Submerged floating tunnel cross-section analysis using a transition turbulence model', *Journal of Hydraulic Research* pp. 1–13.

Zou, P., Bricker, J. & Uijttewaal, W. (2020*a*), 'Impacts of extreme events on hydrodynamic characteristics of a submerged floating tunnel', *Ocean Engineering* **218**.

Zou, P., Bricker, J. & Uijttewaal, W. (2020*b*), 'Optimization of submerged floating tunnel cross section based on parametric Bézier curves and hybrid backpropagation - genetic algorithm', *Marine Structures* .

5

DYNAMIC RESPONSE AND CONFIGURATION OPTIMIZATION

In this chapter, multi-scale hydrodynamic solvers including large scale Delft3D model and small scale CFD model are used to consider the tempo-spatial randomness of the hydrodynamic loads along the submerged floating tunnel (SFT) span. A one-way fluid-structure interaction (FSI) model is established using finite element method (FEM) to assess the dynamic performance of an SFT. A typical long, large aspect ratio SFT is modeled by coupling tube, joint, and mooring components. The SFT is simulated in the time domain under currents, waves, internal waves, and extreme events. Flow-induced vibration (FIV) of SFTs with different cross-section shapes is investigated by analyzing each structure's natural frequencies, hydraulic loading frequency, and dominant modes. A structural parametric study is carried out for the SFT configuration optimization, which can be used for further synchronization suppression of the SFT. The hydrodynamic loads induced by extreme events and internal wave acting on the SFT in Chapter 3 and Chapter 4 are used for dynamic response analysis in this chapter. The dynamic response of the parametric shape proposed in Chapter 2 is compared with circular shape. In this chapter, an optimal SFT structure configuration procedure is proposed to minimize the global structural dynamic response of the SFT under environmental conditions. The highlights of this chapter are:

- *Multi-scale hydrodynamic models combined with the finite element analysis are proposed to predict dynamic response behavior of the submerged floating tunnel.*
- *A typical long SFT coupling tube-joint-mooring components model with a large aspect ratio is simulated in time-domain.*
- *Flow-induced vibrations of the submerged floating tunnel are numerically predicted under currents and waves.*

This chapter has been published as: Zou, P. X., Bricker, J. D., Chen, L. Z., Uijttewaal, W. S., Ferreira, C. S. (2022). Response of a submerged floating tunnel subject to flow-induced vibration. ***Engineering Structures***, 253, 113809.

- *An SFT with a parametric cross-section is recommended for a better dynamic performance than simpler shapes.*

5.1. INTRODUCTION

The dynamic behavior of the SFT should be scrutinized to evaluate structural feasibility and reliability. Cross-flow (CF) and in-line (IL) flow-induced vibration (FIV) under different hydraulic loading cases become crucial factors, inducing structural fatigue damage and affecting the lifetime of the SFT. As water flows over the SFT tube and mooring lines, it causes an unsteady pressure field over the SFT surface and sheds an unsteady wake, which can excite FIV. If oscillatory flow due to vortex shedding periodically occurs and synchronizes with one of the structural natural frequencies, the SFT's displacement of oscillation increases, leading to vortex-induced vibration (VIV), which is a category of FIV. VIV is associated with the so-called "lock-in" regime characterized by a shifting of vortex shedding frequency to the structural natural frequency. However, FIV research for the SFT remains in its infancy due to a series of key scientific challenges that have not been solved yet. The SFT is forced by a dynamic marine environment characterized by temporo-spatially varying hydraulic loading (e.g., typhoons), which brings challenges to the prediction of FIV for an SFT in engineering practice. Moreover, the SFT system is composed of a complex coupled mooring-tube-joint system (Zou et al. 2021). Though a key component in SFT engineering design, the flexible joints between SFT segments have not yet been investigated in sufficient depth. In addition, potential SFT construction sites call for a tunnel length up to thousands of meters (e.g., 1.4 km at the Hogsfjorde crossing in Norway (Larssen & Jakobsen 2010, Remseth et al. 1999); 3 km at Messina crossing in Italy (Martire et al. 2010); 20 km at the Qiongzhou Strait in China (Yan et al. 2016)). A pragmatic approach to FIV research for such a long structure with a large aspect ratio (over 100) is still lacking.

In recent years, SFT-focused FIV research is appearing by means of experimental tests, theoretical and semi-empirical methods, and numerical simulations. For experimental investigations, since no SFT prototype has yet been built, only scale tests in laboratories have been carried out. Deng et al. (Deng et al. 2020) investigated cross-flow VIV features of a twin-tube SFT segment via a self-oscillating physical model test under steady flow. However, structural material and the Reynolds number of the flow are key factors affecting the FIV characteristics. The small laboratory scale limits generalizing the achieved results due to the inability to simultaneously guarantee all the similitudes involved. Thus, dynamic response of a prototype SFT cannot be simply determined by scaled-down experimental tests. For mooring lines or single cylindrical tubes, such as risers, pipelines, and sonar strings, which are characterized by intrinsic slender and flexible elements, abundant scientific studies exist (Felisita et al. 2016, Kamphuis 1998, Wu et al. 2012, Liu et al. 2020). However, experimental research considering the SFT tube and mooring lines as a coupled system subject to FIV are still scarce. As for theoretical and semi-empirical methods, Chen et al. (Chen et al. 2018) investigated the VIV response of a coupled SFT tube–cable system under hydrodynamic forcing based on the Hamilton Principle, in which the SFT tube and cables were simplified as supported Euler-Bernoulli beams without torsional behavior. Hong and Ge (Hong & Ge 2010) and Wu et al.(Wu et al. 2010) employed the wake oscillator model to determine the displacement of vibration of the SFT tethers. VIVANA (Passano et al. 2014) and SHEAR7 (Vandiver & Li 2005) are also commonly used semi-empirical methods for VIV prediction in marine risers. However, these methods predict VIV based on empirical parameters obtained from large-scale experiments, while no abundant experimental results exist for the SFT. Moreover, with the addition of the mooring system and a buoyancy weight ratio (BWR) different from those of the experiments on which these methods are based, these semi-empirical tools for VIV prediction in risers and pipelines cannot be simply applied to the SFT. As for numerical methods, Chen et al. (Chen, Li, Fu & Guo 2016) explored mode competition and multi-mode VIV of the SFT using the finite element method (FEM), where the SFT was simplified as a flexible cylinder under a shear current. They used a third-order polynomial for the velocity of the structure to improve the Morison Equation. However, the coupled mooring and tunnel joint system was neglected. The FIV mechanism of the SFT is an intrinsic multi-physics issue with a strong interaction between the flow field and structure. A fully-coupled two-way fluid-structure interaction (FSI) simulation, in which data is exchanged between fluid and structural solvers at each time-step, can provide high-fidelity results for both structural response and flow field characteristics. However, the heavy computational burden of two-way FSI makes it impractical for a prototype SFT simulation due to the great (multiple kilometers) tunnel length involved (Zhang et al. 2015). Therefore, in the context of practical design purposes, the one-way FSI technique is a pragmatic way to simulate FIV with the assumption that the flow field is not heavily affected by structural deformation. Abundant studies have demonstrated that one-way FSI is capable of providing plausible results for FIV predictions (Ulveseter et al. 2018, Chen, Li, Zhang & Tan 2016, Wijesooriya et al. 2020, Benra et al. 2011). Therefore, in this study, the one-way FSI approach is applied for FIV prediction and analysis of the global dynamic response of an SFT.

In this chapter, multi-scale hydrodynamic models considering the tempo-spatial randomness of the hydrodynamic loads along the SFT span are implemented. A model of a large aspect ratio, super-long SFT with coupled tube-joint-mooring components is established with two different cross-section shapes under a variety of hydrodynamic loads. This chapter is structured as follows. Section 5.2 describes our methodology of combining multi-scale hydrodynamic models and an FEM solver to predict FIV of the SFT. Section 5.3 validates the numerical modeling setup. Section 5.4 simulates the dynamic response and FIV conditions of the SFT under currents and waves conditions. The dynamic responses of the SFT in extreme events and oceanic ISW conditions are analyzed in Section 5.5, followed by a global structural configuration optimization process and sensitivity analysis of multi-structural features in Section 5.6.

5.2. METHODOLOGY

For a long span structure such as an SFT, the spatiotemporal variation and randomness of hydraulic loading (due to currents, waves, tides, extreme events, etc.) along the span must be considered in the engineering design. CFD, as the most comprehensive and accurate modeling approach, requires fine resolution and so is too computationally burdensome for simulation of stochastic waves varying along the span in a large domain. Therefore, a multi-scale cascade of models solving the large-scale oceanographic hydraulic conditions and the small-scale hydrodynamic forcing on the structure, is established. For large-scale oceanographic simulations, the integrated tide, ocean storm surge, and wave modeling framework of Delft3D-FLOW (Hydraulics 2006) coupled with SWAN is applied with a coarse grid size to obtain the hydraulic loading along the SFT span. However, detailed flow characteristics and structural forcing need to be computed with fine resolution at a small scale by CFD. Since CFD enables the pressure distribution over the SFT surface to be determined precisely, the numerically acquired water surface elevation and flow speed from Delft3D-FLOW simulations are imported as inlet-boundary conditions into the CFD model. With reference to the concept of strip theory (where the 3-D flow field along the structure is discretized into several two-dimensional fluid strips, or planes) applied to long flexible risers (Duanmu et al. 2018, Lin & Wang 2019), the unsteady, spatially variable hydraulic loading can be specified at different locations along the span, improving the FIV prediction. As an effective numerical method in analyzing structure behavior, FEM is adopted for further analysis of the SFT dynamic response based on the hydrodynamic forcing calculated by the CFD. Using CFD in conjunction with FEM, motion of the structure, internal forcing, and FIV conditions can be assessed.

SFTs are subject to marine environmental conditions generally including currents, waves, internal waves, and extreme hydraulic events (e.g. tsunamis and typhoons). In order to investigate FIV of the SFT subject to different hydraulic loading, uniform current and regular wave induced forces are firstly calculated using the CFD code ANSYS Fluent v19.1 in section 5.4. For a conservative computation, the hydraulic loading direction is calculated perpendicular to the longitudinal direction of the SFT. Furthermore, to examine the most severe conditions, an extreme event (a super typhoon example in the Qiongzhou Strait) is simulated by the large-scale oceanographic hydraulic modeling framework of Delft3D-FLOW coupled with the spectral wave model SWAN, and the small-scale hydrodynamic forcing on the structure is solved by the CFD code ANSYS Fluent v19.1 (see in Chapter 4). Finally, a coupled tube-joint-mooring SFT model is computed using FEM in the time-domain for the global dynamic response analysis accordingly under internal waves and extreme hydraulic events in section 5.5.

5.2.1. HYDRODYNAMIC MODELS

At a large scale, Delft3D-FLOW is a widely-used ocean-scale prediction tool for tsunami events, tidal flows, and storm surges, solving the depth-averaged shallow water equations based on the finite-volume method (FVM) (Zou et al. 2020*a*, Roeber & Bricker 2015), applied in Chapter 4. At a small scale, most previous research (Chen et al. 2018, Chen, Li, Fu & Guo 2016, Lin et al. 2019, Jin et al. 2018) used the Morison equation for hydrodynamic modeling; however, this neglects the diffraction effect, which should be taken into account, especially for shorter waves. Furthermore, Morison equation coefficients are typically derived from experiments and restricted to simpler shapes. In addition, the Morison equation cannot provide flow field variables in detail. In this study, the CFD code ANSYS FLUENT v19.1 (ANSYS 2019) is applied to conduct high-resolution two-dimensional field-scale simulations of the SFT by solving the unsteady Reynolds-averaged Navier-Stokes (URANS) equations using FVM. The RNG $k-\epsilon$ model has been adopted for uniform current, regular wave, and extreme event modeling. Detailed governing equations of the RNG $k-\epsilon$ model, the volume-of-fluid (VOF) method, the applied Fifth-order Stokes wave theory, and the numerical computation domains and boundary settings are described in Chapter 2, 3, and 4.

5.2.2. STRUCTURAL GOVERNING EQUATIONS

The dynamic response equation for the SFT tube-joint-mooring system under hydraulic loading can be expressed as Eq.5.1.

$$[\mathbf{M}+\mathbf{M_a}]\,\ddot{w}+[\mathbf{C}]\,\dot{w}+[\mathbf{K_e}+\mathbf{K_m}+\mathbf{K_j}]\,w=\mathbf{F} \tag{5.1}$$

where $[\mathbf{M}]$ and $[\mathbf{M_a}]$ are the structural and added mass matrices, respectively; $[\mathbf{C}]$ is damping coefficient matrix; $[\mathbf{K_e}]$, $[\mathbf{K_j}]$and $[\mathbf{K_m}]$ are elastic stiffness of the SFT tube, joint and mooring stiffness matrices, respectively;$\ddot{w}$, $\dot{w}$ and w are the structural acceleration, velocity, and displacement vectors, respectively; $\mathbf{F}$ is the hydrodynamic loading vector.

For slender bodies such as SFTs, the three-dimensional added mass can be derived by integrating two dimensional added mass along the tube length (Tariverdilo et al. 2011). The added mass is expressed as 5.2.

$$M_a = C_A\frac{\rho_w \pi D^2 L}{4} \tag{5.2}$$

where C_A is the added mass coefficient; ρ_w is water density; D is the tunnel tube diameter; L is tube length.

The natural frequency is a key factor for structural dynamic response estimation. The vibration characteristics of the SFT, such as natural frequencies and corresponding vibration modes, can be obtained through modal analysis based on FEM using LUSAS v15.2 (LTD n.d.). The presence of water around the tunnel tube creates an added mass due to the displacement of this water by the motion of the tube, and hence, the natural frequencies in water (wet natural frequencies) of the SFT system decrease compared with the natural frequencies in air (dry natural frequencies). The Eigen-frequencies and Eigen-mode equations of the SFT system in water can be calculated in the absence of external forcing, expressed as Eq. 5.3.

$$[\mathbf{K_e}+\mathbf{K_m}+\mathbf{K_j}]-[\mathbf{M}+\mathbf{M_a}]\,[\omega^{\mathbf{2}}_{\mathbf{jj}}]=0 \tag{5.3}$$

where $[\omega^{\mathbf{2}}_{\mathbf{jj}}]$ is the diagonal matrix of the wet natural frequency of the SFT system.

For calculation of structural damping, Rayleigh damping is regarded as the most mathematically convenient model for structural dynamic response prediction, in particular for multi-degree-of-freedom systems (Liu & Gorman 1995). The system of governing equations of motion in the case of linear response can be decoupled by the use of a modal transformation. Although the validity of Rayleigh damping assumption has not been thoroughly investigated, it is the most commonly used damping model in engineering practice (Cruz & Miranda 2017). Classical mass- and stiffness-proportional Rayleigh damping is formulated as Eqs.5.4, 5.5, and 5.6.

$$[\mathbf{C}]=\beta_1\,[\mathbf{M}+\mathbf{M_a}]+\beta_2\,[\mathbf{K_e}+\mathbf{K_m}+\mathbf{K_j}] \tag{5.4}$$

$$\beta_1=\xi\frac{2\omega_i\omega_j}{\omega_i+\omega_j} \tag{5.5}$$

$$\beta_2=\xi\frac{2}{\omega_i+\omega_j} \tag{5.6}$$

where β_1 and β_2 are the Rayleigh damping coefficients; ξ is the modal damping ratio; ω_i and ω_j are the i^{th} and j^{th} mode natural frequencies of the SFT system, respectively.

5.3. STRUCTURAL DYNAMIC MODEL

5.3.1. MODEL VALIDATION

VALIDATION OF NATURAL FREQUENCY

To verify correctness and effectiveness of the natural frequency calculation for the SFT, the simulated results using modal analysis by LUSAS v15.2 are compared with the case study from Jin et al. (Jin et al. 2018), which conducted a coupled tunnel-mooring line dynamic analysis using OrcaFlex (Manual 2014). The SFT length, diameter, and cross-sectional wall thickness are 900 m, 23 m, and 1 m, respectively. The mooring interval is 50 m. Both tunnel ends are fixed. The bending and axial stiffness of the tunnel tube are 1.26×10^{11} kN·m^2 and 2.07×10^9 kN, respectively. The added mass coefficient is 1.0. A schematic model of the SFT is shown in Fig.5.1. Table 5.1 lists the validation results of the wet natural frequencies of the tunnel tube up to the 3rd mode. The maximum relative error is 3.45 %, indicating the present numerical predictions of structural natural frequencies are reliable.

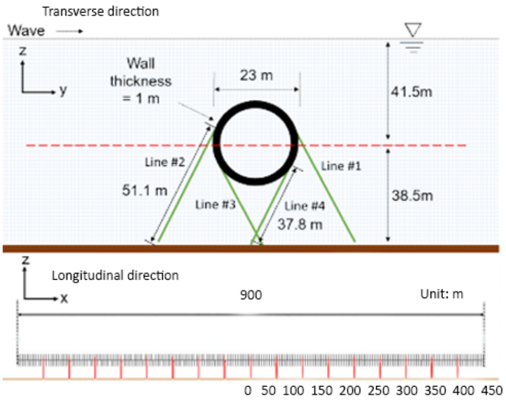

Figure 5.1: 2D schematic views of the entire system for the validation case (Jin et al. 2018)

Table 5.1: Wet natural frequencies of the SFT (Unit: rad/s)

Mode Number		ω_1 (Jin et al. 2018)	ω_2 (by LUSAS)	Relative error $\lvert\omega_1 - \omega_2\rvert/\omega_1$ (%)
Horizontal direction	1st mode	1.345	1.327	1.34
	2nd mode	1.630	1.598	1.96
	3rd mode	2.322	2.242	3.45
Vertical direction	1st mode	2.281	2.247	1.49
	2nd mode	2.455	2.412	1.75
	3rd mode	2.955	2.876	2.67

VALIDATION OF FIV PREDICTION

To further verify the reliability of FIV predictions for the SFT using the current approach, the response displacements of a cylinder are compared with the results reported by Govardhan and Williamson (Govardhan & Williamson 2000). A two-dimensional CFD model was established to obtain the hydrodynamic forcing on a fixed circular cylinder in a cross-flow, over the range of freestream velocities 0.04 ~ 0.40 m/s. The computational domain is 1.2 m in length and 0.4 m in height. A cylinder of diameter $D = 0.0381$ m is applied for the low mass-damping case. The first grid layer cell length normal to the cylinder surface has a value of Y^+ close to 1 as required by the SST $k-\omega$ turbulence model (Fig.5.2(a)). The computational mesh is divided into 3 domains with different cell sizes. The first cell size (S_1): the cell size parallel to the SFT cross-section surface. The second cell size (S_2): the maximum unstructured mesh size around the SFT. The third cell size (S_3): the maximum structured mesh size in the rest of the domain. The grid independent limit test (GIL) is carried out by exemplifying the case freestream velocity of 0.40 m/s. The time histories of the calculated drag and lift using the three cell sizes are presented in Fig.5.3, and the cell numbers and the calculated mean drag and the root mean square (RMS) lift force are listed in Table 5.2. It shows the lift force oscillation displacement and frequency of all the three cases are consistent which are around 4.8 m and 2 Hz, respectively. However, the drag force of Case 1 is under-predicted compared with other two cases. Case 2 has almost identical results as Case 3 (thus is regarded as converged), while with fewer cell numbers and saves computational time. Therefore, grid settings of Case 2 are used. The vortex shedding frequencies for the static cylinder at different freestream velocities are over the range of 0.2 ~ 2 Hz and cover the system natural frequency. The calculated drag and lift are then transferred to the three-dimensional FEM solver LUSAS v15.2 for the FIV predictions.

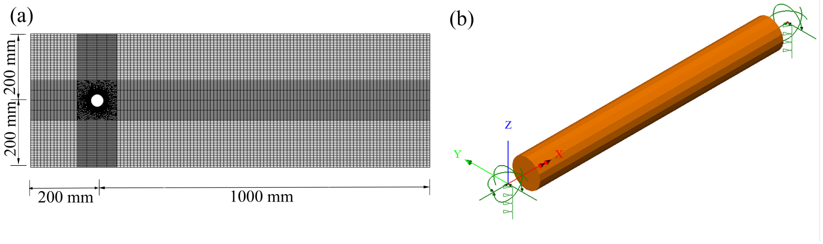

Figure 5.2: Validation models. (a) Schematic Mesh of the CFD model; (b) Structural model using LUSAS v15.2 (a pair of vertical springs act on both ends)

Table 5.2: Mesh size for the grid independent limit test, S is cell size, N_{Cells} is cell number

	S_1 (mm)	S_2 (mm)	S_3 (mm)	N_{Cells}	Mean Drag (N)	RMS Lift (N)
Case 1	1	5	5	21795	4.27	4.87
Case 2	1	2.5	5	28103	4.62	5.08
Case 3	0.5	2.5	5	30368	4.68	5.12

In the structural dynamic model, the cylinder length L is 0.381 m with a length-diameter ratio of 10 (Fig.5.2 (b)). The mass ratio (the reciprocal of BWR) is 1.19, which is consistent with the experimental conditions (Govardhan & Williamson 2000). The cylinder is modelled by “thick beam (BMS3)” elements with an element size of 0.01905 m. In the experiments, end plates were fixed to the test section and placed 2 mm below the bottom of the cylinder to encourage two-dimensional shedding, while in the numerical model, vertical springs with stiffness of 1270 N/m are set on both ends of the cylinder to provide the restoring forces (Deng et al. 2020). The calculated drag and lift are uniformly distributed along the span and perpendicular to the longitudinal direction of the cylinder. Structural modal analysis is firstly performed to determine vibration characteristics (natural frequency, Rayleigh damping coefficients). The natural frequency of the cylinder in still water is 1.01 Hz. The structural damping ratio in water is 0.045, and as per Eqs.5.4, 5.5 and 5.6, β_1 and β_2 are 0.286 s^{-1} and 0.007 s, respectively. The detailed model parameters are listed in Table 5.3.

Table 5.3: Model parameters for validation

Parameter	Value
Cylinder diameter (m)	0.0381
Cylinder length (m)	0.381
Young's modulus (kPa)	45
Poisson's ratio (-)	0.167
Dry density (kg/m^3)	1190
Water density (kg/m^3)	1000
Added mass coefficient (-)	1.0
Structural damping ratio in water (-)	0.045
Spring stiffness for cylinder in CF direction (N/m)	1270
Natural frequency in still water (Hz)	1.01

The onset of VIV can be assessed by a key non-dimensional parameter: reduced velocity V_R, expressed in Eq.5.7

$$V_R = \frac{U}{f_i D} \tag{5.7}$$

where U refers to the current speed; f_i is the Eigen-frequency of the structure.

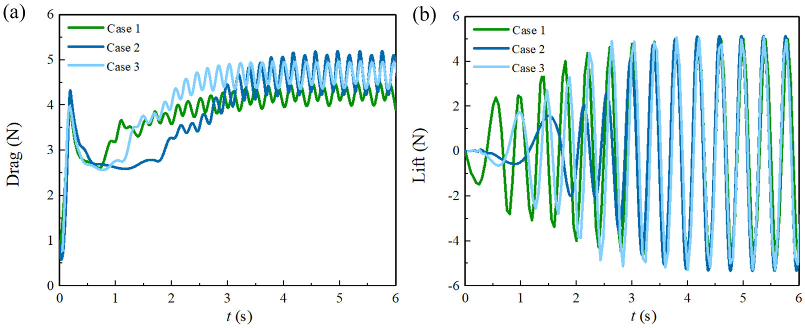

Figure 5.3: The time histories of the calculated drag and lift for grid independent limit tests

Fig.5.4 presents the simulated amplitude and frequency ratio of the numerical model compared with Govardhan and Williamson's results (Govardhan & Williamson 2000). It shows that the simulated results are inconsistent with the experiments at both initial and upper branches. The amplitude ratio (defined by A/D, where A is the peak value of the oscillation amplitude of the cylinder) exhibits a jump during the transition between initial and upper branches at $V_R = 5$ (where the vortex shedding frequency is close to f_n). It proves that the vibration frequency ratio (defined by f/f_n, where f is the cylinder oscillating frequency during induced vibration) during synchronization lies above 1 (Govardhan & Williamson 2000). Due to the assumptions of uniformly distributed hydraulic loading along the span and neglecting the actual surface roughness of the cylinder, dynamic response simulation of the SFT tube produces conservative results.

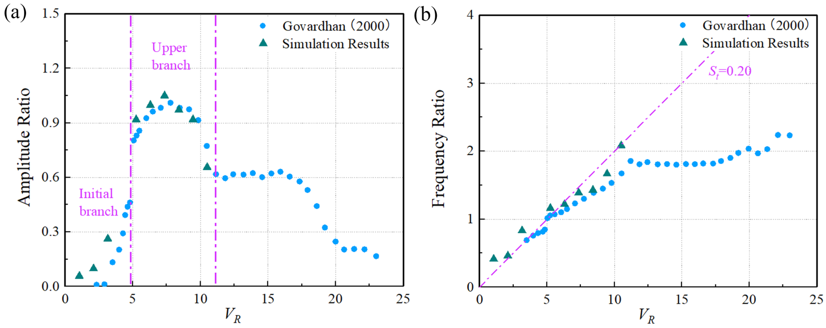

Figure 5.4: Amplitude and frequency variation with reduced velocity for a low-mass-damping cylinder. S_t is Strouhal number

5.3.2. NUMERICAL MODEL SETUP

STRUCTURAL MODEL SETUP

The characteristics of dynamic response of SFTs are complicated due to various types of hydrodynamic loads that the structure is exposed to and complex dynamic response of coupled components of tunnel tube, mooring lines, and tunnel joints. There is still no prototype SFT that has yet been built worldwide due to the immaturity of scientific research and technology. As one of potential SFT application sites, the Qiongzhou Strait, located between Hainan Island and the Leizhou Peninsula in the South China Sea (SCS), is applied for dynamic response analysis of the SFT in this study (Zou et al. 2022). The optimal SFT construction heading "Line V" (from Sitang in the Leizhou Peninsula to Tianwei in Haikou) is around 20 km width, shown in Fig.4.2. Therefore, the overall length of the SFT tube in the example is 20 km, consisting of 200 tunnel elements. The mooring sets moored at mid-span of each tunnel element with an interval of 100 m. The submergence depth of the SFT is 40 m with a water depth of 100 m, and the variety of underwater terrain is neglected.

The software LUSAS v15.2 is employed to establish an SFT model coupling tube-joint-mooring components for the global dynamic response analysis (Fig.5.5(a)), where the tunnel tube with mooring lines is modeled by a "thick beam (BMS3)" element, and the tunnel element joint is modeled by a "Point joint (JSH4)" element. Each element joint is simulated in six DOFs including three force spring units (axial spring unit, horizontal shear spring unit, and vertical shear spring unit) and three torque spring units (torsional spring unit, bending spring unit in horizontal plane, and bending spring unit in vertical plane). Internal rigid constraints are implemented between the mooring line ends and the central mass of the SFT tube nodes. The mooring line ends are imposed rotational releases. Both ends of the tunnel tube are fixed. The mooring lines are arranged symmetrically composing 4 mooring lines in each set to balance restoring forces (Fig.5.5(b)). The basic parameters with respect to geometric and material properties of the SFT are summarized in Table 5.4.

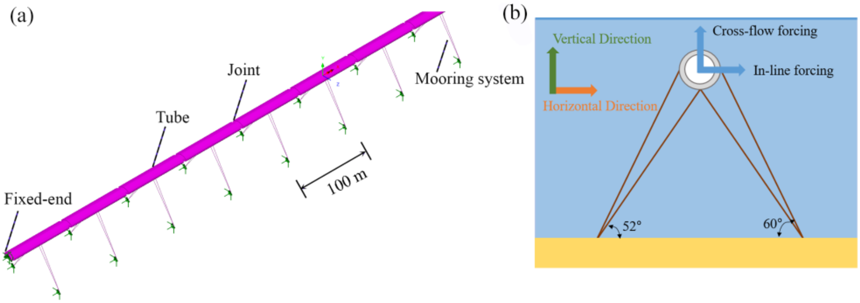

Figure 5.5: The SFT model; (a) Coupled tube-joint-mooring system FEM model (Part of the model); (b) Mooring lines arrangement

PARAMETERS OF SFT CROSS-SECTION

Steel shell-concrete (SSC) composite structures have been applied in advanced engineering constructions such as Kobe Port Minatojima (Kimura et al. 2002) and Shen-Zhong Link (Li et al. 2020). This has the merits of improving material properties, saving costs and manpower, and reducing the installation period and risk of seeping (Van Oorsouw 2010). Hereby, similar technology can be used for the SFT. It is designed as a “sandwich structure” consisting of the outer and inner steel shells and filled concrete layer inside in the walls of the cross-section (Fig.5.6). Longitudinal diaphragms and transverse webs can be implemented between the outer and inner steel plates. To simplify the input SSC material properties in our model, the elastic modulus E and density ρ can be obtained in terms of the equivalence of the axial and bending stiffness, and gross weight, given by Eqs.5.8, 5.9, and 5.10

$$EA = E_{s1}A_{s1} + E_cA_c + E_{s2}A_{s2} \tag{5.8}$$

$$EI = E_{s1}I_{s1} + E_cI_c + E_{s2}I_{s2} \tag{5.9}$$

$$\rho A = \rho_s(A_{s1} + A_{s2}) + \rho_cA_c \tag{5.10}$$

where E_{s1}, E_{s2}, E_c are the elastic modulus of outer shell, inner shell, and concrete, respectively; I_{s1}, I_{s2}, I_c are the cross-sectional moments of inertia of outer shell, inner shell, and concrete, respectively; A_{s1}, A_{s2}, A_c are the cross-sectional area of outer shell, inner shell, and concrete, respectively; ρ_s, ρ_c are the steel shell and concrete density, respectively; E, I, A, and ρ are the equivalent elastic modulus, moments of inertia, area, and density of the SSC structure, respectively. The material properties are summarized in Table 5.4.

Table 5.4: Structure and Material parameters

Structure	Parameter	Value
Tunnel tube	Total length (km)	20
	Element length (m)	100
	Young's modulus (GPa)	40.2
	Dry density (kg/m^3)	2698
	Water density (kg/m^3)	1050
	Added mass coefficient (-)	1.0
	Damping ratio (-)	0.025
	Inner and outer shell thickness (mm)	16
	Tunnel wall thickness (m)	1.0
	Lateral clearance W (m)	11
	Vertical clearance H (m)	5
	Cross-sectional area of circular shape (m^2)	41.1
	Cross-sectional area of parametric shape (m^2)	43.8
Mooring line	Mooring interval (m)	100
	Nominal diameter (m)	0.18
	Mass/Unit length (kg/m)	644.7
	Added mass coefficient (-)	1.0
	Minimum breaking load (kN)	30689 (Grade R5)
Tunnel joint	Axial stiffness (GN/m)	22.1
	Shear stiffness (GN/m)	0.76
	Bending stiffness (GN·m)	548
	Torsional stiffness (GN·m)	592

In order to compare the FIV conditions and dynamic response of the SFT with different cross-section shapes, numerical models with two types of cross-section shapes (i.e., circular and parametric shapes shown in Fig.3.2, in order to be concise, the elliptical shape is not included in this chapter) are built up, respectively. The parametric shape is described by Bézier curves with the parameters combination of $b = 1.5$ m, $r = 0.5$ m, and $y_t = 4$ m. The definition of Bézier parameters can be found in Chapter 2(Zou et al. 2020*b*). Apart from the cross-sectional area, cross-sectional clearance and wall thickness, and structure and material parameters of the two numerical models are kept equal.

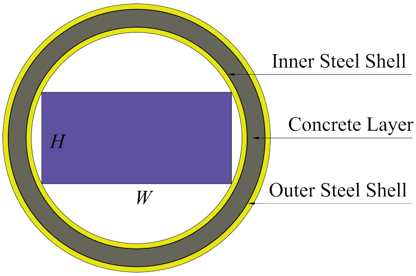

Figure 5.6: SFT Steel shell concrete cross-section (the purple area represents the vehicle clearance zone)

PARAMETERS OF SFT JOINT

Since the SFT tube may have a length of multiple kilometers, a monolithic tunnel tube cannot be cast due to issues with concrete cracking, transportation, and installation.

Thus, tunnel segments or elements should be constructed, assembled, and connected with joints. The restrictions of the six degrees of freedom (DOFs) of the element joint should be accessed by the reliability and durability of the structure.

The allowable axial expansion-compression and water tightness properties need to be accounted for in the SFT joint design. With reference to immersed tunnels, Gina gasket and omega profiles designed to withstand axial loading and form water seals can be implemented. Gina gaskets are pre-compressed due to the water pressure and stiffened when further compressed, and are unstiffened when decompressed. The loading-compression behavior can be categorized into three regions by simplifying the curve of Fig.5.7, where the initial axial stiffness k_0 is determined by the initial water pressure (Van Oorsouw 2010).

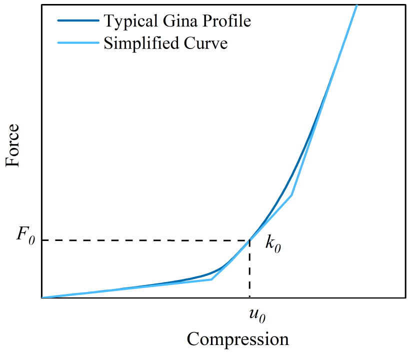

Figure 5.7: Gina gasket loading-compressive behavior

The Gina gasket is modelled as elastic spring and two rotational springs (which control the pitch and yaw motions) with axial stiffness k_u and bending stiffness k_θ. For a circular Gina gasket, stiffnesses can be obtained by Eqs.5.11 and 5.12.

$$k_u = 2\pi k_\theta r \tag{5.11}$$

$$k_\theta = \frac{M_{total}}{\theta} = \pi k_0 r^3 \tag{5.12}$$

where r is the circle radius. A detailed derivation is in APPENDIX.

Transverse deformation of the joint should be restrained to avoid large displacements and leakage. With reference to immersed tunnels, shear forces in the joint can be transferred by shear keys, which can be applied as a basis for the SFT's joint design. The shear keys can be set uniformly on the outer or inner sides of the tunnel wall. The shear capacity of the joint is mainly determined by material property, wall thickness, and quantity, dimensions, and fabrication techniques of the shear keys. Torsional stiffness of the joint can also be provided by shear keys. The detail joint design including Gina gasket and shear keys can be seen in Fig.5.8.

To assess the shear key capacity of the joint for dynamic response modelling of the SFT, a three-dimensional FEM model consisting of two tunnel elements is established using LUSAS v15.2. Each element length is 100 m. Six shear keys with each dimension of 3 m × 0.6 m × 0.6 m are uniformly placed along the outer side of the wall (Fig.5.9). The grid size of shear key and tunnel element is 0.1 m and 1 m, respectively. The tunnel elements and shear keys are modelled by the hexahedral volume element (TH4). The total nodes and elements in the model are 26052 and 18132, respectively. A rigid link constraint is applied to connect all the nodes on the shear keys (child nodes) with a center node (parent node), and hence, a unit vertical or torsional load can be added directly on the parent node. The effect of contact between surfaces of the two elements is simulated by a “slide-line” with a Coulomb friction coefficient of 0.2, and a close contact spring stiffness is adopted to soften the transition between in-contact and out-of-contact states. The material properties of the shear keys are equal to the tunnel element tube shown in Table 5.4. Accessories such as rubber pads are neglected in the model.

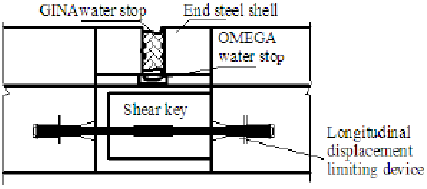

Figure 5.8: Schematic drawing of the SFT joint design (Zhang et al. 2010)

Table 5.5: Calculated results for shear keys

Description	Value
Max. displacement of shear keys under unit vertical load	1.32×10^{-9}m
Max. displacement of shear keys under unit twisting load	1.69×10^{-12}rad

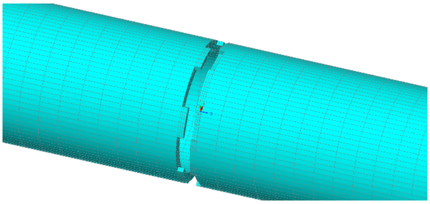

Figure 5.9: FE mesh of shear keys applied in the model

Fig.5.10 shows the shear stress distribution on each side of the joint under unit twisting and vertical load, respectively. It can be found that stress concentrates at the corners of the shear keys under the twisting load. Furthermore, larger shearing resistance is contributed by the horizontal shear keys compared with the vertical ones under the vertical load. By obtaining the maximum displacement of the shear keys in Table 5.5, the shear and torsional stiffness of the joint can therefore be estimated as 0.76 GN/m and 592 GN·m, respectively. Detailed joint properties composed by Gina gasket and shear keys are listed in Table 5.4. However, in engineering practice, the tunnel joint should be further assessed considering multiple factors such as mechanical properties, waterproofing, loading, construction technique, and maintainability.

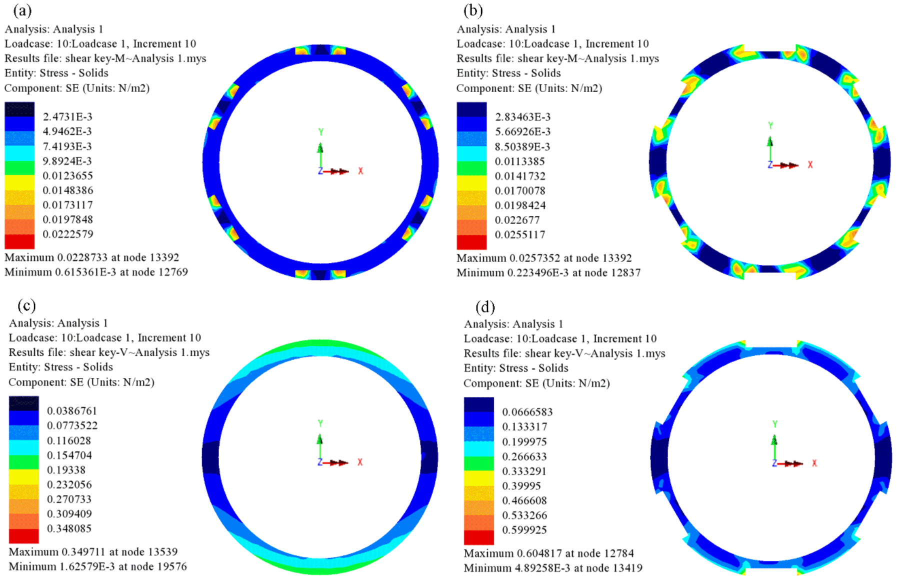

Figure 5.10: (a, b) Stress contour under twisting condition at the front and reverse side of the shear keys, respectively; (c, d) Stress contour under unit vertical load at the front and reverse side of the shear keys, respectively

5.3.3. MODAL ANALYSIS

The wet natural frequencies of the two numerical models are computed using LUSAS v15.2 and are listed in Table 5.6, and the obtained eigenmode shapes are presented in Fig.5.11 (by exemplifying the parametric shape). Directions of excited motion of the first ten modes are consistent between the two models, but slightly larger natural frequencies for the circular shape are observed than for the parametric shape.

Table 5.6: Wet natural frequencies of the SFT tube for different cross-section shapes

Mode number	Wet natural frequency (Hz)		Direction
	Circular shape	Parametric shape	
1	0.129	0.123	Horizontal
2	0.133	0.127	Horizontal
3	0.139	0.130	Horizontal
4	0.139	0.137	Axial
5	0.146	0.138	Horizontal
6	0.153	0.143	Horizontal
7	0.160	0.150	Horizontal
8	0.166	0.156	Horizontal
9	0.172	0.162	Horizontal
10	0.176	0.166	Horizontal

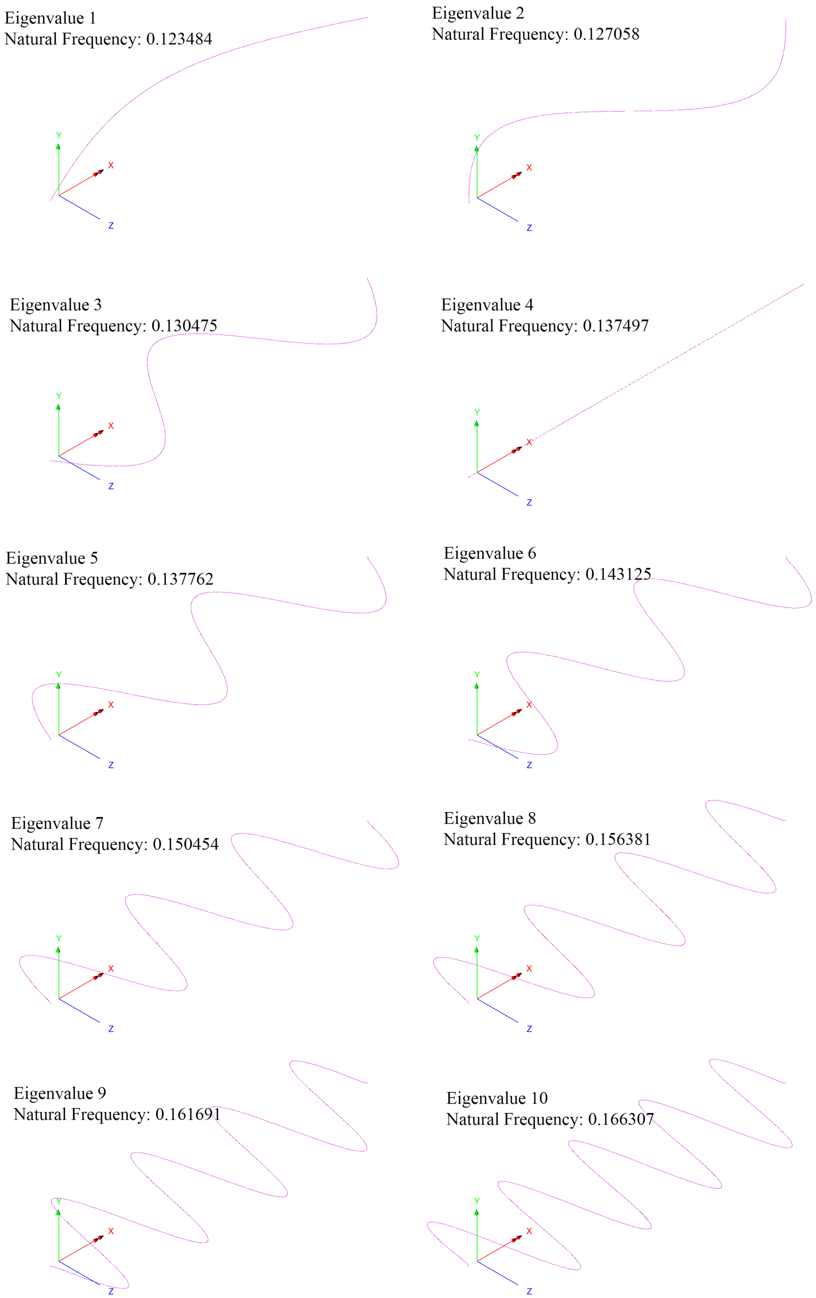

Figure 5.11: Numerical eigenmode shapes of the SFT with the parametric shape cross-section. Frequency in Hz

5.4. FIV CONDITION RESULTS

5.4.1. FIV CONDITIONS UNDER CURRENTS

The velocity fields and hydrodynamic forcing on two types of cross-sections (i.e., circular and parametric shapes) with a current speed of 1.5 m/s solved by the CFD code ANSYS Fluent v19.1 are shown in Fig.5.12. It can be seen that the parametric shape experiences flow separation further downstream and has a smaller wake region than the circular cross section due to its more streamlined geometry (Fig.5.12 (a) and (b)). The circular shape exhibits a classical '2S' vortex formation mode (characterized by two single vortices shedding per oscillation cycle), corresponding to the so-called "initial branch" sequence. Furthermore, the drag is over ten times smaller for the parametric shape than the circular shape (Fig.5.12(c)). Since no apparent vortex pattern can be observed with the parametric shape, the drag and lift forces on the SFT are thereby effectively mitigated.

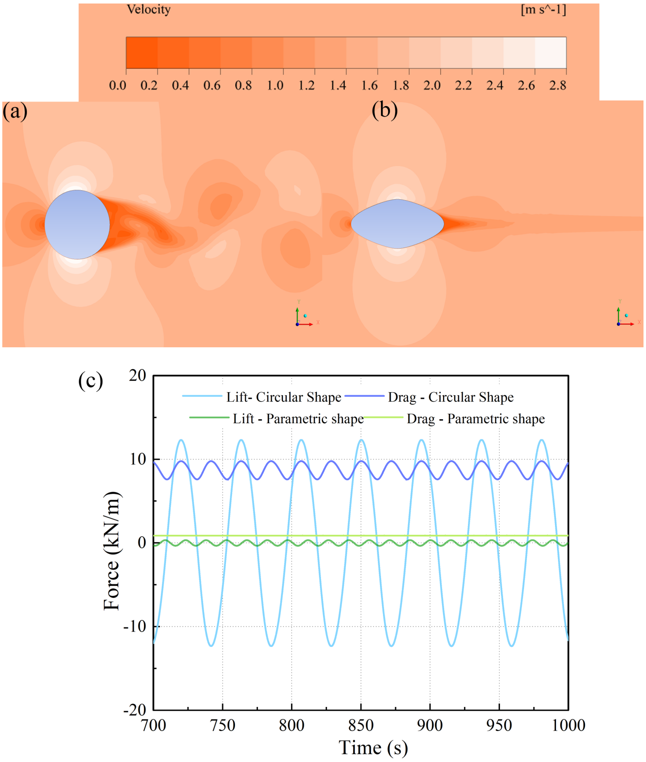

Figure 5.12: (a) Instantaneous flow velocity contour for the circular shape; (b) Sequential flow velocity contour for the parametric shape; (c) Drag and lift time-history for the two shapes at $V = 1.5\,\mathrm{m\,s^{-1}}$

To compare dynamic response of the SFTs with the two cross-section shapes under current conditions, firstly, uniform current speeds varying from 0.5 m/s to 1.5 m/s at 0.25 m/s intervals are selected based on practical hydraulic conditions; subsequently, the stable (after model spin-up) hydrodynamic forcing on the two types of cross-sections under each current speed is computed by CFD; finally, the calculated hydrodynamic forcing in the time-domain is used as the hydraulic load acting on each tunnel element node of the FEM structural model with the corresponding shape for structural dynamic analysis.

A comparison of the envelopes of the tube displacements at different current speeds between the circular shape and the parametric shape is seen in Fig.5.13 (to prevent clutter, only current speeds of 0.50 m/s, 1.00 m/s , and 1.50 m/s are shown). In the inline (IL) direction, the displacements of the tube with circular shape are ten times larger than with the parametric shape (Fig.5.13 (a)), which concurs with the magnitude of the drag (Fig.5.12 (c)). In the cross-flow (CF) direction, the displacement of the tube with circular shape is thirty times larger than that of the parametric shape case (Fig.5.13 (b)), indicating the displacement of the SFT tube can be effectively reduced by adopting the parametric cross-section. The tube displacement in the IL direction are larger than that in the CF direction, indicating the in-line forcing has a major impact on the structural dynamics.Note that the it is unlikely to induce large displacements of the SFT tube under steady currents, similar to what was seen by prior work (Lin et al. 2018).

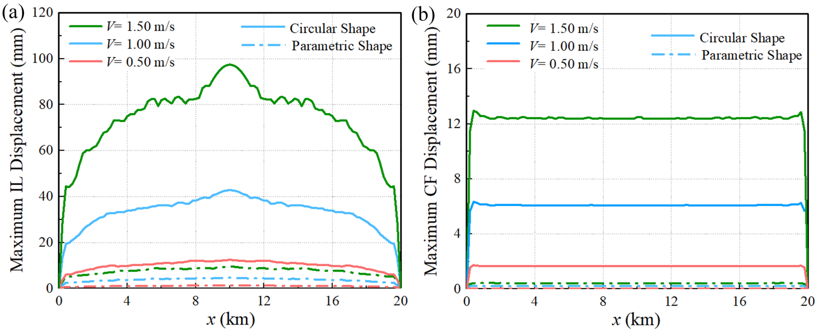

Figure 5.13: (a, b) Envelopes of IL and CF displacements under steady currents for different shapes

The relation of maximum IL displacement of the tube with different cross-sectional shapes to V_R is shown in Fig.5.14. The displacement increases with increasing current speed. The maximum IL displacement is approximately linearly correlated with V_R, with a slope of 0.150 m for the circular shape and 0.020 m for the parametric shape. Chen et al. (Chen et al. 2018) found that the “lock-in” phenomenon for the SFT system under steady current conditions occurs at $V_R = 5$. Govardhan and Williamson (Govardhan & Williamson 2000) found that the largest VIV response for a cylinder with a small mass ratio occurs at $V_R = 8$. It is clear that the V_R values in our models are far away from the lock-in regime and the “upper branch” (characterized by a notable jump in the vortex phase), making resonance between vortex shedding and the dynamic response of the SFT tube unlikely. In this case, to reduce computational load, the static analysis is suggested. However, if the mooring stiffness is not sufficient or the current speed is high enough, the vortex shedding frequency can overlap with the natural frequencies of the SFT. In that case, dynamic analysis is essential. However, for thin mooring cables, V_R can vary over a wide range and may overlap the lock-in region.

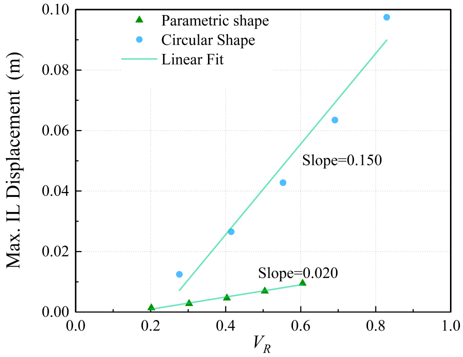

Figure 5.14: The maximum IL displacement of the tube versus the reduced velocity

5.4.2. FIV CONDITIONS UNDER WAVES

In order to evaluate dynamic response of different cross-section shapes of the SFT tube under wave forcing, measured wave data in the Qiongzhou Strait is used (Jiang et al. 2018) (Table 5.7). Fig.5.15 compares the computed stable (after model spin-up) wave load calculated using CFD, acting on the two shapes for waves with a return period of 20 years. The parametric shape experiences a smaller in-line force due to its smaller characteristic length than that of the circular shape.

Table 5.7: Measured data for extreme wave conditions in the Qiongzhou Strait

Return Period (year)	Wave Height (m)	Wave Length (m)
20	7.0	115.11
25	7.3	119.45
100	8.6	137.38

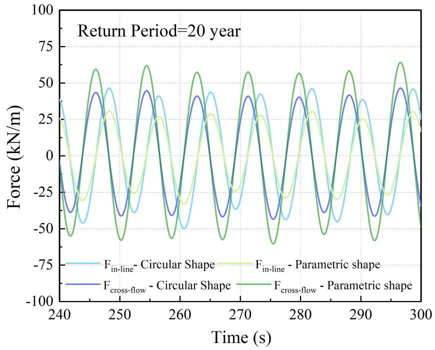

Figure 5.15: Wave force time-history of the two shapes with a wave return period of 20-years

A comparison of the envelopes of the tube displacements at different wave conditions between the circular shape and the parametric shape is seen in Fig.5.16 .The maximum IL displacement reaches 2.7 m at a return period of 20 years because the wave frequency is close to the first mode structural frequency (IL direction) of the SFT tube with the circular shape. The maximum CF displacement is 0.2 m at a return period of 100 years with the parametric shape, and the displacement remains nearly constant along the span. The CF displacement for the parametric shape is larger than for the circular shape; this is consistent with the forcing distribution. The reduction of the tube stiffness with the parametric shape (due to a large cross-section area) also incurs an increase of displacement in the CF direction. Again, it proves that the tube displacements in the IL direction are much larger than that in the CF direction, making reduction of the in-line force more important than the force in CF direction. Since the parametric shape has a smaller IL displacement, its hydrodynamic performance is preferable to that of the circular shape. It should be noted that in actual engineering practice, the SFT cross-section design should also consider the combined effects of the hydrodynamic characteristics, structure behavior, technical difficulties, service level, and construction cost.

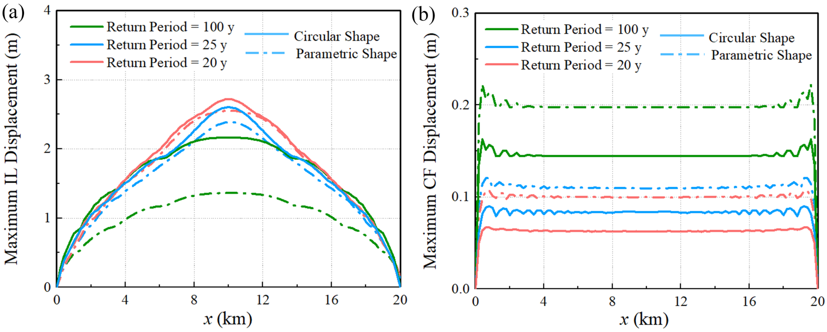

Figure 5.16: (a, b) Envelopes of the maximum IL and CF displacements under waves for different shapes

To better comprehend the impacts of the wave parameters on the FIV, a sensitivity analysis of wave height and period is carried out. Considering it was proved that the structural displacement increases with increasing wave height (wave load is approximately proportional to wave height) (il Seo et al. 2015), and the displacement in the CF direction is comparatively small, we explore how wave period affects only the IL displacement of the SFT tube with the parametric shape. A fixed wave height of 7 m with wave periods of 7.6 s, 7.2 s, 6.8 s, 6.4 s, and 6.0 s are selected.

Fig.5.17 shows the envelopes of the tube displacements under various wave periods. As the deflected shape of the tube reflects the mode of excitation, a single dominant vibration mode is presented at each wave period of 7.2 s, 6.4 s, and 6 s. The corresponding vibration modes are the fifth mode, the seventh mode, and the eleventh mode, respectively. However, multiple dominant vibration modes exist at wave periods of 7.6 s and 6.8 s, due to the irregularity of the oscillation shapes. It can be found that with decreasing wave period, higher vibration modes are excited, but the maximum tube displacement doesn't show positive correlation with wave period. The case of wave period of 7.2 s illustrates a larger dynamic response than T = 7.6 s, and the case of T = 6.4 s has the approximately equal maximum displacement as T = 6.8 s. It can be concluded that a single-mode dominant vibration, to a certain extent, amplifies structural displacement compared with multi-mode vibration. As per Kunisu (Kunisu 2010), the wave force acting on the SFT is strongly dependent on wave number. Firstly the wave force increases dramatically with increasing wave number and after achieving a peak value at a certain wave number, force decreases slowly with increasing wave number. Therefore, the maximum displacement at T = 7.6 s is smaller than at T = 7.2 s and it decreases remarkably for wave periods lower than 7.2 s.

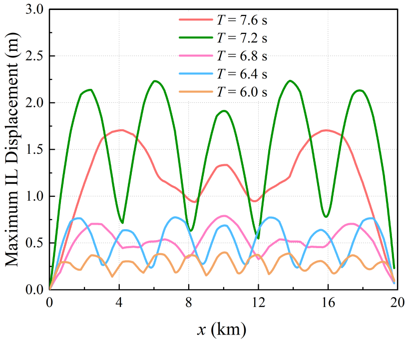

Figure 5.17: Envelopes of the maximum IL displacement of the parametric shape for various wave periods.

In order to further demonstrate the excited modes at different wave periods and determine the dominant modes explicitly, time series of IL displacement along the entire span, and the corresponding density spectrum at mid-span, are depicted in Fig.5.18. The vibration frequency spectra are attained by employing a fast Fourier transform (FFT). A fifth mode standing wave pattern is seen at T =7.2 s in Fig.5.18 (a). Meanwhile, a single dominant vibration frequency associated with the fifth mode (0.143 Hz), followed by a weak spectral peak from the first mode (0.123 Hz), is observed in Fig.5.18 (b). However, at T = 7.6 s, two dominant vibration modes with similar modal weights are seen in Fig.5.18 (d). The third mode (0.130 Hz) appreciably overlaps the first mode (0.123 Hz), and both vibration modes contribute to the dynamic behavior of the SFT tube (Fig.5.18 (c)). It can be further verified by Fig.5.11 and Fig.5.17 that the deflected shape of the tube at T = 7.6 s is mainly composed of a third mode superposed with a first mode. Compared with steady current conditions, unlike the generally current-dominated situation of risers, FIV of the SFT tube is more critical under wave conditions due to its large cross-section. Wave effects on the SFT are remarkable and complex, particularly for single dominant mode excitations.

5.5. DYNAMIC RESPONSE ANALYSIS

5.5.1. DYNAMIC RESPONSE OF THE SFT UNDER INTERNAL SOLITARY WAVES

Since the parametric cross section shape has preferable response properties for both current and wave conditions, the dynamic response of the parametric shape under the internal solitary waves (ISWs) is analyzed. The applied shear stiffness of the tunnel joint (Table 5.4) is less than the axial stiffness, which means the hydrodynamic load direction transverse to the tunnel tube in the horizontal plane is more critical than the longitudinal direction. Therefore, the scenario of ISW-induced force transverse to the tube is considered more conservative than oblique internal wave loading conditions. Furthermore, as per (Chen et al. 2020), the effect of ISW direction on the vertical force on the SFT is negligible. Therefore, as a conservative scenario, the applied external ISW-induced dynamic load is assumed to be uniformly distributed along the tube element nodes, in a direction transverse to the tunnel span. This uniformly distributed load along the fixed-end tube is regarded as one of the worst case scenarios, because it generates the largest shear force at the end of tube, in addition to large bending moments at both mid-span and tube ends. A tube submergence depth of 40 m, corresponding to the case d = 10 m in Chapter 3(Zou et al. 2021), is selected for structural dynamic simulation, in which the influence of buoyancy shift on the SFT can be clearly seen, as shown in Fig.5.19.

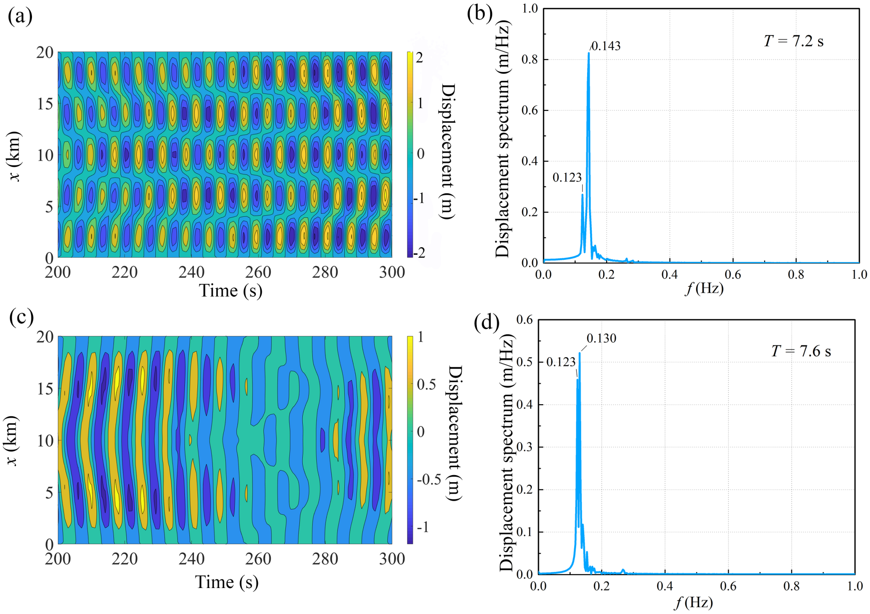

Figure 5.18: (a, b) Time series of IL displacement along the entire span, and mid-span frequency spectrum at T = 7.2 s; (c, d) Time series of IL displacement along the entire span, and mid-span frequency spectrum at T = 7.6 s

Fig.5.20 (a) depicts the envelopes of the tube deflection and acceleration in both horizontal and vertical directions under the ISW. It is observed that the maximum deflection of the tube is about 2.75 cm at mid-span, while the maximum acceleration of the tube is about 2 $\mathrm{mm\,s^{-2}}$ near the shore connections. These values are far less than that of the structural serviceability requirements of floating bridges(Aashto 2010, Koglin 2003, Lwin 2000), implying the effect of internal waves on the dynamic motions of the SFT tube is negligible. This is because, unlike the surface waves for which the wave frequency may overlap the structural natural frequency and amplify the structural response, the frequency of the ISW is much lower than the natural frequency of the SFT tube. Therefore, the SFT is not prone to the resonance with the ISW.

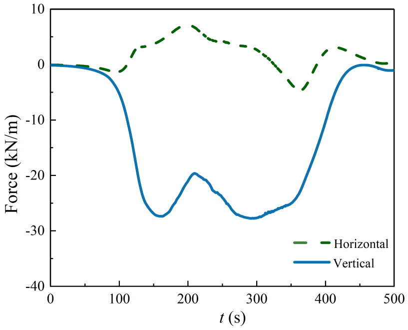

Figure 5.19: The selected ISW-induced force on the SFT with a = 20 m, d = 10 m, parametric cross-sectional shape, and $\rho_1/\rho_2 = 0.970$

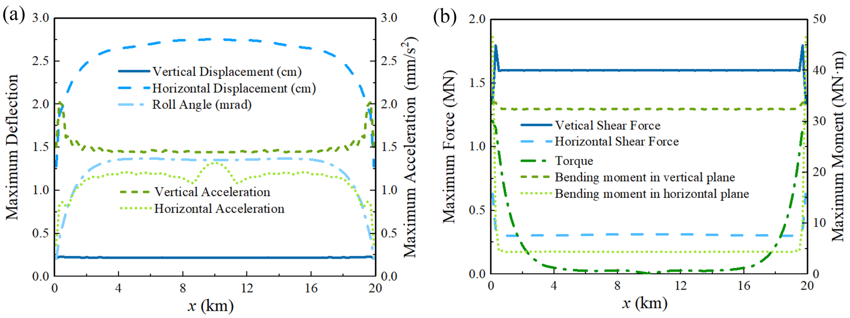

Figure 5.20: (a) Envelopes of the maximum tube motion; (b) Envelopes of the maximum tube internal forcing

Fig.5.20 (b) shows the envelope of the internal force in the SFT tube along the span under the ISW. The maximum shear force reaches 1.8 MN in the vertical direction, and the maximum bending moment in the horizontal plane can be over 45 MN·m near the shore connection due to the end constrains. Even though the displacement and acceleration of the SFT subjected to the ISW are relatively small, the large shear force and bending moment due to the buoyancy shift induced by ISW still affects BWR, and ultimately the tension force in the mooring lines. This can threaten the safety and reliability of the SFT system, which should be carefully examined during engineering design.

5.5.2. DYNAMIC RESPONSE OF THE SFT UNDER EXTREME HYDRAULIC EVENTS

Chapter 4 shows that the storm surge is more devastating than tsunami in the Qiongzhou Strait (Zou et al. 2020*a*). Therefore, as the most powerful and strongest typhoon to make landfall on Hainan Island since 1949, super typhoon Rammasun (2014) was selected as an extreme event for hydrodynamic assessment of the SFT. Rammasun made first landfall on Wenchang, Hainan at 7:00 UTC on July 18, 2014, and dissipated when it made its second landfall in Guangxi province on July 19. We evenly placed seven virtual gauges along the SFT heading (“Line V”) to obtain the hydrodynamic conditions in the Qiongzhou Strait (Fig.4.2 in Chapter 4). Therefore, the 20 km long SFT tube is divided into seven tube reaches, and the hydraulic loading on each reach is taken as the loading measured at the corresponding virtual gauge. The tube reach length is 2.5 km at Gauges #2 ~ #6 and 3.75 km at Gauges #1 and #7.

In order to consider spatiotemporal variation and randomness of hydraulic loading (typhoon-induced waves) along the tunnel span, a large-scale oceanographic model in the far-field was established by means of coupling the integrated atmosphere-ocean framework of Delft3D-FLOW and SWAN. The hydrodynamic model computational time step is 1 s, and is coupled with a stationary SWAN wave simulation every 60 min. Wind stress and tidal forcing drive the simulation from 0:00 on July 14 to 0:00 on July 20, 2014. Detailed model settings and typhoon track data can be found in Chapter 4. Time series of wave height are determined by the along strait component of wave energy flux and the corresponding wave period at each virtual gauge, which were extracted from the model as shown in Fig.5.21. It can be observed that the maximum wave height at each virtual gauge occurs at 14:00 on July 18 as the typhoon eye enters the strait. Therefore, for a conservative consideration, the maximum wave height and the corresponding wave period at each virtual gauge are adopted for small-scale hydrodynamic forcing simulation. The wave force on the SFT at each virtual gauge location (force per meter) is solved by a two-dimensional flow strip using the CFD code ANSYS Fluent v19.1. The wave force on each tube reach is solved by integrating the hydraulic loading (force per meter) at the corresponding virtual gauge along the reach. Therefore, the spatiotemporally varying wave force on the super long tunnel tube can be properly considered by spatially varying the hydraulic loading on different tube reaches in the time-domain.

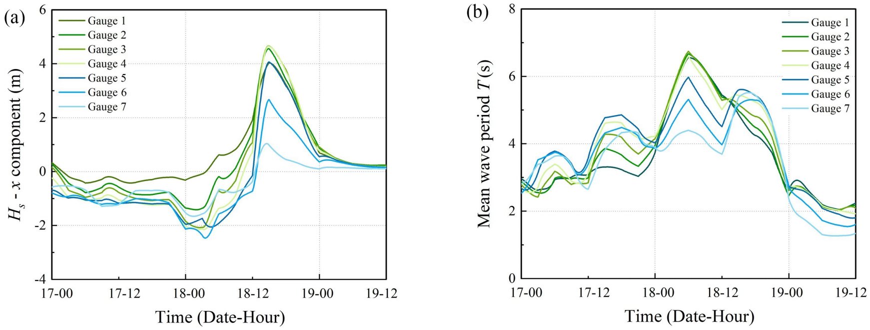

Figure 5.21: (a) Wave heights corresponding to along-strait components of orbital velocity vectors at the seven virtual gauges; (b) The corresponding wave periods at the seven virtual gauges

The global dynamic response of the coupled tube-joint-mooring SFT model under this extreme event is analyzed using LUSAS v15.2 in the time-domain. According to section 5.4, the SFT tube with the parametric shape has preferable dynamic response properties under both current and wave conditions. Therefore, the global dynamic response of the SFT is assessed for the parametric shape.

Fig.5.22 shows the envelopes of the IL displacement and internal forces on the SFT along the span under the extreme event. The displacement, acceleration, and internal forcing in the horizontal direction are much larger than in the vertical direction. The maximum displacement, acceleration and shear force reach 0.28 m, 0.36 $\mathrm{m\,s^{-2}}$, and 4.6 MN at x = 5.7 km, respectively. The torque is much larger than the bending moment which reaches the maximum value of 280 MN·m at x = 4.9 m. The forcing variation along the span may cause fatigue damage to the joints. Since both ends are assumed to be fixed in the simulation, excessive internal forcing due to torque and bending moment may cause structure fatigue and buckling damage at the shore connections. In this case, elastic bearings, bi-linear elastic bearings, and passive isolation bearings can be incorporated as options for the shore connections (Xiao & Huang 2010). An intermediate flex joint allowing axial deformation such as a telescopic joint or stroke-out-of-slip joint as applied in marine risers can also be utilized in the SFT shore connection design (Kavanagh et al. 2002). However, investigation of shore connection type and its effects on dynamic response of the SFT are not within the scope of this research.

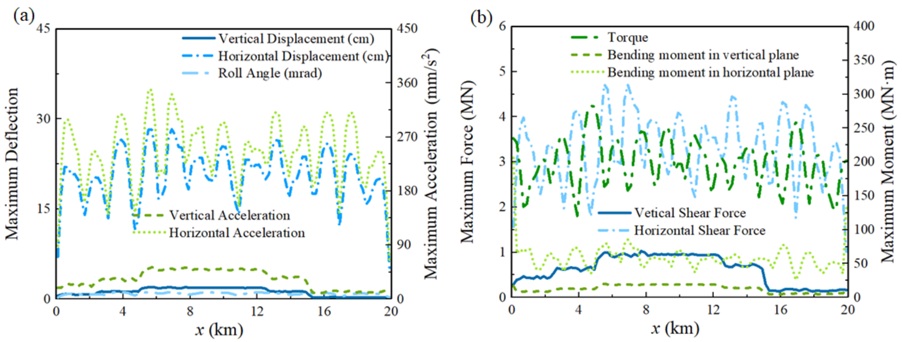

Figure 5.22: (a) Envelopes of the IL displacement under the extreme event; (b) Envelopes of internal forces under the extreme event

5.6. STRUCTURE CONFIGURATION OPTIMIZATION

5.6.1. SFT CONFIGURATION OPTIMIZATION PROCESS

Structural optimization has great potential for the engineering design and construction industry. The main objectives of structural optimization are to satisfy a set of constraints (e.g., improve the structural physical and mechanical properties, mitigate the potential uncertainties, risks and structural failure, increase structural sustainability and reliability, and save construction costs) by tuning certain structural parameters. Generally, structural optimization strategies are categorized into size optimization, shape optimization, and topology optimization (Dillen et al. 2021). Size optimization focuses on the optimal dimensions of the structural components and can be exemplified by determining the optimal aspect ratio of the SFT cross-section. Shape optimization where the shape of the structure is parameterized is to optimize the parameter combinations. A typical application in SFT is to optimize cross-section shape. The topology optimization is to determine the optimal spatial distribution of structural components, i.e. to determine the optimal SFT structure configuration which minimizes the global structural dynamic response to hydraulic loading. The size and shape optimization have been studied in Chapter 2. Therefore, in this chapter, mainly topology optimization of the SFT is discussed.

The structural configuration optimization scheme can be formulated as Eq.5.13.

$$\begin{cases} \min f(x) \\ \text{subject to } h(x) = 0, g(x) \leqslant 0, x \in X \subseteq R^n \end{cases} \tag{5.13}$$

where $f(x)$ is objective function; $h(x)$ and $g(x)$ are equality and inequality constraints, respectively; X is set constraint that includes additional restrictions on design variable x.

For SFT configuration optimization, structural parameters, basically categorized as the tunnel tube parameters, joint parameters, and mooring-related parameters, are formulated as discrete design variables. The constraints can involve limits of design variables (e.g., strait width, water depth, topography at the SFT construction site, structure material) and hydrodynamic loads such as waves, currents, extreme events, and internal waves. The main objective is to minimize the global dynamic response of the SFT under various environmetal conditions. The associated quantities should be examined, such as reducing the maximum internal forcing and motion response. The structural natural frequencies should be tuned outside the local hydrodynamic loading frequency range to avoid FIV, which is determined by structural parameters and global configuration of the SFT system. Thus, the topology optimization problem in this research can be determined as Eq. 5.14.

$$\min f = (F_{max}, M_{max}, \delta_{max}) \tag{5.14}$$

where F and M are the internal force and moment of the SFT; δ is the structural motion displacement.

This optimizing process is generated by outer and inner loops. For the outer loop, the representative hydrodynamic load (e.g., typical wave conditions, extreme events) is selected, and dynamic response of the SFT and FIV condition for the given hydrodynamic load are examined, and following the same procedure, the worst case scenario can be determine. For the inner loop, a sensitivity analysis should be required by tuning few design variables to alter structural natural frequency which alleviate resonance. However, it is a complex systematic optimization problem related to uncertainties such as hydrodynamic loads and structural parameters. Regarding a long span structure as an SFT, spatiotemporal variation and randomness of hydrodynamic loading along the tunnel span are essential to be considered. The CFD, as the most comprehensive numerical simulation approach for fluid dynamics, is insufficient and hardly implemented to simulate the stochastic waves varying along the span in a large domain. Therefore, multiscale models are established to solve large-scale oceanographic hydraulic loading and small-scale hydrodynamic forcing on structures, respectively. For a given hydrodynamic condition, an initial SFT configuration is assumed and dynamic response of the SFT and FIV conditions are computed using FEM. The natural frequency of the SFT is determined by structural configuration and can be regarded as a function of structural parameters. A sensitivity analysis of structural parameters can lay a foundation for FIV predictions and optimal SFT configuration determination. The condition for suppression or avoidance of synchronization for the SFT can be realized by modifying the structural rigidity of the SFT and hence, tuning the natural frequencies to stabilized the system. After tuning structure parameters, dynamic response of the SFT and FIV conditions need to be further examined. Therefore, a dynamic process of SFT configuration optimization can be established. The proposed SFT configuration optimization framework is shown in Fig.5.23.

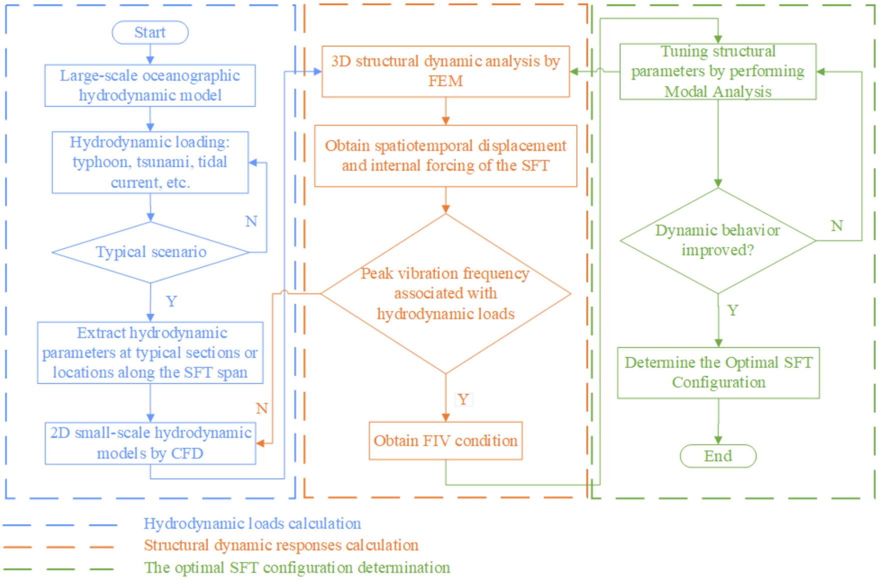

Figure 5.23: SFT configuration optimization framework

5.6.2. SENSITIVITY ANALYSIS OF STRUCTURAL PARAMETERS

In order to reduce dynamic response of the SFT, the structural natural frequencies should be tuned outside the local hydrodynamic loading frequency range by selecting the optimal SFT configuration. Since the natural frequency of the SFT system is determined by its structural configuration, basically categorized as the tunnel tube parameters, joint parameters, and mooring-related parameters, the influence of these structural variables on dynamic performance should be carried out by modal analysis. The tunnel tube parameters affect the structural modes mainly include BWR, element and overall length of the SFT, structure alignment, and cross-section shape; joint parameters include joint stiffness and shore connections; while mooring-related parameters are composed of mooring line property, inclination angle, and mooring spacing and configuration. In the sensitivity analysis procedure, it notes that the selection of the iterative spacing step of design variables is important for the structural optimization. The design estimates selection based on the local behavior of the cost function and constraints affects the optimization results. However, for a complex structure with multiple components such as an SFT, it is important to conduct the sensitivity analysis procedure as efficiently as possible for a general qualitative understanding and a broad structural configuration optimization concept. Therefore, detail sensitivity analysis and optimization algorithms for a concert engineering case are not addressed in this chapter.

The FEM model is established with the initial spring stiffness k_0 of $5 \times 10^8\,\mathrm{N\,m^{-2}}$, SFT tube length of 900 m, element length of 100 m, circular cross-section shape, fixed end connection, mooring configuration Type 1 (Fig.5.24), and mooring spacing of 100 m as a basic case, but in the element length analysis, the overall tunnel length is 1200 m.

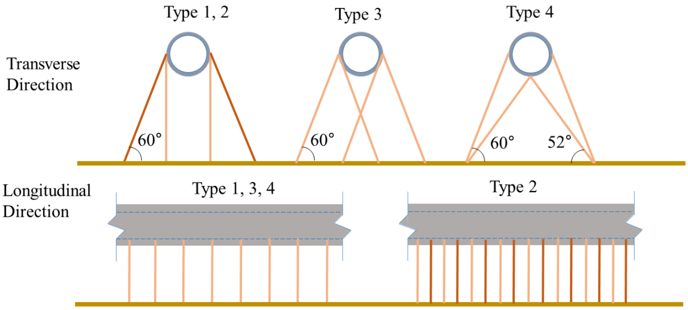

Figure 5.24: Mooring configurations sketch (mooring interval: Type 1, 3, 4: 100 m; Type 2: 50 m)

The variations of mode frequencies of the SFT versus influential factors are shown in Fig.5.25 and Fig.5.26. Basic findings can be listed: the initial spring stiffness k_0 of Gina gasket is recommended larger than $5 \times 10^8\,\mathrm{N\,m^{-2}}$ to maintain the SFT system stability for engineering application (Fig.5.25 (a)). Structural natural frequencies slightly increase with increasing BWR (Fig.5.25 (b)). For a tunnel length exceeds 2000 m, the first several horizontal and vertical mode frequencies are generally remain constant, and the close-by frequencies make the possibility of multi-mode response increases. The axial stiffness should be noteworthy and carefully scrutinized for a tunnel with thousands of lengths (Fig.5.25 (c)). It is speculated that the tunnel element length and cross-section shape are not key factors to horizontal and vertical natural frequencies (Fig.5.25(d) and (f)). The horizontal natural frequencies can be increased by adopting the horizontal structural curved alignment (Fig.5.25 (e)).

The fixed-end connection generally attains the highest frequencies. The hinged condition and one-end free condition show low torsional and axial frequencies, respectively. Moreover, one-end free condition provides the lowest horizontal stiffness which should be scrutinized during the transportation and installation process (Fig.5.26 (a)). The mooring configuration with two single pile foundations symmetrically tying four inclined lines in each group (Type 4, see Fig.5.24) can increase the horizontal fundamental frequencies to some extent, while saves the usage of pile foundations, and alternating mooring configuration scheme shows no clear advantages in structural dynamic response (Fig.5.26 (b), Fig.5.24). Structural natural frequencies (except for axial mode) can be effectively increased by decreasing mooring longitudinal spacing (Fig.5.26 (c)). A mooring inclination angle of 45° can balance well the structural vibration with the construction cost, which is recommended in engineering practice (Fig.5.26 (d)).

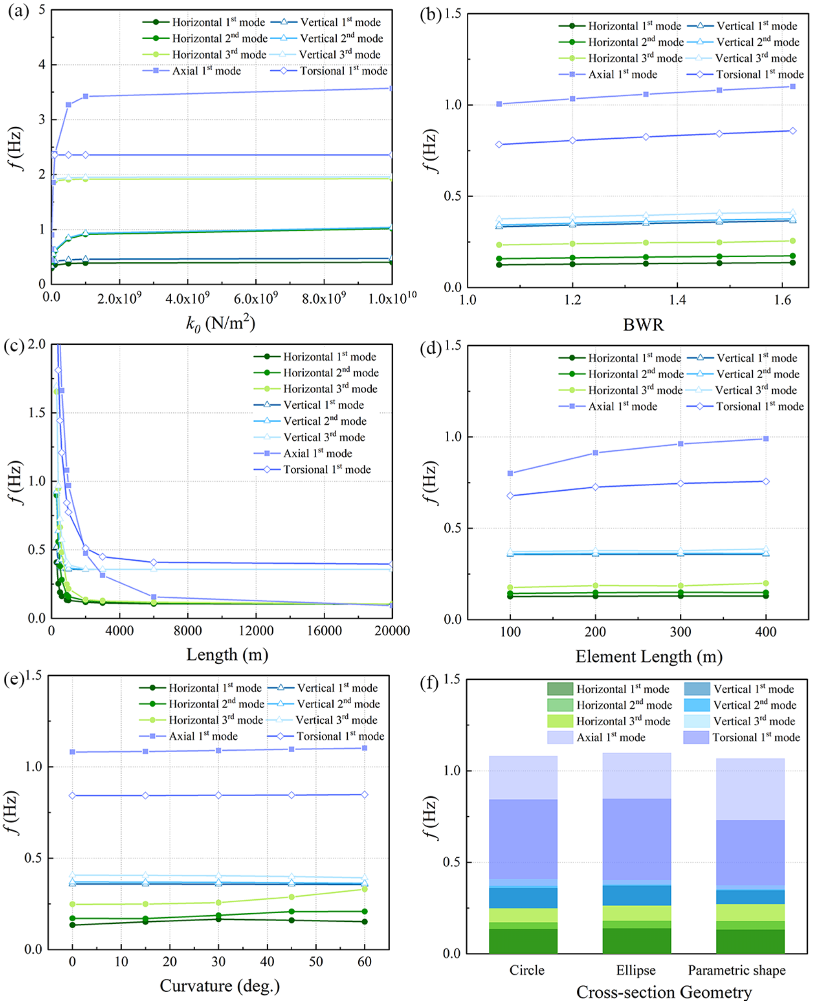

Figure 5.25: Variation of natural frequencies with structural parameters (a)

As per the achievements from the sensitivity analysis, the structural horizontal stiffness, as a relatively vulnerable spot in the SFT system, can be enhanced by taking the concrete measurements such as element joints with high stiffness, a large BWR, a reasonably curved SFT longitudinal alignment, a short span SFT, a rigid shore connection, and a reduced mooring spacing. In this way, a smart and dynamic SFT configuration optimization procedure can be established by tuning structural parameters for the suppression or avoidance of synchronization under a certain hydrodynamic loading condition.

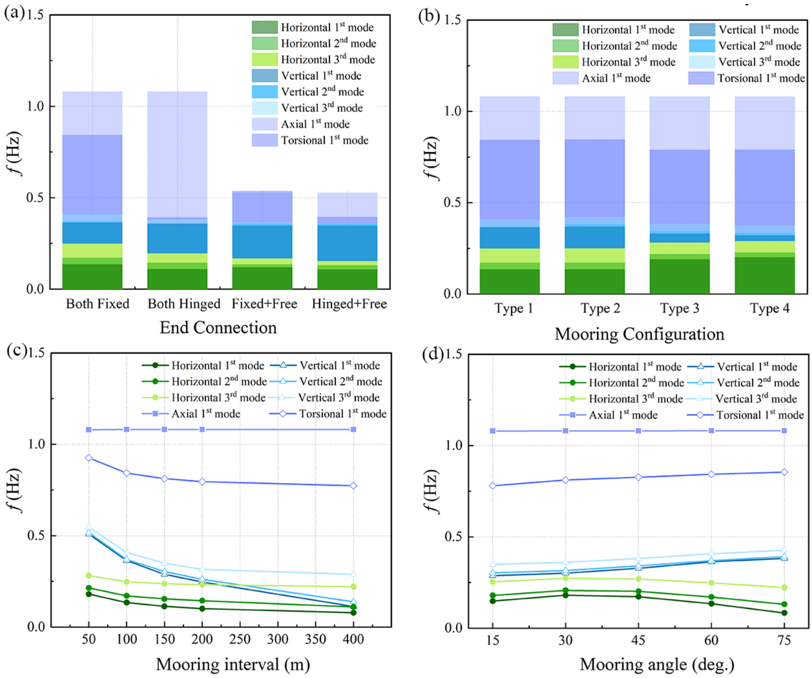

Figure 5.26: Variation of natural frequencies with structural parameters (b)

5.7. CONCLUSION

In this chapter, a pragmatic one-way FSI approach consisting of a multi-scale cascade of hydrodynamic models combined with FEM are proposed to consider the spatiotemporal variation and randomness of hydrodynamic loading. Steel shell concrete composite material is proposed for the SFT tube, and stiffness properties of a tunnel joint composed of a Gina gasket and shear keys are quantified. A prototype super long and large aspect ratio SFT numerical model composed of a coupled tube-joint-mooring system is established for FIV prediction and global dynamic response analysis in the time-domain. The dynamic response and FIV predictions of an SFT with parametric and a circular cross section shapes are compared under steady currents and waves. The structural motion response and dynamic forcing of a super-long SFT are assessed under extreme events and oceanic ISW conditions. A sensitivity analysis of structural parameters is performed to modify the fundamental frequency outside the hydrodynamic frequency, and a structural configuration optimization process to avoid the resonant period of the structural primary modes coincide with the hydrodynamic frequency is established. The main conclusions are briefly summarized as follows:

- The spatiotemporal variation and randomness of hydraulic loading can be effectively solved by multi-scale models including a large-scale oceanographic (shallow water equation) model and a small-scale hydrodynamic forcing (CFD) model.

- The SFT tube is unlikely to experience strong resonance under steady currents, due to its large cross-section dimension. FIV of the SFT tube is mainly dominated by wave conditions. Wave effects on FIV of the SFT are complex. A single dominant mode excitation of the tube with a large wave height and period should be avoided.

- An SFT with a parametric cross-section shape is recommended over the simpler circular shape due to the effectively reduced hydrodynamic forcing and structural dynamic response of the parametric cross-section.

- The deflections and accelerations of the SFT under the ISW are far smaller than the typhoon case. As the ISW is a long wave, its frequency is much lower than the natural frequency of the SFT tube. Therefore, resonance of the tunnel tube under ISW conditions becomes unlikely. Due to BWR change during the ISW evolution, a large shear force and bending moment on the SFT may occur, which affects the tension force in the mooring lines, and can threaten the safety and reliability of the SFT system. In the typhoon scenario, The large bending moment and torque may occur at shore connections, where structure fatigue and buckling failure should merit attention.

- The structural axial stiffness is mainly affected by BWR, tunnel length, element length, and joint and shore connection properties, while the torsional stiffness is also influenced by mooring parameters. The super long structure with thousands meter length is subject to multi-modes response, and one end free scenario should be scrutinized during transportation and installation process.

- A dynamic process for SFT configuration optimization is proposed by smartly tuning the fundamental frequencies for the suppression or avoidance of synchronization under a certain hydrodynamic loading condition.

In spite of these achievements for the FIV prediction and dynamic response analysis of the SFT, some restrictions and future work still should be noted in this study.

- Flow-induced vibration conditions are studied under uniform currents and regular waves. In reality, the SFT will be subject to inhomogeneous irregular waves and unsteady currents. Therefore as a future step, the dynamic response of the SFT should also be examined based on such realistic environmental conditions.

- Hydraulic loading computation based on the framework of two-dimensional flow strips conserves computational resources, but is limited by incapability of accounting for complex three-dimensional effects, axial pressure gradients, or oblique flows.

- Hydrodynamics of the SFT is a multi-physics issue with a strong interaction between the flow field and tunnel tube. It is rational to assume the flow is not heavily affected by small structural deformations of an SFT at this stage. However, the importance of this effect should be quantified in future research.

APPENDIX

The stiffness of pitch and yaw motions of the SFT tube can be modelled as rotation springs, and mainly be determined by the Gina gaskets property and cross-section dimensions. The derivation process of bending stiffness of Gina gasket with a circular tubular shape in horizontal and vertical directions is shown as follows:

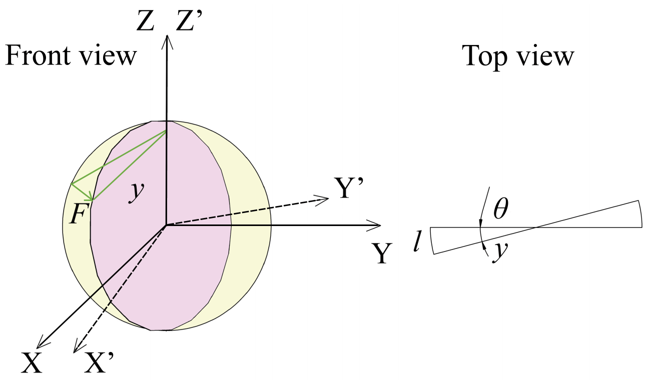

Figure 5.27: Bending stiffness derivation

Assumed that the yellow circular arc represents the original Gina gasket (XYZ coordinate system), and a small rotational angle θ of Gina gasket takes place due to an external bending force, and the pink circular arc represents the transformed Gina gasket (X'Y'Z' coordinate system). y is the distance between a certain point along the Gina gasket and the rotation axis, and l is the displacement of that point after the rotation, expressed as Eq.5.15

$$l = y\theta \tag{5.15}$$

The compression force F at that point provided by Gina gasket can be expressed as Eq.5.16

$$F = k_0 l \tag{5.16}$$

where k_0 is the initial spring stiffness of Gina gasket.

The total compression along the Gina gasket can be derived in Eq.5.17

$$F_{total} = \oint F ds = \oint k_0 y\theta ds \tag{5.17}$$

Assume y=$r\cos t$; z=$r\sin t$, where r is the radius of Gina gasket. Therefore, ds can be formulated in Eq.5.18

$$ds = \sqrt{(y_t')^2 + (z_t')^2} dt = r dt \tag{5.18}$$

Therefore, the total compression provided by Gina profile is calculated using Eq.5.19

$$F_{total} = 4\int_0^{\frac{\pi}{2}} k_0\theta r^2 \cos t dt = 4\pi k_0\theta r^2 \tag{5.19}$$

For the bending moment at a certain point can be expressed as Eq.5.20

$$M = Fy \tag{5.20}$$

Similarly, the total bending moment along the Gina gasket can be derived in Eq.5.21

$$M_{total} = \oint M ds = \oint k_0 y^2 = 4\int_0^{\frac{\pi}{2}} k_0 \theta r^2 \cos^2 t \cdot r dt = \pi k_0 \theta r^3 \tag{5.21}$$

Thus, the bending stiffness of Gina gasket can be derived as Eq.5.22

$$k_\theta = \frac{M_{total}}{\theta} = \pi k_0 r^3 \tag{5.22}$$

REFERENCES

Aashto (2010), *AASHTO LRFD Bridge Design Specifications.*

ANSYS, F. (2019), ‘ANSYS fluent theory guide 19.1’, *ANSYS, Canonsburg, PA* .

Benra, F. K., Dohmen, H. J., Pei, J., Schuster, S. & Wan, B. (2011), ‘A comparison of one-way and two-way coupling methods for numerical analysis of fluid-structure interactions’, *Journal of Applied Mathematics* .

Chen, M., Chen, J. & You, Y. X. (2020), ‘Forces on a semi-submersible in internal solitary waves with different propagation directions’, *Ocean Engineering* .

Chen, W., Li, M., Zhang, L. & Tan, T. (2016), ‘Study on multimode vortex-induced vibration of deepwater riser in different flow fields by finite element simulations’, *Journal of Offshore Mechanics and Arctic Engineering* .

Chen, W., Li, Y., Fu, Y. & Guo, S. (2016), On Mode Competition during VIVs of Flexible SFT’s Flexible Cylindrical Body Experiencing Lineally Sheared Current, *in* ‘Procedia Engineering’.

Chen, Z., Xiang, Y., Lin, H. & Yang, Y. (2018), ‘Coupled vibration analysis of submerged floating tunnel system in wave and current’, *Applied Sciences (Switzerland)* .

Cruz, C. & Miranda, E. (2017), ‘Evaluation of the Rayleigh damping model for buildings’, *Engineering Structures* **138**.

Deng, S., Ren, H., Xu, Y., Fu, S., Moan, T. & Gao, Z. (2020), ‘Experimental study of vortex-induced vibration of a twin-tube submerged floating tunnel segment model’, *Journal of Fluids and Structures* .

Dillen, W., Lombaert, G. & Schevenels, M. (2021), ‘A hybrid gradient-based/metaheuristic method for Eurocode-compliant size, shape and topology optimization of steel structures’, *Engineering Structures* **239**.

Duanmu, Y., Zou, L. & Wan, D. (2018), ‘Numerical analysis of multi-modal vibrations of a vertical riser in step currents’, *Ocean Engineering* .

Felisita, A., Gudmestad, O. T., Karunakaran, D. & Martinsen, L. O. (2016), A review of VIV responses of steel lazy wave riser, *in* 'Proceedings of the International Conference on Offshore Mechanics and Arctic Engineering - OMAE'.

Govardhan, R. & Williamson, C. H. (2000), 'Modes of vortex formation and frequency response of a freely vibrating cylinder', *Journal of Fluid Mechanics* .

Hong, Y. & Ge, F. (2010), Dynamic response and structural integrity of submerged floating tunnel due to hydrodynamic load and accidental load, *in* 'Procedia Engineering'.

Hydraulics, D. (2006), 'Delft3D-FLOW user manual', *Delft, the Netherlands* .

il Seo, S., suk Mun, H., ho Lee, J. & ha Kim, J. (2015), 'Simplified analysis for estimation of the behavior of a submerged floating tunnel in waves and experimental verification', *Marine Structures* .

Jiang, B., Liang, B., Faggiano, B., Iovane, G. & Mazzolani, F. M. (2018), Feasibility study on a submerged floating tunnel for the Qiongzhou strait in China, *in* 'Maintenance, Safety, Risk, Management and Life-Cycle Performance of Bridges - Proceedings of the 9th International Conference on Bridge Maintenance, Safety and Management, IABMAS 2018'.

Jin, C., Kim, J. M.-H., Choi, J. & Park, W.-S. (2018), Coupled dynamics simulation of submerged floating tunnel for various system parameters and wave conditions, *in* 'International Conference on Offshore Mechanics and Arctic Engineering', Vol. 51265, American Society of Mechanical Engineers, p. V07AT06A050.

Kamphuis, J. (1998), 'Hydrodynamics around cylindrical structures', *Coastal Engineering* .

Kavanagh, K., Dib, M., Balch, E. & Stanton, P. (2002), New Revision of Drilling Riser Recommended Practice (API RP 16Q), *in* 'Proceedings of the Annual Offshore Technology Conference'.

Kimura, H., Moritaka, H. & Kojima, I. (2002), 'Development of sandwich-structure submerged tunnel tube production method', *Nippon Steel Technical Report* .

Koglin, T. L. (2003), *Movable Bridge Engineering*.

Kunisu, H. (2010), Evaluation of wave force acting on Submerged Floating Tunnels, *in* 'Procedia Engineering'.

Larssen, R. M. & Jakobsen, S. E. (2010), Submerged floating tunnels for crossing of wide and deep fjords, *in* 'Procedia Engineering'.

Li, Y., Song, S. & Liu, Y. (2020), 'Steel web effects on shear mechanism of steel shell-concrete composite structure', *Engineering Structures* .

Lin, H., Xiang, Y. & Yang, Y. (2019), 'Vehicle-tunnel coupled vibration analysis of submerged floating tunnel due to tether parametric excitation', *Marine Structures* .

Lin, H., Xiang, Y., Yang, Y. & Chen, Z. (2018), 'Dynamic response analysis for submerged floating tunnel due to fluid-vehicle-tunnel interaction', *Ocean Engineering* **166**, 290–301.

Lin, K. & Wang, J. (2019), 'Numerical simulation of vortex-induced vibration of long flexible risers using a SDVM-FEM coupled method', *Ocean Engineering* .

Liu, G., Li, H., Qiu, Z., Leng, D., Li, Z. & Li, W. (2020), 'A mini review of recent progress on vortex-induced vibrations of marine risers'.

Liu, M. & Gorman, D. G. (1995), 'Formulation of Rayleigh damping and its extensions', *Computers and Structures* **57**(2).

LTD, F. E. A. (n.d.), 'LUSAS user manual'.

Lwin, M. M. (2000), 'Floating bridges', *Bridge engineering handbook* **22**, 1–23.

Manual, O. (2014), 'Version 9.8 b', *Orcina Ltd* .

Martire, G., Faggiano, B., Mazzolani, F. M., Zollo, A. & Stabile, T. A. (2010), Seismic analysis of a SFT solution for the Messina Strait crossing, *in* 'Procedia Engineering', Vol. 4.

Passano, E., Larsen, C. M., Lie, H. & Wu, J. (2014), 'VIVANA theory manual', *Norwegian Marine Technology Research Institute: Trondheim, Norway. Current profiles with higher velocities produce high damage at both the riser's upper catenary and buoyancy section due to high current exposure at the shallower water depth and the high c* .

Remseth, S., Leira, B. J., Okstad, K. M., Mathisen, K. M. & Haukås, T. (1999), 'Dynamic response and fluid/structure interaction of submerged floating tunnels', *Computers and Structures* **72**(4).

Roeber, V. & Bricker, J. D. (2015), 'Destructive tsunami-like wave generated by surf beat over a coral reef during Typhoon Haiyan', *Nature Communications* .

Tariverdilo, S., Mirzapour, J., Shahmardani, M., Shabani, R. & Gheyretmand, C. (2011), 'Vibration of submerged floating tunnels due to moving loads', *Applied Mathematical Modelling* .

Ulveseter, J. V., Thorsen, M. J., Sævik, S. & Larsen, C. M. (2018), 'Time domain simulation of riser VIV in current and irregular waves', *Marine Structures* .

Van Oorsouw, R. S. (2010), 'Behaviour of segment joints in immersed tunnels under seismic loading'.

Vandiver, J. K. & Li, L. (2005), 'Shear7 V4. 4 program theoretical manual', *Massachusetts Institute of Technology* .

Wijesooriya, K., Mohotti, D., Amin, A. & Chauhan, K. (2020), 'An uncoupled fluid structure interaction method in the assessment of structural responses of tall buildings', *Structures* .

Wu, X., Ge, F. & Hong, Y. (2010), Effect of travelling wave on vortex-induced vibrations of submerged floating tunnel tethers, *in* 'Procedia Engineering'.

Wu, X., Ge, F. & Hong, Y. (2012), 'A review of recent studies on vortex-induced vibrations of long slender cylinders', *Journal of Fluids and Structures* .

Xiao, J. & Huang, G. (2010), Transverse earthquake response and design analysis of submerged floating tunnels with various shore connections, *in* 'Procedia Engineering'.

Yan, H., Zhang, F. & Yu, J. (2016), The Lectotype Optimization Study on Submerged Floating Tunnel Based Delphi Method, *in* 'Procedia Engineering'.

Zhang, K., Xiang, Y. & Du, Y. (2010), Research on tubular segment design of submerged floating tunnel, *in* 'Procedia Engineering'.

Zhang, Y., Habashi, W. G. & Khurram, R. A. (2015), 'Predicting wind-induced vibrations of high-rise buildings using unsteady CFD and modal analysis', *Journal of Wind Engineering and Industrial Aerodynamics* .

Zou, P., Bricker, J. D., Chen, L., Uijttewaal, W. S. & Simao Ferreira, C. (2022), 'Response of a submerged floating tunnel subject to flow-induced vibration', *Engineering Structures* **253**, 113809.

Zou, P., Bricker, J. D. & Uijttewaal, W. (2021), 'The impacts of internal solitary waves on a submerged floating tunnel', *Ocean Engineering* **238**, 109762.

Zou, P., Bricker, J. & Uijttewaal, W. (2020*a*), 'Impacts of extreme events on hydrodynamic characteristics of a submerged floating tunnel', *Ocean Engineering* **218**.

Zou, P., Bricker, J. & Uijttewaal, W. (2020*b*), 'Optimization of submerged floating tunnel cross section based on parametric Bézier curves and hybrid backpropagation - genetic algorithm', *Marine Structures* .

6

CONCLUSIONS AND RECOMMENDATIONS

This thesis has addressed dynamic response of the submerged floating tunnel subject to hydraulic loading, including identification of hydrodynamic loads, analysis of structural dynamic response, and structural optimization. The findings enhance the understanding of hydrodynamic forces acting on a submerged floating tunnel, providing reference for assessment of the impact of these loads on the SFT, and contributing to further structure reliability and safety assessment for the SFT concept. The broader impact of this research is to guide SFT system design at potential construction sites worldwide and contribute to further understanding the mechanism of interaction between large-scale floating offshore structures and complex hydrodynamic loads.

This chapter presents the overall conclusions of this thesis (Section 6.1), detailed findings of each chapter (Section 6.2), limitations of the current research (Section 6.3), and recommendations for follow-on research (Section 6.4).

6.1. MAIN FINDINGS

The main objective of this thesis was to comprehend the interactions of a submerged floating tunnel (SFT) with the variety of hydrodynamic loads expected. The conclusions of this thesis refer to how different hydrodynamic loads affect structural forcing, and how to construct and implement structural optimization methods to minimize hydrodynamic loading and structural response. The main findings are summarized below.

1. SFTs are subject to marine environmental conditions generally including currents, waves, internal waves, and extreme hydraulic events (e.g. tsunamis and super typhoons). Relevant research about the impacts of hydrodynamic loads on SFT's motion (e.g. sway, heave, and roll displacements and accelerations) and mooring force temporal distribution (e.g. slack risk analysis) and the influences of the structural parameters on them are important for the reliability and safety design of an SFT. Prior research has addressed some of these issues, but results are not yet sufficient to understand critical loading. Furthermore, the flow-induced vibration issue of the SFT is another crucial factor affecting the safety, reliability, and lifetime of the SFT. Therefore, in this thesis, research of the hydrodynamic load impacts on the SFT focus on the global dynamic response of the SFT (e.g. internal forcing, structural deflection and vibration, etc.), especially vibration issues. In addition, the dynamic behaviour of the SFT under extreme loading was specially addressed in this thesis. The impacts of each type of hydrodynamic load on the SFT have been numerically analyzed and discussed by using CFD and the finite element method (FEM).

   - For steady current conditions, as the current flows over the SFT tube and mooring lines, an unsteady pressure field over the surface and the shedding of an unsteady wake can be generated. If oscillatory flow occurs and synchronizes with one of the structural natural frequencies, the oscillation amplitude of the SFT amplifies, leading to vortex-induced vibration (VIV). The vibration amplitude of the SFT tube increases with increasing current speed. However, due to the large tunnel cross-sectional dimensions applied, the reduced velocities of the SFT tube under the given steady current conditions are rather low, and hence, a notable resonance phenomenon is unlikely to occur. Nevertheless, the reduced velocity can vary within a wide range and may overlap the lock-in region for mooring cables, which has been extensively investigated in previous works.
   - Unlike the generally current-dominated situation for marine risers, flow-induced vibration (FIV) of the SFT tube is more critical under wave conditions than steady current conditions. The SFT tube oscillation amplitude in the in-line direction (parallel to the wave propagation direction) is much larger than in the cross-flow direction (heave) due to the comparatively weaker stiffness provided in the in-line direction. Therefore, the response motion of the SFT along the wave propagation direction is more severe, which should be especially focused on. The surface wave loads acting on the tube and the oscillation amplitude of the SFT increase with increasing wave height, whereas the

impact of wave period on the SFT is complex. The structural response amplitude can be amplified by a single dominant mode excitation under a large wave height and period scenario, where measures should be taken to suppress or avoid severe resonance. For a super long SFT, multi-mode responses are observed.

- Internal wave with stratification interface near the SFT submergence depth can act directly on the SFT tube, and can cause severe impacts and safety issues. The hydrodynamic forces on the SFT tube increase with increasing internal solitary wave (ISW) amplitude, and strong ISW-SFT interaction and severe energy dissipation can be observed at large ISW amplitude conditions. The buoyancy change induced by the ISW evolution can remarkably alter the BWR (buoyancy - weight ratio) of the SFT, causing strong interactions between the ISW and structure, and leading to large shear forces and bending moments on the SFT tube. These effects threaten the safety and reliability of the SFT system which should be carefully examined in the engineering design phase. However, the resonance of the tunnel tube becomes unlikely under the applied ISW condition due to its rather low intrinsic frequency.
- Extreme hydraulic events in marine and coastal zones exacerbate structural vulnerability, and the impacts on the SFT were assessed. In the tsunamic scenario, the unsteady current speed and inflow acceleration can change dramatically, and hence, may cause large drag and inertial forces on the SFT compared with the local astronomical tide, jeopardizing the SFT structure and mooring system. Since a tsunami is unsteady, inertia can play an important role in the in-line force on the SFT. However, in the typhoon scenario, the wave and current provide an approximately equal contribution to the in-line force, whereas the waves play a dominant role in the lift. A large bending moment and torque can occur at the shore connections, where structure fatigue and buckling failure should merit attention.

Hydrodynamic loads affect the structural dynamic response. In addition, structural configuration is another influential factor to dynamic response. The large hydrodynamic forcing on the SFT can be reduced by tuning the structural parameters. For instance, in this thesis, the influence of cross-sectional shape on the hydrodynamic forcing on the SFT was analyzed and elucidated in detail. Furthermore, the hydrodynamic loads impacts on the SFT can be changed by modifying the fundamental frequencies of the structure, which is regarded as an effective way to suppress or avoid SFT resonance.

- This thesis proposed a parametric shape for the SFT cross-section using Bezier curve profiles. The hydrodynamic performance of the parametric shape was compared with simpler shapes such as circular and elliptical shapes under various hydrodynamic load conditions (e.g. waves, current, internal wave, and extreme hydraulic events). Compared with other simpler shapes, for steady current conditions, the oscillation amplitudes in both in-line and cross-flow directions of the SFT can be effectively reduced by adopting the parametric shape. For the wave conditions, the in-line response of the SFT can be effectively reduced by using the parametric shape. The parametric shape with its most streamlined SFT cross-section geometry, experiences reduced flow separation and vortex shedding, and hence, results in the minimum hydrodynamic forcing on the SFT under both internal wave and extreme hydraulic event conditions. Furthermore, in the tsunami scenario, vortex shedding is limited to a shorter time period and lower amplitude by using the parametric shape. Therefore, in general, this thesis concluded that the proposed parametric shape SFT cross-section shows better hydrodynamic performance than simpler shapes.

- For a coupled SFT tube-joint-mooring system, mooring lines and tethers provide sufficient vertical stiffness in the vertical plane, and additionally, ballast adjustment can contribute to balance the vertical loads. However, inclined mooring lines are needed to provide horizontal stiffness to the SFT system to resist the hydrodynamic loads. Thus, the structural horizontal stiffness, as a relatively vulnerable spot in the SFT system, should be enhanced. By conducting a sensitivity analysis of structural parameters, this thesis proposed several concrete measures to increase the horizontal fundamental frequencies for the global system: an SFT with a short span, a curved SFT longitudinal alignment, element joints and shore connections with high stiffness, a reduced mooring interval, etc. In addition, conclusions that can provide reference to the engineering practice are: an inclined mooring angle of 45° can balance well the structural vibration with the construction cost, and the mooring configuration with four inclined lines in each group can increase the horizontal fundamental frequency to some extent.

In summary, dynamic response of a submerged floating tunnel is determined by hydrodynamic loads and structure configuration properties, and more importantly, the interactions and mutual effects among them. Despite the hydrodynamic forcing on the SFT and the specific impacts on the SFT that vary with the selected environmental conditions, the applied research methods and achieved general conclusions in this thesis help to better understand the different types of hydrodynamic impacts on the SFT and contribute to further structure reliability and safety assessment for the SFT concept. This can provide guidance for the SFT system at other potential application sites in the world and shed light on better design of other offshore floating moored structures.

2. Structural optimization is a crucial process in the engineering design and construction industry to improve the physical and mechanical properties of a structure. The main objectives of structural optimization are to satisfy a set of constraints by tuning certain structural parameters. Three types of structural optimization strategies were carried out in this thesis: size optimization, shape optimization, and topology optimization, which are exemplified by the optimization of cross-sectional aspect ratio, cross-sectional geometry, and global structural configuration. Different variables, constraints, and cost functions are defined for different optimization strategies.

- In the size optimization problem, the aspect ratio of the SFT cross-section described by different types of parametric Bezier curves was defined as the design variable, cross-sectional clearances or dimensions based on technical guidelines were defined as constraints, and the dynamic performance (e.g. drag force) and construction cost (e.g. the perimeter of the cross-section) of the SFT cross-section were defined as the optimization functions.

- In the shape optimization problem, the SFT cross-sectional geometry was described by a parametric curve function (i.e. Bezier-PARSEC curve). Bezier-PARSEC curve parameter combinations were defined as design variables; the variable constraints can be defined by cross-sectional dimensions (or clearances) and the intrinsic constraints of the Bezier-PARSEC curves, and the optimization objectives were to minimize the hydrodynamic loads on the SFT (e.g. mean drag and RMS lift).

- In the topology optimization problem, discrete structural variables include tunnel tube parameters (e.g. BWR, element and overall length of the SFT, and structure alignment), joint parameters (e.g. joint stiffness, shore connection), and mooring-related parameters (e.g. mooring line stiffness, inclination angle, spatial spacing, and mooring arrangement) were defined as design variables. The constraints involved multiple hydrodynamic loads such as waves, currents, extreme hydraulic events, and internal waves; and the optimization functions were defined by the SFT dynamic response quantities such as natural frequencies, internal forcing, and deflection.

According to different design, usage, and precision requirements, the optimization approach can be determined differently. Sensitivity analysis with its efficiency and generality has been extensively applied in the structural optimization process. As a more advanced structural optimization approach, machine learning tools such as Artificial Neural Network (ANN) have been widely employed to resolve complex physical processes across various disciplines and have shown good properties in nonlinearity prediction. This thesis showed the reliable performance of an ANN in the cross-section shape optimization for an SFT. Furthermore, unlike the need for time-consuming CFD simulations, due to the powerful learning capacity of the machine learning approach, an ANN is an effective way to bridge the gap between simulation efficiency and accuracy. For a complex optimization problem such as the global configuration of the SFT which involves multiple structural components (i.e., the tunnel tube, joint, and mooring system), the structural optimization process can be generated by multiple iterations, where the most influential constraints (e.g. the most disastrous hydrodynamic load) and the major design variables (e.g. structural parameters that can effectively alter the natural frequencies of the SFT) should be determined.

In this thesis, the structural optimization of an SFT regarding the cross-sectional aspect ratio, shape, and structural configuration was described and documented. The optimization procedure and methods can be extended and integrated into other optimization problems for the SFT or other type of infrastructures.

6.2. DETAILED FINDINGS

6.2.1. SFT CROSS-SECTION OPTIMIZATION

In order to optimize the SFT cross section for hydrodynamic performance, the amplitude of oscillation of the lift and the mean drag on the SFT, should be reduced. This thesis has proposed a parametric shape for the SFT cross-section using two types of Bézier curve profile with a combination of parameters such as b, r, y. It derived that a symmetrical cross-sectional shape on both upper and lower surfaces with equal b (i.e., $b_{up} = b_{low}$) can effectively minimize the root mean square lift force on the SFT. An appropriate decrease of the leading edge radius of the parametric shape can achieve a better hydrodynamic performance for an SFT, while a shape with a sharp leading edge and apex should be avoided due to exacerbation of flow detachment. By comparing the hydrodynamic performance of the shapes described by the leading-edge BP curve and the trailing-edge BP curve under the same unsteady current conditions and equal aspect ratio, the apex of the trailing-edge BP curve is sharper and less streamlined as cross-sectional height increases. The bluffer shape described by the trailing-edge BP curve results in the streamflow passing the apex, detaching from the surface, and forming a large wake of recirculating flow, which increases the in-line force. Additionally, a reasonable aspect ratio was determined by comparing the hydrodynamic performance and perimeter of the two types of SFT cross-sectional shapes. The SFT cross-section with aspect ratio of 0.47 using the leading-edge BP curve under the given clearance appears the best option with a balanced consideration of hydrodynamic performances and construction cost.

In order to predict the optimal cross-sectional shape for the SFT, the thesis provided an applicable structure optimization method associated with hydraulic engineering practice, which is an artificial neural network (ANN) method using a backpropagation learning algorithm with benefits from combination with a GA (hybrid BP-GA structure). The SFT cross section with the Bézier curve parameter combination of $b_{up} = b_{low} = 1$ m; $r = 3$ m; $y_{up} = y_{low} = 2.5$ m shows an optimized hydrodynamic performance based on the prediction of the ANN method. The ANN can be used to deal with the expected high nonlinearity of the relationships and thus can be an effective tool to optimize the complex interdependency of Bézier curve parameters. This data-driven machine learning method reduces the need for time-consuming CFD analyses, increasing the efficiency, reliability, and goodness of prediction of the SFT cross section design.

6.2.2. INTERNAL WAVE IMPACTS

The assessment of the hydrodynamic performance of the SFT subject to internal waves is inherently a fluid-structure interaction problem. The mechanism of interaction between the ISW and the SFT is revealed by elucidating the velocity field around the SFT during ISW propagation based on CFD. In addition, the thesis provided insight into parameters that affects the hydrodynamic forcing on the SFT by conducting a sensitivity analysis. The influential factors selected in this research include the ISW amplitude, SFT cross-sectional shape, relative distance of the SFT to the pycnocline, and fluid density ratio.

The hydrodynamic force acting on the SFT shows a proportional relation to the ISW amplitude and the fluid density difference. The influence of the relative distance from the SFT to the pycnocline is crucial due to the buoyancy change induced by the ISW evolution. The vertical force and BWR of the SFT can be remarkably altered by the relative positions between the SFT and ISW. The fluid mixing between the top and bottom layers and energy dissipation can be exacerbated by large ISW amplitude and fluid density ratio. By comparing the cross-section geometry, the parametric shape can effectively reduce flow separation and vortex shedding and in this regard, the parametric shape has a better hydrodynamic performance than the simpler shapes (e.g., circular and elliptical shapes). Rank-ordered packets of internal solitons in realistic oceanic conditions would be a realistic hazard case study if field observations by means such as synthetic-aperture radar (SAR) can be carried out.

6.2.3. EXTREME HYDRAULIC EVENTS IMPACTS

When analyzing the dynamic performance of the SFT under extreme hydraulic events, it is essential to determine the appropriate environmental conditions based on the SFT application site. The thesis proposed a multi-scale model method with the framework of Delft3D-FLOW and the CFD solver ANSYS Fluent to determine the hydrodynamic forcing on an SFT under extreme hydraulic events. A worst-case tsunami and a hindcast typhoon in the Qiongzhou Strait were selected as case studies of catastrophic natural disasters. It was found that extreme hydraulic event hazards are partially mitigated due to the sheltering effect of Hainan Island. The selected typhoon scenario is more devastating than the tsunami case for an SFT in terms of hydrodynamic forcing. The maximum current speed induced by tsunamis in the Qiongzhou strait is around 0.9 m/s, whereas it can be around 1.65 m/s for the typhoon case. By comparing the internal forcing on the SFT induced by tsunami and typhoon, it was discovered that in the typhoon scenario, the wave and current provide an approximately equal contribution to the in-line force on the SFT, while the waves play a dominant role in lift force. For the tsunami scenario, inertia plays an important role in the in-line force.

In addition, the thesis compared the hydrodynamic forces acting on the SFT among parametric shape, circular shape, and elliptical shape. The parametric shape has the most streamlined profile, experiencing the minimum in-line force and the smallest wake region in the typhoon scenario. Furthermore, serious vortex shedding is limited to a shorter time period and lower amplitude in the tsunamic scenario compared with other simpler shapes. It is therefore recommended to adopt the parametric shape for the SFT cross-section engineering design.

6.2.4. FLOW-INDUCED VIBRATION AND STRUCTURAL DYNAMIC RESPONSE

One objective of this thesis is to comprehend the flow-induced vibration (FIV) conditions of the SFT under different hydrodynamic loads due to the possibilities of fatigue damage and structural failure. In order to assess the structural dynamics in a more realistic way, a prototype coupled tube-joint-mooring SFT system with a super long span and large aspect ratio model was simulated. A pragmatic approach for FIV prediction of the super long structure was presented considering the spatial randomness distribution of the hydrodynamic loads along the tunnel span by using multi-scale hydrodynamic models (i.e., a large-scale oceanographic model and a small-scale CFD model). It has been elucidated that the SFT tube is unlikely to experience severe resonance under steady currents conditions due to the large cross-sectional dimension and low current speeds.

However, the vibration of the SFT tube is dominated by wave conditions, where a single dominant mode excitation of the tube with a large wave height and period condition should be avoided.

As for the assessment of the SFT dynamic response, for the internal wave conditions, the displacement and acceleration of the SFT under the ISW are far smaller than values that would affects the structural serviceability requirements of floating bridges. As the ISW is a long wave, its frequency is much lower than the natural frequency of the SFT tube. Therefore, resonance of the tunnel tube under ISW conditions becomes unlikely. Due to BWR change during the ISW evolution, a large shear force and bending moment on the SFT may occur. This affects the tension force in the mooring lines, and can threaten the safety and reliability of the SFT system. For extreme hydraulic event conditions, large bending moment and torque may occur at shore connections, where structure fatigue and buckling should merit attention.

In order to mitigate structural dynamic response, a sensitivity analysis of structural parameters is performed to modify the fundamental frequency outside the hydrodynamic frequency. It has been found that the global axial stiffness of the SFT tube is mainly affected by BWR, tunnel tube and element length, and joint and shore connection properties, while the global torsional stiffness is also influenced by mooring parameters. The super-long structure is subject to multi-mode response, and the one end free scenario should be carefully scrutinized during the transportation and installation process. The influence of tunnel element length on the natural frequencies is small compared with other variables. A dynamic process for the SFT configuration optimization is proposed by smartly tuning the fundamental frequencies.

6.3. LIMITATIONS

Since the main objectives of this research are to understand and predict how the SFT behaves under various hydrodynamic loads using numerical simulations and how to optimize the structural configuration for a given environmental condition, some assumptions and limitations exist.

- The main challenge of this innovative structure is the lack of experimental and measured data, especially three-dimensional experimental tests for global dynamic performance analysis of the SFT. The numerical results of a small-scale tube were validated using existing sectional experiments. However, the validation of the numerical results for a prototype super long SFT is rather difficult.

- The applied hydrodynamic loads are assumed transverse to the tunnel tube span as the worst scenario, and hence, two-dimensional CFD models with high fidelity and efficiency were established for the hydrodynamic load computation. However, multi-directional hydrodynamic load impacts in complex ocean environmental conditions such as oblique waves and currents - mainly by means of three-dimensional numerical models and high computational resources - are not taken into consideration in this thesis. Furthermore, in the storm surge impact modelling (Chapter 4), the wave height is determined using only the corresponding x-component of the orbital velocities for the further two-dimensional CFD analysis, and thus, the vertical force induced by waves due to both the pressure fluctuation, and the vertical component of the orbital velocity, is underestimated.

- The hydrodynamics of the SFT is a multi-physics issue with a strong interaction between the flow field and tunnel tube. The hydrodynamic loads alter the pressure distribution along the tunnel, causing an instantaneous movement and deformation of the tube. In addition, the SFT tube motion, in turn, disturbs the surrounding flow field. Fully-coupled two-way fluid-structure interaction (FSI) principally provides accurate results in both structural forcing and fluid field characteristics. However, two-way FSI simulation incurs high computational demand, requiring a constant data transmission between two solvers, making it impractical for a prototype SFT simulation due to the great tunnel length (multiple kilometres) involved. In the context of practical application, it is rational to assume the flow is not heavily affected by small structural deformations of an SFT at this stage, and only one-way FSI was applied as a feasible and efficient way to address the dynamic behaviour of the SFT. However, the quantitative effects of structural deformation and movement on the surrounding flow field are not assessed by the current research.

- As a case study in this research, a potential SFT construction site - Qiongzhou Strait in China was selected, and the dynamic behaviour of a moored-type SFT was modelled with consideration of the water depth and severe environmental conditions in the Qiongzhou Strait. The dynamic behaviour of other types of SFT (such as pontoon-type and pile-type) and in other application sites are not taken into consideration.

6.4. RECOMMENDATIONS

This thesis presents the dynamic response of a submerged floating tunnel under various hydrodynamic loads and the structural optimization methods for the SFT cross-section and global configuration with the aim of improving hydrodynamic performance. The hydrodynamic loads that have been studied include steady and unsteady currents, waves, internal solitary waves, and extreme hydraulic events (i.e., typhoon and tsunami). The structural deflections and internal forcing of a prototype tube-joint-mooring system of an SFT have been evaluated under different hydrodynamic loads. Flow-induced vibration issues under wave and current conditions have been discussed. Based on the findings of this thesis, some recommendations for model validation can be proposed for follow-on research and can be mainly distinguished into the following two main categories.

6.4.1. PHYSICAL MODEL TEST

One of the limitations of this thesis is the lack of experimental and measured data to validate the global hydrodynamic performance of the tube-joint-mooring system, especially three-dimensional experimental tests. Experimental tests are essential and irreplaceable to provide a reference for numerical model validation and engineering design. Despite some two-dimensional SFT segment tests that have been implemented in recent years, the characteristics of local and global motions and deflections and complex interactions of the tube-joint-mooring system cannot be reflected by those two-dimensional models, and three-dimensional global model tests for an SFT are still lacking.

Recently, a global hydrodynamic physical model test of the SFT at a model scale of 1:50 was conducted at the Tianjin Research Institute for Water Transport Engineering in China (Zhang et al. 2021). Based on the findings of this thesis, some recommendations for the physical model test are provided. In order to systematically investigate the global dynamic response of an SFT with a long span, a physical model test for a coupled tube-joint-mooring SFT system in a wave-current basin should be carried out. Advanced motion response and deformation measuring techniques underwater for the tunnel tube should be explored. For the hydrodynamic evaluation of an SFT, the following issues are recommended to be identified as the key areas for further investigations by three-dimensional physical model tests.

- The effects of complex and extreme hydrodynamics, inclined current conditions, oblique wave conditions (also wave propagation in the longitudinal direction), non-uniformity of the hydrodynamic loads along the span.

- Tunnel motion response (e.g., displacement, velocity, and acceleration in six DOFs) under wave, current, and combined wave-current conditions.

- Internal forcing on the SFT tube and slack-taut behavior of the mooring system under wave, current, and combined wave-current conditions.

- The synergistic behavior of joints in six DOFs and shore connection constraints under wave, current, and combined wave-current conditions.

- The flow-induced vibration of the tunnel tube and mooring lines under wave, current, and combined wave-current conditions.

- Hydroelastic properties of the tunnel tube under wave, current, and combined wave-current conditions.

- The scale effect on the hydrodynamic performance of the SFT.

6.4.2. NUMERICAL MODEL SIMULATION

In this thesis, the approach to predict dynamic response of the SFT is intrinsically a one-way fluid-structure interaction (FSI) technique where the effects of structural motion and deformation on the surrounding flow fields are neglected based on the assumptions of small structural deflection of the SFT. However, a three-dimensional fully-coupled two-way FSI method can principally provide more accurate results for both structural forcing and fluid field characteristics. For the fully-coupled two-way FSI method, the fluid force in the fluid domain is transferred to the nodes of the SFT tube at each time step, and accordingly, the motion responses of the SFT tube computed by the structural solver is mapped to the moving boundary or immersed boundary (i.e., immersed boundary method) of the fluid domain. The computational mesh of the fluid domain is updated based on the structural motion using the dynamic mesh technique. Therefore, the nonlinear hydroelastic effects of the SFT associated with fluid-structure interaction can be precisely evaluated. Furthermore, multi-directional hydrodynamic loads impacts on the SFT can be simulated, compared, and discussed. The mesh-based open-source CFD software OpenFOAM or commercial software such as ANSYS and ABAQUS can be adopted for the fully-coupled two-way FSI modelling. In addition, a mesh-free technique, the smoothed particle hydrodynamics (SPH) method using the code Dual-SPHysics, can also be applied for complex structural dynamics and fluid-structure interaction simulations. However, due to its utmost intensive computation, powerful parallel computing with high-performance computing (HPC) clusters should be conducted. In a more practical way, some modelling simplification and optimization approaches should be explored and validated especially for the modelling of a prototype SFT with a super long span.

In terms of structural optimization, more influential factors (e.g., structure behavior, technical difficulties, service level, and construction cost) can be included and more optimization strategies (e.g., deep learning) can be applied. For the further stability and reliability evaluations of an SFT, multi-discipline research method can be used by linking this research to structure and risk analysis and by further cooperation. The following issues are recommended to be identified as the key areas for further investigation by the numerical model simulations.

- The effects of structural deformation and movement on the surrounding flow field.
- The effects of complex and extreme hydrodynamics, multi-directional current and wave conditions (also wave propagation in the longitudinal direction), non-uniformity of the hydrodynamic loads along the span.
- The nonlinear effects arising in connection with wave-structure interactions such as wave breaking, slamming, and drift forces (second-order wave impacts).
- The flow-induced vibration of the tunnel tube and mooring lines under wave, current, and combined wave-current conditions.
- The effects of hydrodynamic loads combined with service loads (e.g., rail or road traffic) and the combination of flow-induced vibration and traffic-induced vibration issues.
- The effects of accidental or impact loads which result from low probability events (e.g., vehicle or ship impact, ship waves, explosion, earthquake, flooding, drift ice).
- The fluid-structure-seabed interaction analysis for the assessment of the coupling effects of tube-mooring system-foundation dynamics.
- The development of simplification and optimization approaches of modelling to balance the accuracy and efficiency.
- An integrated structural optimization method considering the combined effects of the hydrodynamic performance, structure behavior, technical difficulties, service level, and construction cost.

- Linking this work to the overall structure and risk research for the reliability assessment of the SFT concepts.
- The scale effect on the hydrodynamic performance of the SFT.

REFERENCES

Zhang, H., Yang, Z., Li, J., Yuan, C., Xie, M., Yang, H. & Yin, H. (2021), 'A global review for the hydrodynamic response investigation method of submerged floating tunnels', *Ocean Engineering* **225**, 108825.

NOMENCLATURE

α_k	Inverse effective Prandtl numbers for k (-)
α_ϵ	Inverse effective Prandtl numbers for ϵ (-)
β	Bezier curve parameter (m)
β_1	Rayleigh damping coefficient (s^{-1})
β_2	Rayleigh damping coefficient (s)
δ	Structural motion amplitude (m)
ϵ	Turbulent dissipation rate ($\mathrm{m}^2 \cdot \mathrm{s}^{-3}$)
γ	Intermittency (-)
κ	Fluid thickness coefficient (-)
λ	Characteristic internal wave length (m)
$\widetilde{\mathrm{R}_{\mathrm{e}\theta \mathrm{t}}}$	Transition momentum thickness Reynolds number (-)
$\mathrm{R_e}$	Reynolds number (-)
μ	Fluid viscosity ($\mathrm{kg{\cdot}m}^{-1} \cdot \mathrm{s}^{-1}$); fluid thickness coefficient (-)
μ_t	Eddy viscosity ($\mathrm{kg{\cdot}m}^{-1} \cdot \mathrm{s}^{-1}$)
μ_{eff}	Effective viscosity ($\mathrm{kg{\cdot}m}^{-1} \cdot \mathrm{s}^{-1}$)
ω	Wave frequency (s^{-1}, $\mathrm{rad} \cdot \mathrm{s}^{-1}$)
ω_e	Effective wave frequency (s^{-1}, $\mathrm{rad} \cdot \mathrm{s}^{-1}$)
ω_i	i^{th} mode natural frequencies (s^{-1}, $\mathrm{rad} \cdot \mathrm{s}^{-1}$)
ω_m	Integral frequency scale (s^{-1}, $\mathrm{rad} \cdot \mathrm{s}^{-1}$)
Φ	Latitude (deg.); velocity potential ($\mathrm{m}^2 \cdot \mathrm{s}^{-1}$)
ρ	Density ($\mathrm{kg{\cdot}m}^{-3}$)
ρ_1	Density of the upper-layer ($\mathrm{kg{\cdot}m}^{-3}$)
ρ_2	Density of the lower-layer ($\mathrm{kg{\cdot}m}^{-3}$)
ρ_c	Concrete density ($\mathrm{kg{\cdot}m}^{-3}$)

ρ_s	Steel shell density (kg·m^{-3})
ρ_w	Water density (kg·m^{-3})
σ	Volume fraction (-)
τ_ω	Local wall shear stress (N·m^{-2})
θ	Rotational angle of Gina gasket (rad)
ξ	Modal damping ratio (-)
A	Cross-sectional area (m^2)
a	Wave amplitude (m)
A_c	Cross-sectional area of concrete (m^2)
A_{s1}	Cross-sectional area of outer shell (m^2)
A_{s2}	Cross-sectional area of inner shell (m^2)
b	Bezier curve parameter (m)
b_{low}	b at lower half of the tunnel profile (m)
b_{up}	b at upper half of the tunnel profile (m)
c	Chord length (m)
C_1	Linear damping resistance (s^{-1})
C_2	Quadratic damping resistance (m^{-1})
C_d	Drag coefficient (-)
C_l	Lift coefficient (-)
C_m	Inertia coefficients (-)
C_p	Pressure coefficient (-)
C_x	Dimensionless horizontal force (-)
C_y	Dimensionless vertical force (-)
$C_{d,m}$	Time-averaged drag coefficient (-)
$C_{f,m}$	Time-averaged skin-friction coefficient (-)
$C_{l,max}$	Max. lift coefficient (-)
$C_{l,rms}$	RMS lift coefficient variability (-)
c_{mKdV}	Phase velocity of internal wave (m·s^{-1})

D	Cylinder of diameter (m)
d	Relative distance of the SFT to the pycnocline (m)
d_p	Thickness of the pycnocline layer (m)
E	Equivalent elastic modulus (GN·m^{-2})
E_c	Elastic modulus of concrete (GN·m^{-2})
$E_{\gamma 1}$	Transition source (m$^2 \cdot$ s^{-3})
$E_{\gamma 2}$	Relaminarization source (m$^2 \cdot$ s^{-3})
E_{s1}	Elastic modulus of outer shell (GN·m^{-2})
E_{s2}	Elastic modulus of inner shell (GN·m^{-2})
F	Force (N)
f_i	Eigen-frequency (s^{-1}, rad $\cdot$ s^{-1})
F_x	Horizontal force (N)
F_y	Vertical force (N)
$F_{l,d}$	Lift or drag force per meter (N·m^{-1})
g	Gravitational acceleration (m·s^{-2})
G_b	Generation of k due to buoyancy (kg $\cdot$ m$^{-1} \cdot$ s^{-3})
G_k	Generation of k due to the mean velocity gradients (kg $\cdot$ m$^{-1} \cdot$ s^{-3})
H	Cross-sectional vertical clearance (m);total water depth (m)
h	Lateral consecutive vortex spacing (m)
h_1	Thickness of the upper-layer (m)
h_2	Thickness of the lower-layer(m)
h_c	Critical level (m)
I	Equivalent moments of inertia (kg·m^2)
i	Slope (-)
I_c	Cross-sectional moments of inertia of concrete (kg·m^2)
I_{s1}	Cross-sectional moments of inertia of outer shell (kg·m^2)
I_{s2}	Cross-sectional moments of inertia of inner shell (kg·m^2)
k	Turbulent kinetic energy per unit mass (m$^2 \cdot$ s^{-2}); wave number (m^{-1})

k_0	Initial axial stiffness (GN·m^{-2})
k_u	Axial stiffness of Gina gasket (GN·m^{-1})
k_θ	Bending stiffness of Gina gasket (GN·m)
L	Wave length (m);tube length (m)
l	Longitudinal consecutive vortex spacing (m)
M	Moment (N·m)
n	Manning coefficient (s·m$^{-1/3}$)
p	Pressure (N·m^{-2})
$P_{\gamma 1}$	Transition source ($m^2 \cdot s^{-3}$)
$P_{\gamma 2}$	Destruction source ($m^2 \cdot s^{-3}$)
p_∞	Reference pressure (N·m^{-2})
$P_{\theta t}$	Production source term ($m^2 \cdot s^{-3}$)
p_{ref}	Reference pressure (N·m^{-2})
R	Curb or sidewalk (m)
r	Leading-edge radius (m)
R_m	Radius of maximum wind (m)
S_k	User-defined source terms ($kg \cdot m^{-1} \cdot s^{-3}$)
S_t	Strouhal number (-)
S_ϵ	User-defined source terms ($kg \cdot m^{-1} \cdot s^{-4}$)
S_{max}	Grid size at outer boundaries (m)
S_{min}	Gird size of the tunnel profile (m)
T	Wave period (s)
t	Time (s)
T_u	Turbulence intensity (-)
T_{uinlet}	Inlet turbulence intensity (-)
U	Upstream flow velocity (m·s^{-1})
u	Horizontal velocities of water particles (m·s^{-1})
V_m	Maximum wind speed (m·s^{-1})

V_R	Reduced velocity (-)
W	Cross-sectional lateral clearance (m)
x_t	Half of the cross-sectional width (m)
y	Vertical coordinate of the grid (m)
Y^+	Dimensionless wall distance (-)
y_c	Position of the mid-pycnocline layer (m)
Y_m	Contribution of the fluctuating dilatation in compressible turbulence to the overall dissipation rate ($\mathrm{kg \cdot m^{-1} \cdot s^{-3}}$)
y_t	Half of the cross-sectional height (m)
y_{low}	y at lower half of the tunnel profile (m)
y_{up}	y at upper half of the tunnel profile (m)

ACKNOWLEDGEMENTS

As a part of the submerged floating tunnel project, this research was funded by **China Communications Construction Company Ltd. (CCCC)**. Despite twists and difficulties of the project during the period, I am still very pleased to see it proceed as scheduled. I would also like to thank **CCCC-FHDI** for the continuous encouragement, support, and concern.

Three years ago, I never imagined to be a PhD candidate to study abroad in my engineer career, and the hesitation, confusion, and expectation to start a new journey seem to be still in front of my eyes. However, time flies, my PhD life is coming to an end. Looking back on these extraordinary years, bit by bit, I am deeply moved.

Thanks to my daily supervisor **Jeremy Bricker**, for answering my questions patiently and meticulously at every progress meeting and helping me out by contacting experts and scholars who can collaborate with as always, from meet physically to online, from Delft to the United States. The efficient project progress is inseparable from his timely and high-quality feedback. I cherish the time communicating with him and I'm inspired by his always positive attitude towards life. With the ups and downs of my mood especially during the pandemic, Jeremy will always be like a peaceful lake, diminishing and smoothing out my anxiety and confusion, making me feel warm in a foreign country. I would also like to thank my promoter **Wim Uijttewaal** for caring about the progress of my research out of his busy schedule. My understanding of the research topic can be more in-depth by his enlightening questions. His rigorous academic and meticulous spirit are my role models. Thanks to **Carlos Simao Ferreira** for being my committee member and giving me valuable suggestions on the topic. These bits and pieces are all fond memories of the past years.

Thanks to my friends who have accompanied me over the difficult but wonderful years, **Ma Xu**, **Miguel**, **Shaoqing**, for many times of cycling, jogging, watching movies, visiting museums, travelling, fitness, dinner parties, and of course, heart-to-heart talks. I overcame so many times of isolation, hesitation, and lack of motivation with your encouragement and support; it's heartily unforgettable to play badminton and work out with **Kuai Yu** and **Su**; to my office-mates **Miguel**, **Gina**, and **Danny** for the rare fate and the happy time together; to **Xuexue** for giving me advice and help on the project and the nice memories during the conference in Greece; to the SFT team members in TU Delft, **Lingfeng, Gina, Marcel, Yan Ni, Roelof, Oswaldo, Dirk Jan, Bas**, it is a pleasure to work on the same project and enlighten ideas with you; and to other fellow PhDs and colleagues in my section for coffee breaks and sectional events, **Liu Lian, Ke Qian, Robert, Ece, Chris, Ermano, Mark, Kristina, Judith, Dianna, Eefke**; I am happy to join PhD council of CEG faculty and to represent the PhD fellows of my department. Thanks to **Silke** for getting me involved in and thank everyone who I worked with: **Marco, Ali, Mariska, David, Joelle Martijn, Bahareh, Kevin, Angeliki, Emanuele, Shozab, Til, Sebastian**. Thank my parents and families for their unconditional love and support over

the years. Thanks to all the people I encountered and interacted with, and the moments I seized and memorized.

Life is like a winding river, sometimes rushing turbulently, sometimes trickling slowly. The days in the Netherlands are as calm as water and as quiet as poetry. It is rare to have a period intently focusing on scientific research and thinking and exploration without distractions. It is also valuable to study abroad, explore different cultures, and experience the variety of the world. Though there is no lack of regrets - nearly two-thirds of my PhD life is spent at home with online classes and meetings due to the pandemic, which reduces the opportunities for interactions and communications with peer fellows and colleagues. I can honestly admit to suffering certain mental turbulence and anxiety, but it is precise because of this unique experience that I feel that people share weal and woe, and I learned to pay more attention to my inner health and emotional resilience, to think the meaning of life and connections with the outside societies.

At the end of this unforgettable period, I would say that PhD life is a journey to create possibilities for knowledge exploration, which is perhaps the closest way to my understanding of the value of life - to discover, think, and create. This creation is full of life enthusiasm, and this curiosity drives us to move forward and never stop.

Pengxu Zou
August, 2021, in Delft

CURRICULUM VITÆ

Pengxu ZOU

21-08-1992	Born in Shenyang, Liaoning, China.

EDUCATION

2010–2014	BSc in Port and Coastal Engineering (CumLaude) Tianjin University, Tianjin, China
2014–2017	MSc in Hydraulic Engineering Tianjin University, Tianjin, China
2019–2022	PhD in Hydraulic Engineering Delft University of Technology, Delft, the Netherlands
Thesis:	Dynamic response of a submerged floating tunnel subject to hydraulic loading
Promotor:	Prof. Wim S.J. Uijttewaal
Copromotor:	Dr. Jeremy D. Bricker

LIST OF PUBLICATIONS

PEER-REVIEWED JOURNAL PAPERS

5. **P. X. Zou**, J. D. Bricker, L. Z. Chen, W. S. J. Uijttewaal, and C. S. Ferreira, *Response of a Submerged Floating Tunnel Subject to Flow-induced Vibration*, Engineering Structures **253**, (2022).

4. **P. X. Zou**, J. D. Bricker, and W. S. J. Uijttewaal, *The impacts of internal solitary waves on a submerged floating tunnel*, Ocean Engineering **238**, (2021).

3. **P. X. Zou**, J. D. Bricker and W. S. J. Uijttewaal*Submerged floating tunnel cross-section analysis using a transition turbulence model*, Journal of Hydraulic Research **,** (2021).

2. **P. X. Zou**, J. D. Bricker, and W. S. J. Uijttewaal, *Impacts of extreme events on hydrodynamic characteristics of a submerged floating tunnel*, Ocean Engineering **218**, (2020).

1. **P. X. Zou**, J. D. Bricker, and W. S. J. Uijttewaal, *Optimization of submerged floating tunnel cross section based on parametric Bzier curves and hybrid backpropagation - genetic algorithm*, Marine Structures **74**, (2020).

CONFERENCE PAPERS

2. **P. X. Zou**, L. Z. Chen, *The Coupled Tube-Mooring System SFT Hydrodynamic Characteristics Under Wave Excitations*, Proceedings of the 14th International Conference on Vibration Problems, (2021).

1. **P. X. Zou**, J. D. Bricker, and W. S. J. Uijttewaal, *A parametric method for submerged floating tunnel cross-section design*, The 30th International Ocean and Polar Engineering Conference, (2020).